Dissertation

Influence of Microstructure on Material Behaviour of WC-Co Hard Metals under Static and Cyclic Loading Conditions

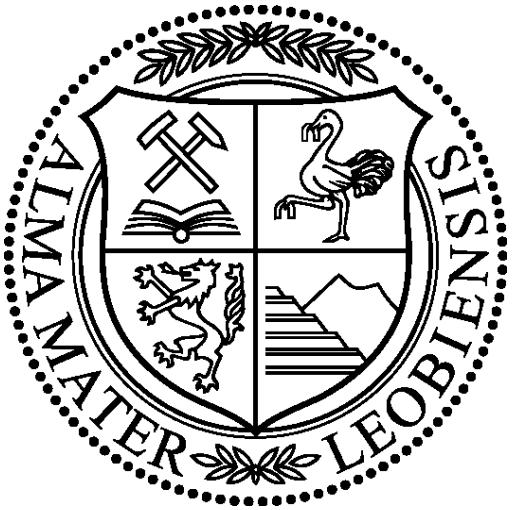

DI Thomas Klünsner

Leoben, May 2011

A thesis in fulfilment of the requirements for the degree

Doctor rerum montanarum (Dr.mont.)

at the University of Leoben

Eidesstattliche Erklärung

Ich erkläre an Eides statt, dass ich diese Arbeit selbstständig verfasst, andere als die angegebenen Quellen und Hilfsmittel nicht benutzt und mich auch sonst keiner unerlaubten Hilfsmittel bedient habe.

Affidavit

I declare in lieu of oath, that I wrote this thesis and performed the associated research myself, using only literature cited in this volume.

Leoben, May 2011

Thomas Klünsner

Acknowledgements

My thanks for giving me the opportunity to perform my work go to both my supervisors **Prof. Dr. Reinhard Pippan** and **Prof. Dr. Reinhold Ebner** who were never tired of discussing my latest findings. Without their helpful guidance and their expert input my work would not have been possible.

Especially I want to thank **Dr. Stefan Marsoner**, **DI Stefan Wurster, Prof. Dr. Peter Supancic**, **Dr. Werner Ecker, Dr. Sven Eck, Dr. Anton Ishmurzin, Dr. Hans-Peter Gänser** and **Naeem Huque** for the time they spent helping me to complete my work.

Also, I want to acknowledge **Johannes Glätzle, Dr. Arndt Püschel** and **Dr. Manuel Beschliesser** for providing samples and expertise in the field of hard metals.

Furthermore, many thanks go to all my colleagues at the Materials Center Leoben Forschung GmbH (MCL) and the Erich Schmid Institute of Materials Science of the Austrian Academy of Sciences who provided me with a pleasant working environment.

Financial support by the Austrian Federal Government (in particular from the Bundesministerium für Verkehr, Innovation und Technologie and the Bundesministerium für Wirtschaft und Arbeit) and the Styrian Provincial Government, represented by Österreichische Forschungsförderungsgesellschaft mbH and by Steirische Wirtschaftsförderungsgesellschaft mbH, within the research activities of the K2 Competence Centre on "Integrated Research in Materials, Processing and Product Engineering", operated by the Materials Center Leoben Forschung GmbH in the framework of the Austrian COMET Competence Centre Programme, is gratefully acknowledged.

Table of contents

Table of contents 3
1 Introduction 5
2 Einleitung 7
3 Theoretical background 9
3.1 Linear elastic fracture mechanics 9
3.2 Weibull statistics 10
3.2.1 Effectively tested sample volume 12
3.2.2 Specimen size effect 12
3.3 Matricity parameter 13
4 Investigated materials 15
4.1 Investigated hard metal grades 15
4.1.1 Typical microstructures of WC-Co hard metals 17
5 Material testing procedures for hard metals 20
5.1 Uniaxial loading conditions 21
5.1.1 Specimen design and manufacture 21
5.1.2 Testing setup 22
5.1.3 Strain measurement accuracy 23
5.1.4 Strain correction 24
5.1.5 Buckling resistance and stress distribution 26
5.1.6 Test reproducibility 33
5.2 Bending loading conditions 33
5.2.1 Specimen design and manufacture 34
5.2.2 Testing setup 36
6 Material properties under monotonous loading conditions 40
6.1 Influence of microstructure on flow behaviour 40

6.1.1 Uniaxial compression loading conditions 41
6.1.2 Influence of matricity and mean free path on flow behaviour 46
6.2 Influence of microstructure and specimen size on fracture behaviour 52
6.2.1 Uniaxial loading conditions 52
6.2.2 Influence of effectively tested volume on tensile fracture strength 54
6.2.2.1 Data evaluation 55
6.2.2.2 Results of strength characterisation 57
6.2.2.3 Defect sizes 61
6.2.2.4 Defect densities 68
7 Material properties under cyclic loading conditions 75
7.1 Flow behaviour under cyclic loading conditions 76
7.1.1 Cyclic stress-strain curves under uniaxial loading conditions 76
7.1.2 Ratchetting behaviour under uniaxial loading conditions 80
7.2 Fracture behaviour under cyclic loading conditions 84
7.2.1 Fracture behaviour under uniaxial cyclic loading conditions 84
7.2.1.1 S-N behaviour under various stress ratios 85
7.2.1.2 Dependence of fatigue crack growth threshold on stress ratio 86
7.2.1.3 Influence of overloads on S-N behaviour 88
7.2.1.4 Influence of material batch on S-N behaviour 90
7.2.2 Fracture behaviour under cyclic bending loading conditions 91
7.2.2.1 Influence of surface finish on S-N behaviour 91
7.2.2.2 Influence of residual stress state on S-N behaviour 95
8 Summary and Outlook 100
9 References 102
10 Appendix 111

1 Introduction

WC-Co hard metals are so far mainly utilised for wear applications and metal machining. In recent years the property spectrum of WC-Co has been widened significantly, so today new hard metal grades are available with improved hardness, bending strength and/or fracture toughness. The main achievements are based on WC grain refinement, leading to fine and ultrafine grained hard metal grades.

To facilitate the reliable design of fatigue resistant tools or structural components via e.g. finite element methods (FEM), a sound knowledge of the materials' behaviour under static and cyclic loading conditions is required. Unfortunately, material data such as yield strength and fatigue strength for WC-Co hard metals is scarce in literature today, especially for grades of ultrafine WC grain size.

There is increasing interest in the application of hard metals in components and tools, varying widely in dimensions, e.g. cutting matrices at the decimetre sizes, fine blanking tools at centimetre sizes or printed circuit board drills with diameters even below 200 µm. Since there exists a significant influence of loaded volume on tensile stress sustained in service, part design also requires some basic understanding of their relation. To date, the dependence of tensile strength data on specimen size has not been thoroughly investigated for ultrafine grained WC-Co hard metals in a wide range of specimen sizes.

In the present work, detailed information about a material testing procedure for the reliable determination of the stress-strain response of WC-Co hard metals under uniaxial loading conditions, in tension and compression, is presented. Material data such as Young's modulus and yield strength were determined under uniaxial loading conditions, along with the influence of microstructural parameters such as WC grain size, binder content and binder matricity on flow behaviour.

In addition, the dependence of tensile fracture behaviour on specimen size was examined for a vast dimensional spectrum, in which loaded volumes vary over a wide range depending on specimen size and stress distribution, revealing the intrinsic ultimate strength of ultrafine grained WC-Co hard metals in tension.

Furthermore, the cyclic stress-strain response, including ratchetting behaviour, was studied under uniaxial loading conditions, as well as the cyclic fracture behaviour, which was investigated via S-N curves determined under uniaxial and bending loading conditions. The threshold of the stress intensity factor range at which fatigue crack growth starts from inhomogeneities was determined for different stress ratios. Results of investigations on the effects of surface finish, residual stresses and overloads on the S-N behaviour of WC-Co hard metals are discussed.

2 Einleitung

WC-Co Hartmetalle werden heute hauptsächlich in Verschleißanwendungen und in der Metallzerspanung verwendet. In letzter Zeit wurde das Eigenschaftspektrum von WC-Co wesentlich erweitert und so sind nun neue Hartmetallsorten mit verbesserter Härte, Biegefestigkeit und/ oder Bruchzähigkeit erhältlich. Die größten Verbesserungen der Eigenschaften basieren auf WC Kornfeinung, so dass in modernen Sorten feine und ultrafeine WC Korngrößen vorliegen.

Um die verlässliche Auslegung von ermüdungsresistenten Werkzeugen und strukturellen Komponenten mit z. B. Finite-Elemente-Methoden (FEM) zu ermöglichen, ist eine profunde Kenntnis des Materialverhaltens unter statischer und zyklischer Belastung erforderlich. Leider sind Materialdaten wie Fließgrenzen oder Ermüdungsfestigkeiten kaum in der offenen Literatur verfügbar, speziell für Sorten mit ultrafeinem WC Korn.

Es existiert verstärktes Interesse an der Anwendung von Hartmetallen in Komponenten und Werkzeugen in den unterschiedlichsten Dimensionen: Schneid-Matrizen in Dezimetergrößen, Feinschneidestempel in Zentimetergrößen oder auch Leiterplattenbohrer mit Durchmessern von weniger als 200 µm. Weil die Zugfestigkeit von Komponenten aus Hartmetall entscheidend vom beanspruchten Volumen im Bauteil abhängt, ist ein grundlegendes Verständnis der Abhängigkeit dieser Größen voneinander notwendig. Bis heute wurde die Beziehung zwischen Zugfestigkeit und beanspruchtem Volumen für ultrafeinkörnige WC-Co Hartmetalle nicht eingehend, in breiter Variation beider Größen, untersucht.

In der vorliegenden Arbeit wird eine Materialprüfmethode dargestellt, die die zuverlässige Bestimmung der Spannungs-Dehnungs Antwort von WC-Co Hartmetallen unter uniaxialer Belastung in Zug und Druck ermöglicht. Materialdaten wie E-Modul und Fließgrenze wurden unter uniaxialer Belastung bestimmt. Ebenso wurde der Einfluss von Gefügeparametern wie WC Korngröße, Bindergehalt und Matrizität des Binders auf das Fließverhalten untersucht.

Weiters beleuchtet die Arbeit die Abhängigkeit des Bruchverhaltens unter Zugbelastung für ein weites Spektrum von Volumen unter Zugbelastung, das je nach Probengröße und Spannungsverteilung variiert, und legt die intrinsische Zugfestigkeit von ultrafeinkörnigem WC-Co Hartmetall dar.

Außerdem wurde die zyklische Spannungs-Dehnungs Antwort unter uniaxialer Belastung inklusive dem Ratchettingverhalten untersucht. Das zyklische Bruchverhalten wurde durch unter uniaxialer Belastung sowie Biegebelastung gewonnener Wöhlerkurven charakterisiert. Der Schwellwert des Spannungsintensitätsfaktors, bei dem Ermüdungsrissausbreitung von Gefügeinhomogenitäten startet, wurde für verschiedene Spannungsverhältnisse bestimmt. Ergebnisse von Untersuchungen hinsichtlich der Einflüsse von Oberflächengüte, Eigenspannungen und Überlasten auf das Ermüdungsverhalten von WC-Co Hartmetallen werden diskutiert.

3 Theoretical background

In the current section, a brief introduction to theoretical concepts utilised in the present work is given. Only the most important relations on the respective topics are given. For more detailed information the reader is referred to the cited literature.

As most high strength materials, WC-Co hard metals show defect-controlled tensile fracture behaviour. Defects that occur in hard metal microstructures are, for instance, pores [1], non-metallic inclusions [2], (micro-) cracks [3] or enlarged WC grains and their agglomerates. Note that in brittle materials the results of strength experiments are a direct measure for defect size distributions [4] and can be evaluated via Weibull statistics [5],[6], which facilitate predictions about the fracture behaviour of a batch of samples. For a certain stress, a certain probability of failure is predicted for an individual specimen. Due to the statistical size distribution and spatial distribution of defects, values of stress at fracture also become a function of specimen size or effectively tested sample volume (i.e. the effective volume V_{eff}) which represents the equivalent volume of a sample under uniaxial tensile loading conditions [7].

In this section, a brief introduction to linear elastic fracture mechanics relations that connect stress at fracture and defect size is given, along with a short summary of Weibull statistics. The specimen size effect and the determination of values of V_{eff} for simple and more complex specimen geometries are described along with a microstructural parameter referred to as matricity M. Along with the Co binder content and mean free path in the binder λ_{Co}, M is thought to be capable of correlating the materials' microstructures and their stress-strain behaviour.

3.1 Linear elastic fracture mechanics

To estimate critical defect sizes that lead to failure in WC-Co hard metals, linear elastic fracture mechanics (LEFM) [8] were used as a first approximation. Combining stress at fracture σ_f and defect radius a, as in Eq. 1, gives a value referred to as stress intensity factor K [9].

$$K_{IC} = \sigma_f Y \sqrt{\pi a} \quad (1)$$

K_{IC} is the critical value of stress intensity (i.e. fracture toughness) above which unstable crack propagation occurs, σ_f is the fracture stress and Y is a dimensionless factor accounting for geometrical details of the crack shaped defect and the specimen. Y varies from 0.63 for a penny shaped volume crack [10] and 1.12 for a shallow surface crack [11]. The defect radius that causes unstable crack growth at a given stress σ, referred to as a_c is found by rearranging Eq. 1:

$$a_c = \frac{1}{\pi}\left(\frac{K_{IC}}{Y\sigma}\right) \quad (1a)$$

3.2 Weibull statistics

For brittle, homogeneous materials loaded under uniaxial homogeneous tension, containing a population of defects whose relative density decreases with a negative power of their radius (Weibull material), a probability of failure F can be described as a function of the stress at fracture at room temperature σ_f and the sample volume V via Eq. 2 as postulated by Weibull [5],[6]. It is assumed that stress fields of flaws do not interact and that failure of a single defect causes the whole specimen to fracture (weakest link hypothesis).

$$F(\sigma, V) = 1 - \exp\left[-\frac{V}{V_0}\left(\frac{\sigma}{\sigma_0}\right)^m\right] \quad (2)$$

The characteristic strength σ_0 is the stress at which the probability of failure $F = 1 - e^{-1} \approx 63\%$, for samples of the volume $V = V_0$. The so-called Weibull modulus m describes the scatter of the fracture stress values. A low value of m corresponds to a large scatter range of strength data. Values of m and σ_0 for specimens investigated in the present work were calculated according to the standard ENV 843-5 (i.e. unbiased maximum likelihood parameters) [12].

To learn about the probability of failure depending on the applied load, information on the distribution of defects is necessary (the rest of this section follows the introduction

to Weibull theory from [13]): Knowing the mean number of destructive defects $N_{c,S}(\sigma)$ within a specimen of size and geometry S, one can determine the probability of failure F [14]:

$$F_S(\sigma = -\exp[-N_{c,S}(\sigma \quad (3)$$

Information on $N_{c,S}(\sigma)$ can be gained integrating the local density function of destructive flaws $n_c(\sigma,\vec{r})$, that can depend on the position vector $\vec{r}$, over the specimen volume (i.e. defect density may depend on location in the specimen):

$$N_{c,S}(\sigma = \int n_c(\sigma\ \vec{r})\mathrm{d}V \quad (4)$$

The local density function $n_c(\sigma,\vec{r})$ can be determined by integrating the so-called frequency distribution density of flaw sizes $g(a,\vec{r})$, that can depend on the position vector $\vec{r}$, which depends on two parameters, namely the exponent ($-r$) and a coefficient ($g_0 * a_0^r$):

$$n_c(\sigma\ \vec{r}) = \int_{a_c(\sigma)}^{\infty} g(a,\vec{r})\,\mathrm{d}a = \int_{a_c(\sigma)}^{\infty} g_0 \left(\frac{a}{a_0}\right)^{-r} \mathrm{d}a = \frac{a_c}{r-} g(a_c) \quad (5)$$

The exponent r in Eq. 5 can be determined from the Weibull modulus m:

$$m = (r-1) \quad (6)$$

For an individual specimen from a batch containing X specimens, ranked according to its strength with a ranking parameter i (weakest specimen $i = 1$), the frequency distribution density of flaw sizes $g(a_c,i)$ can be calculated using Eq. 7 [13]:

$$g(a_{c,i}) = \frac{r-}{V a_{c,i}} \ln \frac{2X}{2X - i +} \qquad i = ,2,3,\ldots,X \quad (7)$$

The volume V in Eq. 7 is the effectively tested sample volume V_{eff} described in section 3.2.1. For additional detailed information about Weibull statistics and their application the reader is referred to references [4]-[7],[12]-[18].

3.2.1 Effectively tested sample volume

If the stress distribution in a strength test specimen and the Weibull modulus *m* of the entire specimen batch are known, one can calculate V_{eff} that represents the equivalent volume of a sample under constant tensile stress [7]. For simple flexural specimen geometries such as cylindrical rods [7] or rectangular beams [15] analytic solutions for the calculation of V_{eff} exist. For more complex geometries and stress distributions in specimens and components, V_{eff} can be estimated evaluating Eq. 8 [7] for each integration point of a finite element (FE) simulation model for the respective specimen geometry. The evaluations should be performed at the maximum loads observed in the respective experiments.

$$V_{eff} = \int_V \left(\frac{\sigma_1}{\sigma_{max}} \right)^m dV \qquad (for\ \sigma_1 \geq 0) \tag{8}$$

where V is the volume of the specimen, σ_z the first principal stress (i.e. maximum tensile stress) along the z-axis, σ_{max} the maximum of the first principal stress in the specimen and *m* is the Weibull modulus.

3.2.2 Specimen size effect

In brittle materials, stresses at fracture scale with the effectively tested sample volume [4]. Low strength values are associated with large specimen size and vice versa. Therefore, a quantitative prediction of strength values for a given probability of failure and specimen geometry is possible by strength extrapolation according to the Weibull theory (see Eq. 9) [4]. It is assumed that failure is caused by a single defect type population of non-interacting defects.

$$\sigma_1(R)^m V_1 = \sigma_1(R)^m V_2 \qquad or \qquad \sigma_1(R) = \sigma_1(R) \cdot \left(\frac{V_1}{V_2} \right)^{\frac{1}{m}} \tag{9}$$

where $\sigma_1(R)$ and $\sigma_2(R)$ are the equivalent reference stresses corresponding to the reliabilities *R*. V_1 and V_2 are the respective effective volumes of the specimens.

One of the prerequisites for the application of Weibull theory is that flaws critical for failure do not interact. Please note that this requirement might be violated when tested

specimens become very small. In this case defect density and strength values could be lower than predicted by Weibull theory [13].

3.3 Matricity parameter

Amongst other parameters such as mean WC grains size and Co binder content or phase contiguity [19] that can be used to describe a two-phased microstructure, the so-called matricity parameter M [20] is applied in the present work to quantify microstructural properties of WC-Co alloys (see Eq. 10). It represents the ratio of the skeleton line lengths (as defined in Eq. 10), attained by thinning single phase regions in a binary image to the width of single-pixel lines – leaving the structures' topology, continuity and frequency of branching unchanged [20]. In contrast to matricity, contiguity depends on grain size and is therefore not an exact description of the phase arrangement [20].

$$M_\alpha = \frac{s_\alpha}{s_\alpha + s_\beta} \quad ; \quad M_\alpha + M_\beta = \tag{10}$$

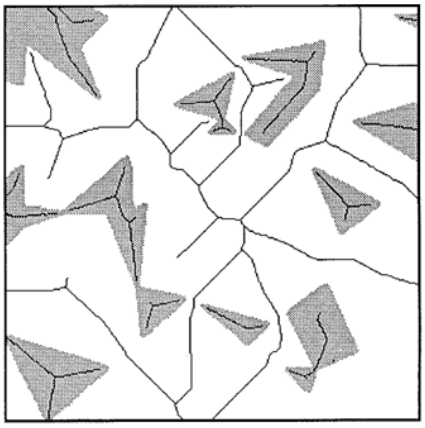

Fig. 1: Skeleton lines of individual phase regions in a two-phased microstructure [20]

The matricity parameter quantitatively describes to what extent a phase forms the matrix or an inclusion in a two-phase composite material. Phase matricity varies between values of 0 and 1 for the respective phase. Binder inclusions, for example, that exhibit a perfectly circular shape give $M_{Co} = 0$ and $M_{WC} = 1$. In the given example the matrix character of the WC phase would be 100%.

A reciprocal dependence of stress-strain behaviour on M_{Co} is found in literature assuming a certain in-situ flow stress for the binder phase and linear elastic behaviour for the hard phase in a FEM simulation of a typical WC-Co hard metal microstructure [21]. The applicability of the concept to other composite materials such as Fe/Ag [22],[23] and ZrO_2/ NiCr 80 20 composite materials [23] has also been demonstrated.

4 Investigated materials

In this chapter the reader is introduced to the investigated hard metal grades, their production, composition and microstructure.

4.1 Investigated hard metal grades

WC-Co hard metals are produced by the powder metallurgical method of liquid phase sintering [24],[25]. In this process, a mixture of WC powder, Co powder, dopant elements and plastifying agent (paraffin wax) is mixed. The resulting blend is then formed to a near net shape e.g. via extrusion forming and sintered at and above temperatures of 1300 °C in a vacuum furnace to prevent oxidation during sintering. To attain ultrafine grained hard metal grades, dopants such as VC are added to prevent WC grain growth [26],[27]. The application of hot isostatic pressing [28] and the application of clean room conditions in production lead to a reduction of porosity levels in the hard metal products [1].

The WC-Co hard metals investigated in this work - commonly characterised by cobalt binder content (wt %), hardness (HV30), average WC grain size and fracture toughness (K_{IC}), as determined by the material manufacturer Ceratizit Austria - are presented in Table 1. The terms “fine”, “submicron” and “ultrafine” as associated with average WC grain sizes in Table 1 will henceforth be used to describe average WC grain dimensions. Fig. 2 gives an overview of the investigated hard metal grades.

Grade	Co [wt %]	HV 30	WC grain size [µm]	K_{IC} [MPa√m]
X1	12	1340	0.8 to 1.3 – fine	12
X2	11.8	1380	0.8 to 1.3 – fine	12
X3	9	1470	0.8 to 1.3 – fine	10.9
X4	6	1610	0.8 to 1.3 – fine	9.9
X5	12	1460	0.5 to 0.8 - submicron	9.9
X6	10	1590	0.5 to 0.8 - submicron	9.4
X7	9	1590	0.5 to 0.8 - submicron	10.4
X8	12	1730	0.2 to 0.5 - ultrafine	7.5
X9	8.2	1930	0.2 to 0.5 - ultrafine	7.5
X10	6.5	2080	0.2 to 0.5 – ultrafine	7.2
X11	9.2	1930	0.2 to 0.5 – ultrafine	8.3

Table 1: Investigated hard metal grades as characterised by Co binder content, hardness, WC grain size and fracture toughness

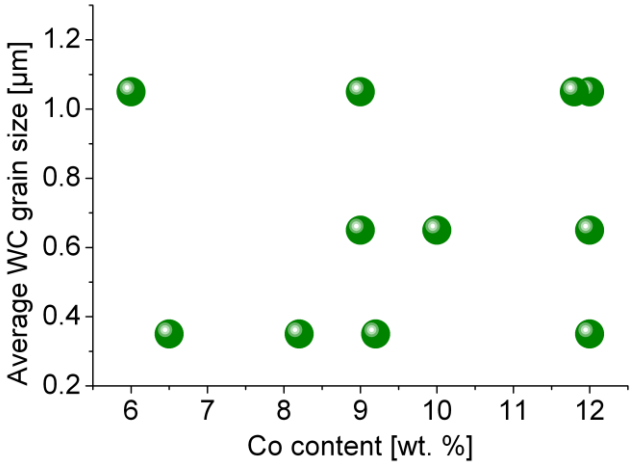

Fig. 2: Overview of hard metal grades investigated in this work in terms of average WC grain size and Co content

4.1.1 Typical microstructures of WC-Co hard metals

To give a general impression on the shape and size range of the microstructural constituents of WC-Co hard metals, scanning electron microscopy (SEM) micrographs of typical microstructures from the extreme ends of the investigated ranges of WC grain size and Co binder content are shown in Fig. 3 to Fig. 6. In the figures, dark grey regions represent the Co phase and light grey represent the WC phase. The surfaces presented in Fig. 3 to Fig. 6 are the result of focused ion beam (FIB) polishing that was applied to avoid the deterioration of small microstructural features such as very fine Co ligaments (see e.g. Fig. 5 or Fig. 6). Note that the slight differences in contrast in the four quadrants of Fig. 3 and Fig. 4 result from joining of four images of higher magnification to one larger image. In the chapter 6.1.2, binarised images of the SEM micrographs presented here will be used to determine the microstructural parameter M_{Co}.

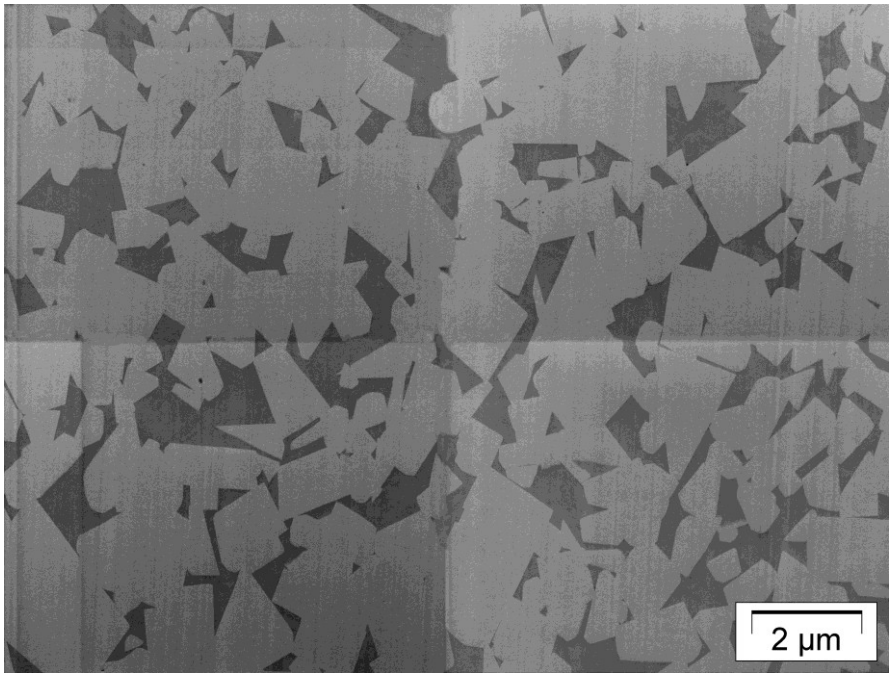

Fig. 3: SEM micrograph of a typical microstructure of hard metal grade X1; 12 wt % Co; fine WC grain size

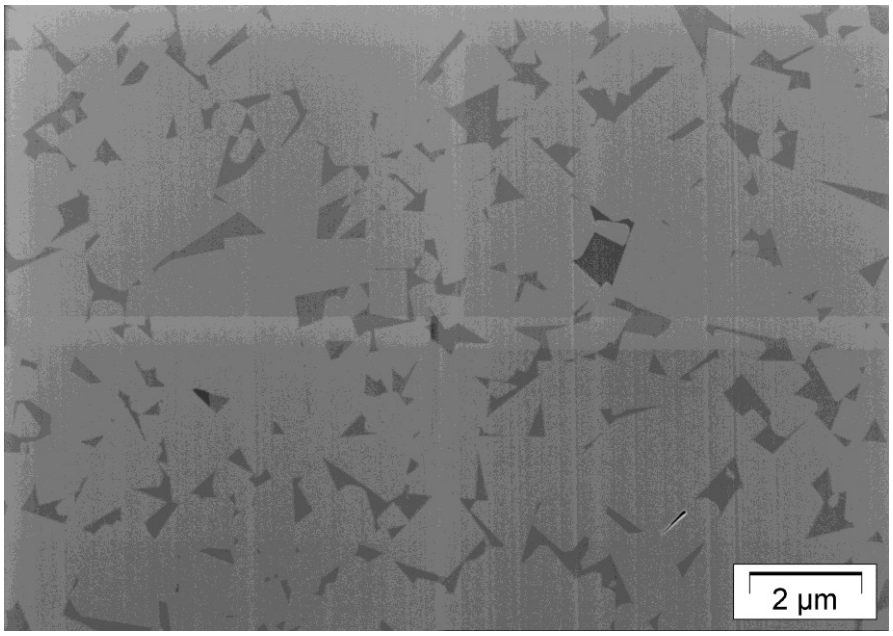

Fig. 4: SEM micrograph of a typical microstructure of hard metal grade X4; 6 wt % Co; fine WC grain size

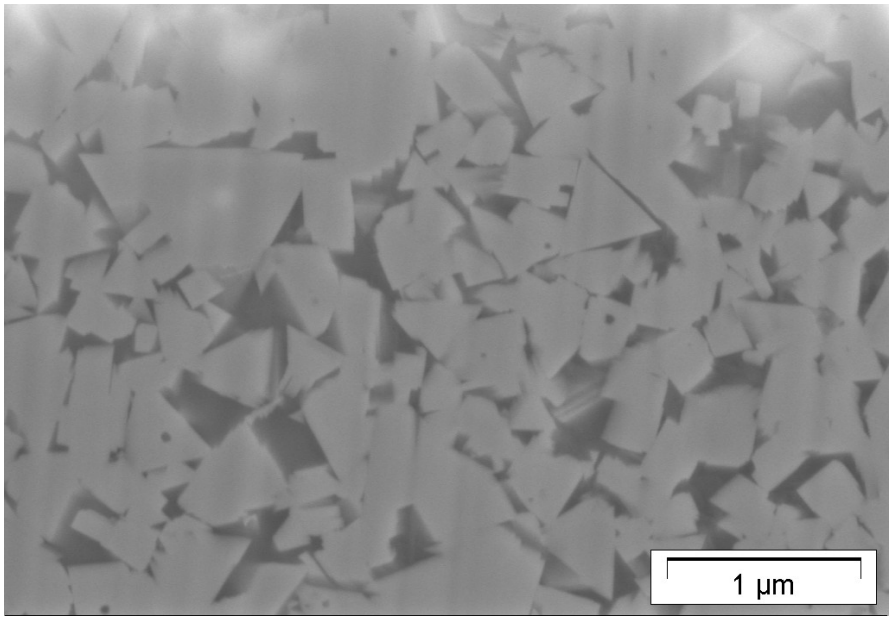

Fig. 5: SEM micrograph of a typical microstructure of hard metal grade X8; 12 wt % Co; ultrafine WC grain size

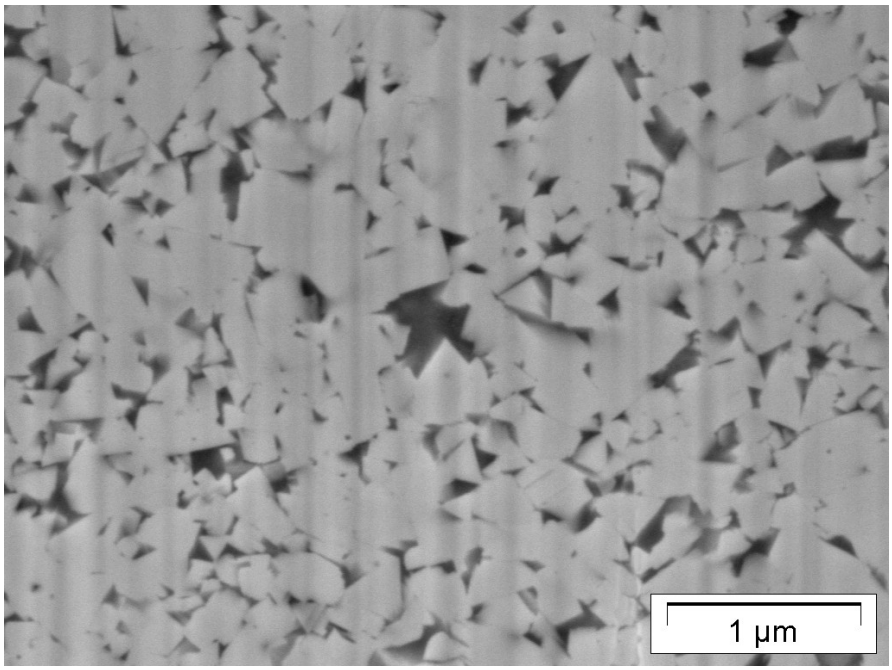

Fig. 6: SEM micrograph of typical microstructure of hard metal grade X10; 6.5 wt % Co; ultrafine WC grain size

5 Material testing procedures for hard metals

For the application of an engineering material in tools or structural components, material data such as yield strength, ultimate strength, Young's modulus or fatigue strength are indispensible prerequisites to proper design. In the present section, a material testing procedure adequate for the reliable determination of material properties of WC-Co hard metals under uniaxial tension and compression loading is presented. The stress distribution in the utilised specimen and the consequences of the possible application of specimens of modified geometry in terms of buckling resistance are investigated via FE simulations. Material testing methods applied to characterise WC-Co hard metals under bending loading conditions are explained at the end of the chapter.

In the past, the mechanical behaviour of WC-Co hard metals has been studied thoroughly in terms of bending strength [29]-[34], hardness and fracture toughness [33]-[44]. Other material data such as yield strength and ultimate tensile or compressive strength are not as well established, mainly due to the high hardness and the low ductility of the material, which makes the determination of reliable material data, necessary for engineering applications of the material, a challenging task.

In literature, one can find a few examples of uniaxial material testing techniques for WC-Co hard metals. Some of these testing procedures can be used to determine material properties under uniaxial tension loading conditions only, using specimens of round [45] or rectangular cross section [46].

Other methods are applicable for compression loading conditions only [47]-[50]. The parallel-sided end faces of the specimens used in these methods are loaded in compression between parallel platens or anvils. A problem with this kind of load application is the occurrence of stress concentrations at the interface between specimen and anvil, that may lead to premature specimen failure. In contrast to methods described in [47] to [49], where short, cylindrical rod type samples are used, the testing technique [50] tackles this problem by relocating the site of maximum stress from the site of load

transfer at the specimen end faces to the specimen's centre, where its diameter is reduced. To avoid high stress gradients, a so-called hydraulic profile design is applied [50], which represents the shape that an ideally frictionless liquid assumes when running out through a circular opening in the bottom of a container. Only one testing technique [51] described in literature allows for the determination of material properties under tensile and compression loading conditions.

An important question in material testing is the efficient transfer of load from the testing machine to the specimen. To facilitate the load transfer, some of the described testing methods rely on brazing of cylindrical specimens into adapters made of steel that contain shoulder features [45] or screw threads [51]. The necessity of these adapters makes these testing procedures quite elaborate and should be avoided in an efficient material testing method.

5.1 Uniaxial loading conditions

5.1.1 Specimen design and manufacture

The requirements of the specimen design for uniaxial tests are (a) a high resistance to buckling in case of compressive loading, (b) the avoidance of stress concentrations in the specimen, (c) a clamping procedure that permits the application of high loads as well as easy sample exchange in the testing facility and (d) a small sample to limit the forces necessary for testing. To meet these requirements a specimen with an hourglass shape with a radius R of 50 mm and a minimum diameter d of 6 mm was chosen to ensure a high resistance to buckling (see Fig. 7). A disadvantage of this specimen geometry is that during testing, average stresses and strains are lower than their maximum values that occur at the specimen's smallest diameter and require correction.

Friction locked clamping of the cylindrical specimen ends in hydraulic jaws facilitates easy sample exchange but also requires a sufficiently large sample diameter D of 15 mm to avoid specimen sliding. The sample dimensions are a compromise between the requirements mentioned above.

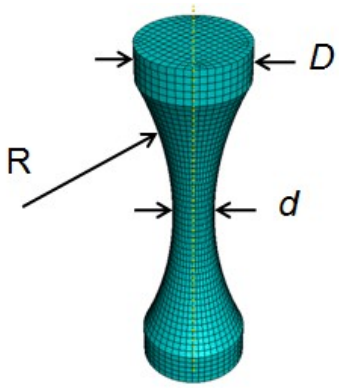

Fig. 7: Model of specimen geometry S1 (Hourglass-shaped specimen) for uniaxial compression and tension tests (R = 50 mm, *D* = 15 mm, *d* = 6 mm)

The measurement of intrinsic material properties requires the specimens to be free of defects from machining. Special attention has to be put on avoiding surface damage introduced during the sample preparation. The samples were thus carefully ground and polished not to create surface grooves or damage WC grains (see Fig. 8).

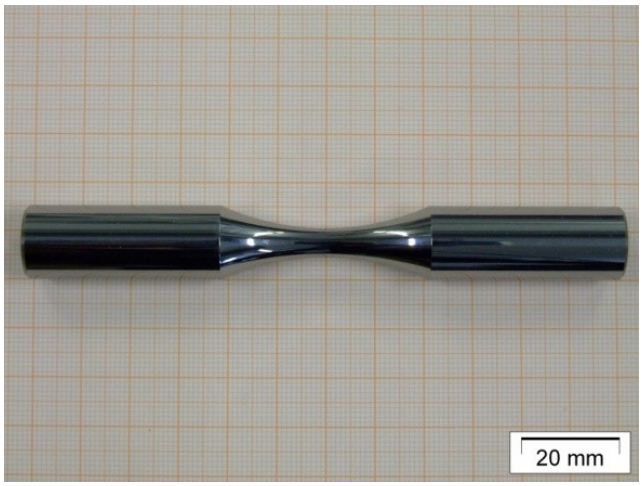

Fig. 8: Specimen geometry S1 (Hourglass-shaped specimen, minimum diameter = 6 mm) tested in uniaxial tension and compression tests

5.1.2 Testing setup

Static and cyclic uniaxial tests under compression and tension loading conditions were performed using a servo-hydraulic testing facility, “Instron 8803”, with a maximum load of 250 kN (see Fig. 9). The testing machine is encapsulated by transparent walls to

protect the operator from sample splinters that may be emitted at high velocities when samples fail. Meticulous efforts are necessary to guarantee perfect alignment of the testing facility and the specimen to avoid sample buckling in the case of compression loading. Strain measurements were performed contactlessly with a Laser extensometer P-2S-50 / 400 Hz of the company "Fiedler Optoelectronic GmbH" with a class of accuracy of 0.2 and resolution of 0.1 µm. All uniaxial tests described in this work were performed at room temperature in ambient air.

Fig. 9: Servo-hydraulic testing device "Instron 8803"

5.1.3 Strain measurement accuracy

The accuracy class *X*, as defined in the standard [52], describes the deviation of the measured elongation from the correct elongation. The value of *X* for the used laser extensometer is 0.2 which means that the maximum deviation is ± *X* % or ± 3 times *X* µm - whichever is larger [52]. For the strain values determined experimentally at a gauge length of 8 mm this means that the absolute error made when measuring the

strain, reaches 7.5% at strain values of 10^{-4} (0.01%) and 75% at strain values of 10^{-5} (0.001%). The laser extensometer used to measure the strain is capable of resolving length changes of 0.1 µm which is 1/800,000th of the gauge length.

On a cylindrical specimen the relative error committed when measuring the strain becomes smaller with increasing gauge length. In the present case of a non-constant sample diameter the necessary corrective measures in terms of strain become more elaborate as the gauge length increases. A gauge length of 8 mm is chosen as a compromise between the mentioned effects. One can conclude that differences in strain values presented in this work smaller than 0.01% should not be regarded as significant.

5.1.4 Strain correction

The maximum strain values recorded in uniaxial tension and compression tests are underestimated due to the non-constant sample diameter and need to be corrected. A procedure to perform this correction is suggested and described briefly.

Fig. 10 represents a sketch of the used model which is referred to as “disk model”. It consists of five disks exhibiting the diameters corresponding to the sample’s actual diameter at the respective position in the axial direction, referred to as *y*-direction. The sample volume within the gauge length of 8 mm with the minimum sample diameter in its centre has a symmetry plane in the *x*-*z* plane. Therefore only half of the gauge length is considered in the simulation. The centres of the disks are arranged equidistantly; only half of the disk of minimum diameter is part of the model.

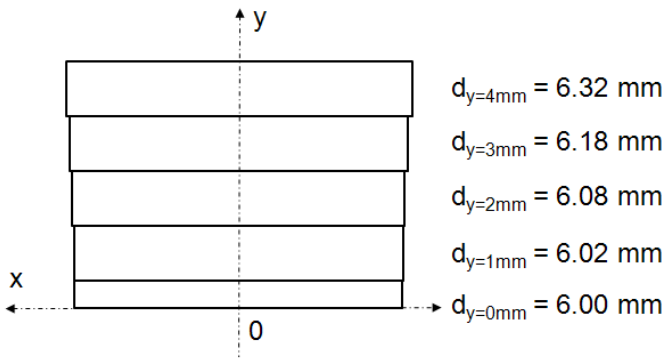

Fig. 10: Disk model of gauge length of specimen geometry S1 (non-constant diameter) used for strain correction in collected stress-strain curves

Experimentally determined values of load applied to the specimen and corresponding strain, both varying with time, are input for the procedure correcting the strain values at individual points of the stress-strain curve. These points, being parts of the actual stress-strain curve at the minimum diameter, are then fitted via a mathematical function approximating the actual stress-strain curve. To attain one point of the actual stress-strain curve the following steps are performed:

A stress value for each individual disk of the model is calculated corresponding to its diameter and the force applied to the specimen at a certain point in time during the test. Then all the strain values of the experimentally determined stress-strain curve are multiplied by a factor x, x being $1 < x < 1.15$ in the investigated cases. This leads to an assumptive stress-strain curve that is used to assign a strain value to each of the disks according to their stress values - if necessary performing an interpolation between data points of the physically measured stress-strain curve. The strain values of all the disks at a certain value of force applied to the sample are then averaged and compared to the strain value found experimentally. If the two strain values differ, x is changed and the procedure is repeated in an iterative manner until they are equal. This procedure should be performed for one point at the end of the elastic regime and three points in the plastic regime of the stress-strain curve. In the present work, one of the three points in the plastic regime is chosen at two percent strain, the other two are placed equidistantly in terms of strain to facilitate fitting the points via an exponential function.

To determine the Young's modulus of the material the linear part of the measured stress-strain curve, omitting data points up to 200 MPa, is approximated with a linear function up to stress levels were the first deviation from linear behaviour is found. For the various grades the onset of plastic deformation varied between 1450 MPa and 4300 MPa.

Now, the linear function and the exponential function can be used to simulate the experimental results, in the elastic and plastic regime respectively, assigning strain values to the individual disks according to their stress values and comparing the result with the experimentally determined data.

For the determination of the Young's modulus and the comparison of simulated and measured stress-strain curves, the disks of the disk model were subdivided to insert four new disks at y = 0.5 mm, 1.5 mm, 2.5 mm and 3.5 mm. Due to considerable time

consumption of the determination of points of corrected strain, this step was carried out with five disks only.

In Fig. 11 experimentally determined, corrected and simulated stress-strain curves attained as described above are compared.

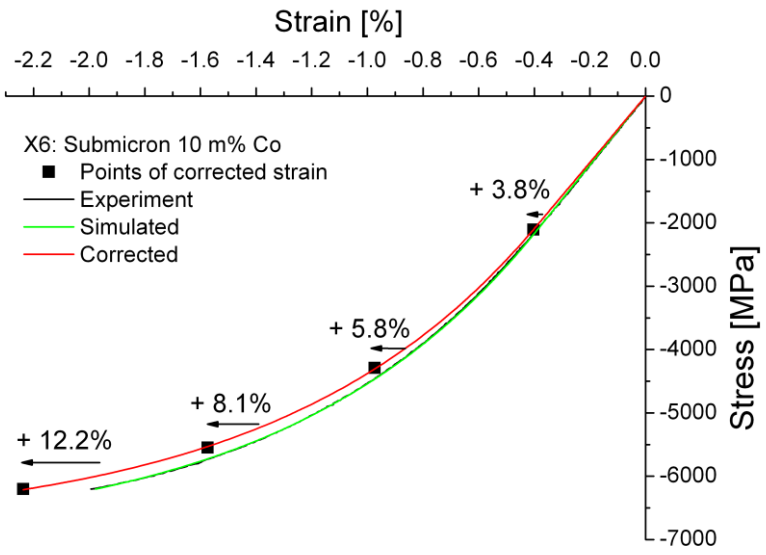

Fig. 11: Comparison of stress-strain curves of specimen geometry S1: Experimentally determined, simulated and corrected as described in the text

5.1.5 Buckling resistance and stress distribution

The feasibility of inserting a cylindrical part l_c in the axial centre of the specimen to avoid the time-consuming strain correction as well as a reduction of the minimum sample diameter d to permit testing up to higher stresses was investigated by means of FEM simulations.

An FE model of the sample, see Fig. 12, was subjected to a nominal stress $\sigma_{nominal}$ of 1000 MPa at the minimum sample diameter. The sample's resistance to buckling compared to the original hourglass shaped sample (geometry S1) as well as the distributions of hydrostatic pressure, von Mises equivalent stress and principal normal stress in the direction of loading were numerically determined.

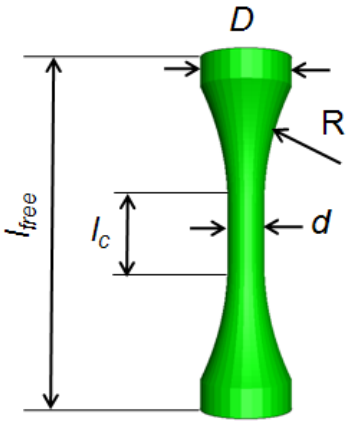

Fig. 12: Model of geometry variation of specimen geometry S1 with cylindrical part in its axial centre

To characterise the resistance to buckling of a specimen, the differential equation for elastic (Euler) buckling (see Eq. 11) along the major axis y of an axially loaded elastic staff of length l clamped on one side has to be studied [53].

$$EI_y w''(x) = -M_b(x) = -Fw(x)$$

$$\text{or} \quad w''(x) + \alpha^2 w(x) = 0 \quad with \quad \alpha = \sqrt{\frac{F}{EI_y}} \tag{11}$$

In equation (11) the symbols E represent the Young's modulus, I_y the smallest second moment of inertia, M_b the bending moment, F the applied load and $w(x)$ the axial displacement.

The solution of equation (11) is:

$$w(x) = C_1 \sin \alpha + C_2 \cos \alpha \tag{12}$$

With the boundary conditions being w(x=0) = 0 and w(x=l) = 0 it follows that $C_2 = 0$ and $\sin(\alpha)l = 0$ with the eigenvalues $\alpha_K = n\pi/l$; n = 1, 2, 3, … It follows that the Euler load, at which a kink instability occurs, can be described as [53]:

$$F_K = \alpha^2 EI_y = \frac{\eta^2 \pi^2 EI_y}{l^2} \tag{13}$$

When considering boundary conditions as present in the testing setup used in this work as depicted in Fig. 13 the specimen length l has to be replaced by l_K being 0.5 times l in

this case. The eigenvalue of buckling resistance α_K is used to compare various specimen shapes in terms of their buckling resistance.

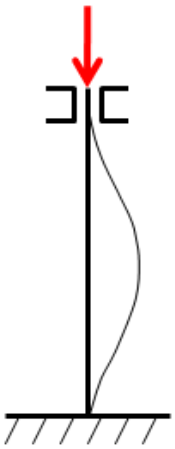

Fig. 13: Boundary conditions for buckling resistance simulation of hourglass-shaped specimen

The influence of the change in the minimum diameter d and the cylindrical length l_c on the buckling resistance of the sample geometry variants is described in Fig. 14 and Table 2. The geometry variants are compared to specimen geometry S1 with a constant radius R of 50 mm and a minimum diameter of 6 mm. In all the variants the buckling resistance is significantly reduced compared to specimen geometry S1. The fraction of buckling resistance of specimen geometry S1 is referred to as f_B.

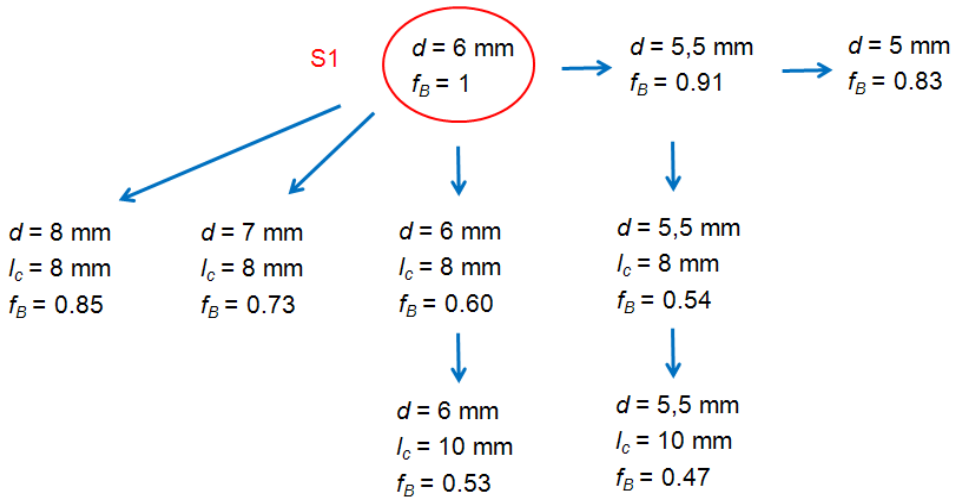

Fig. 14: Scheme of influence of minimum diameter d and cylindrical length l_c on buckling resistance. f_B represents a fraction of the eigenvalue of buckling resistance of specimen S1

Specimen geometry	d [mm]	D [mm]	l_c [mm]	R [mm]	Eigenvalue of buckling resistance α_K [m^{-1}]	Fraction f_B of buckling resistance of specimen S1 [1]	$\sigma_{Mises,max}$ [MPa]	Free sample length l_{free} [mm]
S1	6.0	15.0	0	50	24.97	1	1016	51.94
Variant 1	5.5	14.5	0	50	22.82	0.91	1015	51.94
Variant 2	5.0	14.0	0	50	20.64	0.83	1013	51.94
Variant 3	6.0	15.0	8	50	15.09	0.60	1013	59.46
Variant 4	6.0	15.0	10	50	13.22	0.53	1013	61.46
Variant 5	5.5	14.5	8	50	13.51	0.54	1012	59.46
Variant 6	5.5	14.5	10	50	11.77	0.47	1012	61.46
Variant 7	7.0	15.0	8	50	18.15	0.73		57.19
Variant 8	8.0	15.0	8	50	21.33	0.85		54.76
Variant 9	5.5	15.0	8	50	13.53	0.54		60.54

Table 2: Influence of minimum diameter d and cylindrical length l_c on buckling resistance α_K and von Mises equivalent stress maximum; $\sigma_{nominal}$ is 1000 MPa

Studying Fig. 14 closely it also becomes apparent that the influence of the cylindrical portion l_c on the specimens' resistance to buckling is stronger than that of the reduction in minimum diameter d. When l_c is zero and d is reduced from 6 mm to 5.5 mm and 5 mm, the eigenvalue of buckling resistance α_K significantly drops down to 91 % and 83 % of the value of the specimen geometry S1 respectively. Inserting cylindrical portions of 8 mm and 10 mm with an unchanged minimum diameter of 6 mm results in even more drastically reduced buckling resistance values of 60 % and 53 % of the reference value.

Furthermore, the minimum diameter was reduced to 5.5 mm in addition to the insertion of cylindrical length portions of 8 mm and 10 mm. As a result buckling resistance values drop to 54 % and 47 % of the value of the sample geometry S1 respectively.

When the cylindrical length ought to be retained, as in the present case, an option to attain a buckling resistance value similar to the one of geometry S1 is to increase the

minimum sample diameter. Increasing it from 6 mm to 7 mm and 8 mm, each with a cylindrical length of 8 mm, the buckling resistance values are 73 % and 83 % of the reference value respectively. In these cases the maximum stress values achievable with the available testing equipment are reduced compared to the case of geometry S1, from about 8800 MPa to values of 6240 MPa and 4780 MPa respectively. On the one hand this would decrease the extent to which the stress-strain curve of an investigated material could be determined, on the other hand, the time consuming strain correction as described in 5.1.4 would not be necessary.

Comparing geometry variants 5 and 9 that differ in free sample length l_{free} by 1.08 mm, one can observe that variations as small as this do not significantly alter buckling resistance, as it is 54 % of the reference value in both cases. This result indicates that small variations in free sample length from one uniaxial test to the next do not significantly alter buckling behaviour of the specimens. The values of d and l_c have a far more pronounced influence on buckling resistance.

As displayed in Fig. 15 the distributions of hydrostatic pressure is more homogeneous in the geometry variants with a cylindrical portion than in the hourglass-shaped ones. The maximum value of 350 MPa in specimen S1 is about 5 % higher than in the ideal case of purely uniaxial loading conditions for which a value of one third of the nominal stress of 1000 MPa is expected. In the specimens with a cylindrical part the maxima of hydrostatic pressure (see Fig. 15), principal normal stress in the direction of loading (see Fig. 16) and von Mises equivalent stress (see Fig. 17) are located at the ends of the cylindrical part l_c.

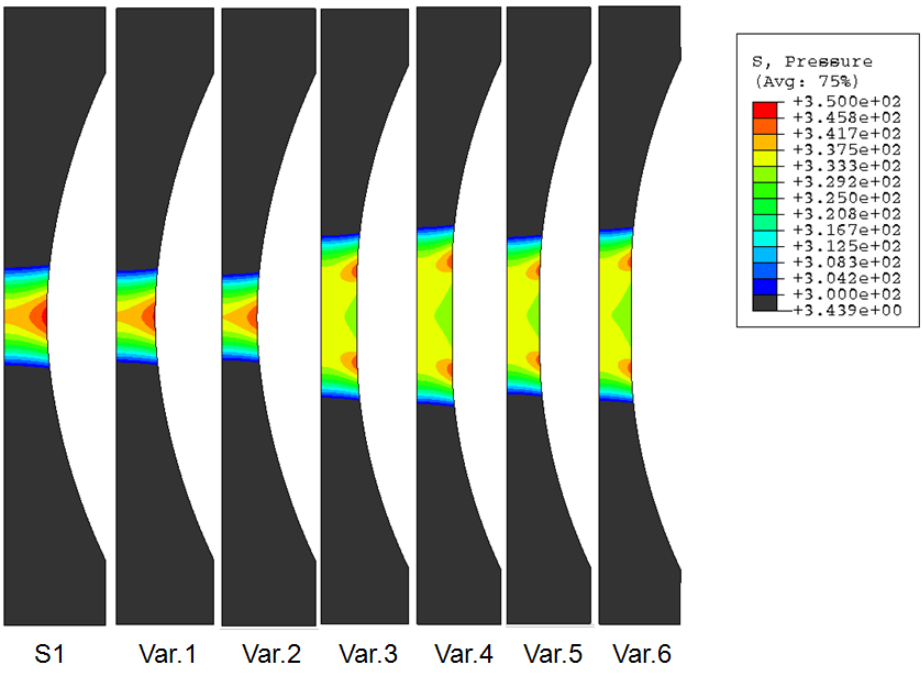

Fig. 15: Distribution of hydrostatic pressure varying with minimum diameter and cylindrical portion as described in the text, $\sigma_{nominal}$ is 1000 MPa

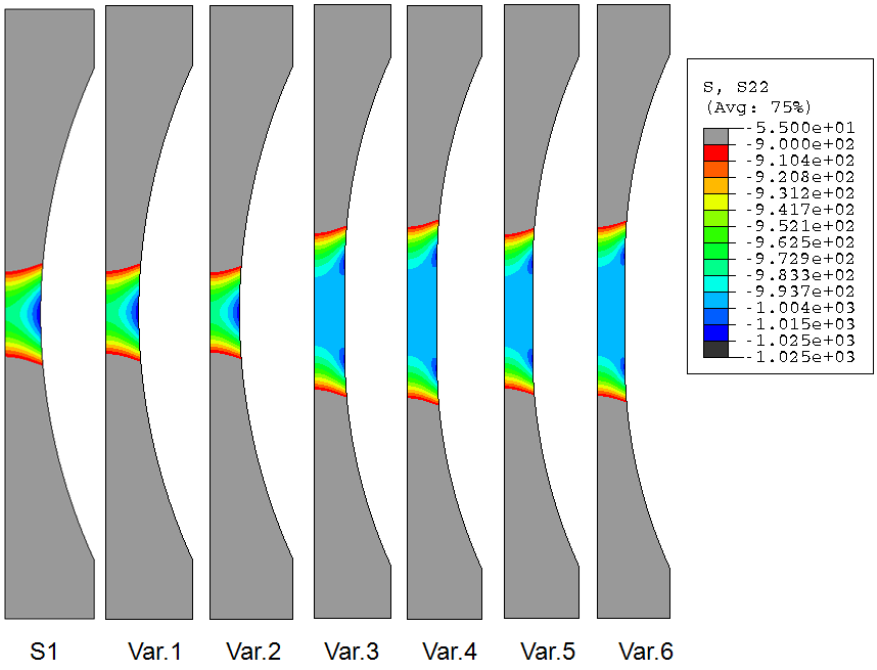

Fig. 16: Distribution of principal stress in axial direction varying with minimum diameter and cylindrical portion as described in the text, $\sigma_{nominal}$ is 1000 MPa

For the geometry S1, calculated values of the maximum and minimum von Mises equivalent stress range from 950 MPa in the centre of the specimen (see leftmost pattern in Fig. 17 b) to 1016 MPa in regions close to the sample surface at the minimum diameter (see Table 2 and leftmost pattern in Fig. 17 b). This is equivalent to a deviation from the nominal stress of 1000 MPa of 4.5% and 1.6% respectively. One can conclude that the goal of avoiding unacceptable stress concentration sites in the specimen was fulfilled to a satisfying degree.

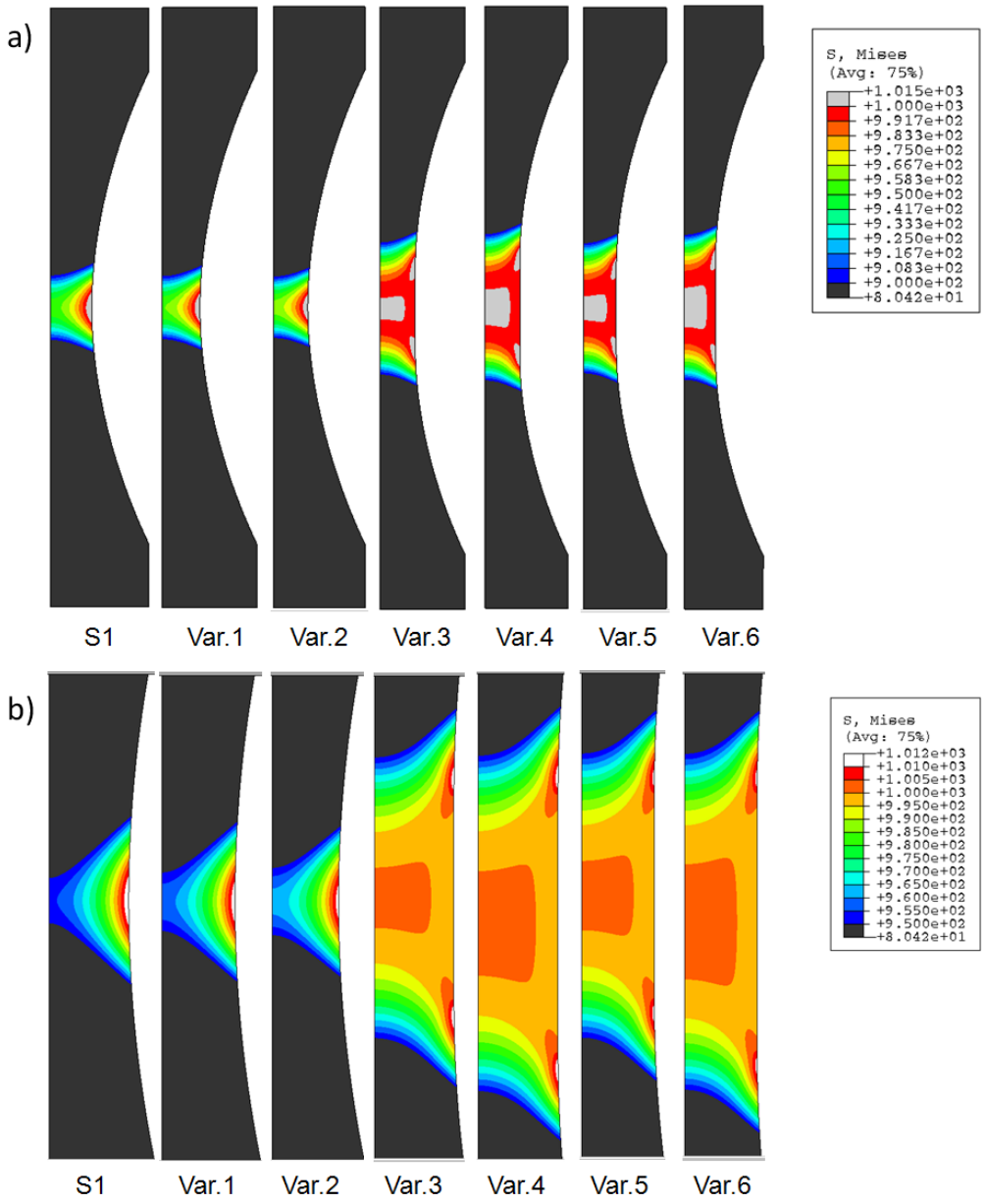

Fig. 17: Distribution of von Mises equivalent stress varying with minimum diameter and cylindrical portion as described in the text and Table 2 – b) shows detail of a); $\sigma_{nominal}$ is 1000 MPa; for specimen dimensions see Table 2

5.1.6 Test reproducibility

Reproducibility of the uniaxial compression test was assessed by means of repeating the tests. Fig. 18 shows stress-strain curves determined from five samples of the hard metal grade X6 which coincide to a satisfying degree [54]. Please note that the stress and strain correction to account for the hourglass shape of the sample, necessary for quantitative evaluation of stress-strain data, was not performed in these curves since only qualitative reproducibility was verified.

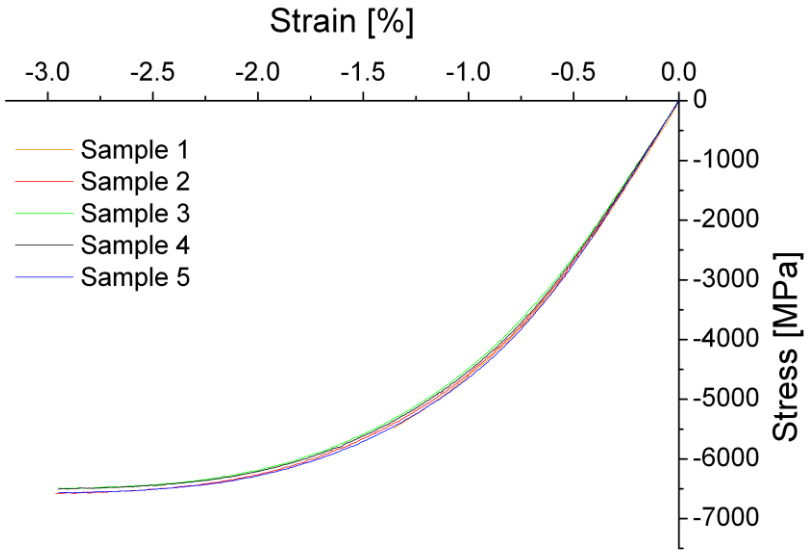

Fig. 18: Example for the reproducibility of uniaxial compression test results for the hard metal grade X6

5.2 Bending loading conditions

In the current section, various specimens used to characterise WC-Co hard metals under bending loading conditions are presented. One of the specimens is extraordinary due to its dimensions in the micrometre regime. The field of materials research utilising samples as small as this has attracted considerable interest in recent years. Experiments have been described for various specimen geometries and loading conditions in literature. Mechanical tests under compression loading [55], tensile loading [56] and

bending [57] were performed with specimens in micrometre dimensions. Also, micro-fracture experiments of brittle materials [58]-[60] were accomplished.

5.2.1 Specimen design and manufacture

Four different kinds of bending specimen varying in size and geometry, denoted as S2 to S5, were used in the present work as listed below:

"S2" represents a cylindrical rod with a diameter of 3.16 mm and a length of 38 mm (see Fig. 19). Careful mechanical grinding and polishing was performed to ensure the avoidance of surface damage.

"S3" exhibits a cylindrical shape with a diameter of 1 mm and a length of 6 mm as depicted in Fig. 20. Specimens were carefully ground and polished mechanically to avoid surface damage.

"S4" is a micrometre sized cantilever as depicted in Fig. 21. Specimens were machined from a plate-like preform (3 mm x 1 mm x 0.1 mm) which was thinned via an argon ion slicing technique [61]. This procedure is utilised to minimise FIB milling time and gallium ion induced damage in the subsequent cantilever production. Low energy argon ions strike the preform in a direction perpendicular to the surface of the dimensions 3 mm x 0.1 mm and remove material. In this manner, a crescent shaped lamella with almost parallel flanks and a thickness of several micrometres is produced [61]. The cantilevers' final geometry was then manufactured via FIB cutting. Their sizes varied from about 16 µm x 10 µm x 60 µm to 6 µm x 9 µm x 40 µm. The utilised gallium ion currents at an acceleration voltage of 30kV were between 20 nA and 2 nA for course milling and 500 pA for the final polishing steps.

"S5" is a cylindrical rod with a diameter of 4.95 mm and a length of 60 mm (see Fig. 22). The specimens were cut out of bulk hard metal pieces via electrical discharge machining (EDM). Some of the specimens of geometry S5 used in this work were also ground mechanically after EDM cutting.

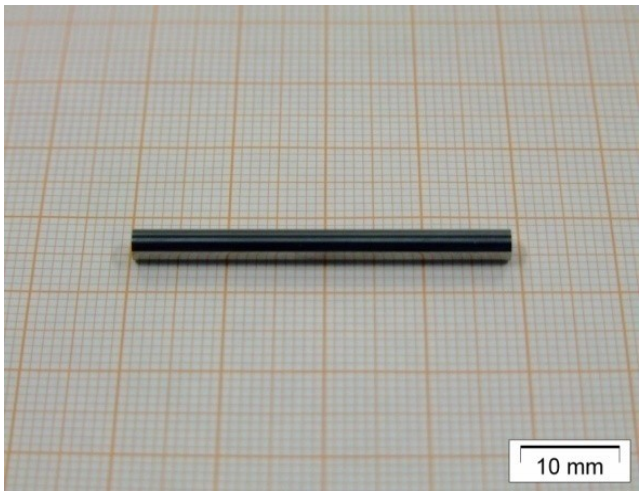

Fig. 19: Specimen geometry S2 (Cylindrical rod, diameter = 3.16 mm) tested in a four-point bending test

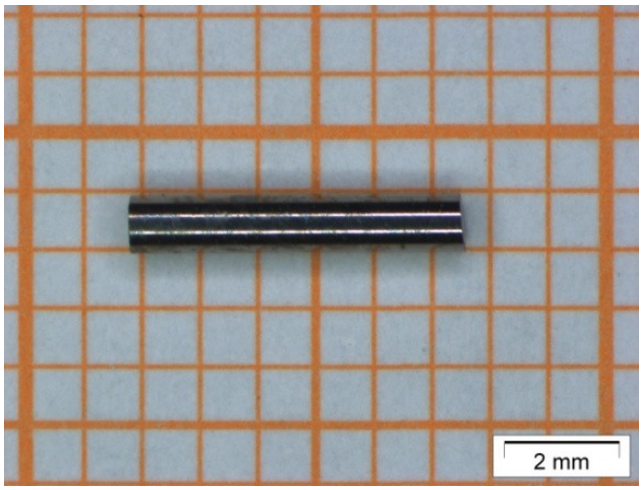

Fig. 20: Specimen geometry S3 (Cylindrical rod, diameter = 1 mm)

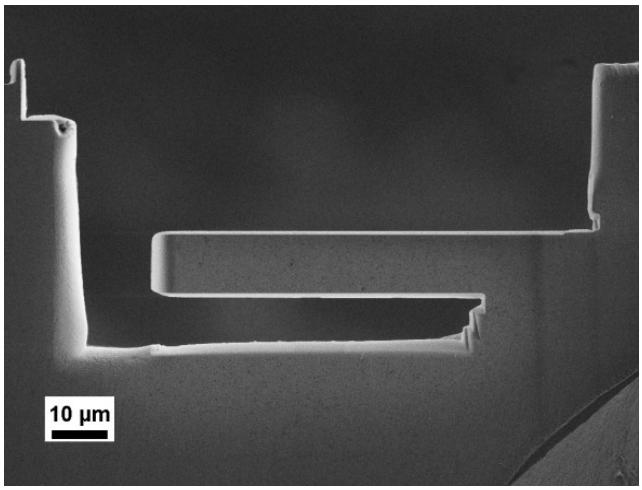

Fig. 21: SEM micrograph of specimen geometry S4 (Cantilever with rectangular cross section, thickness = 10 µm)

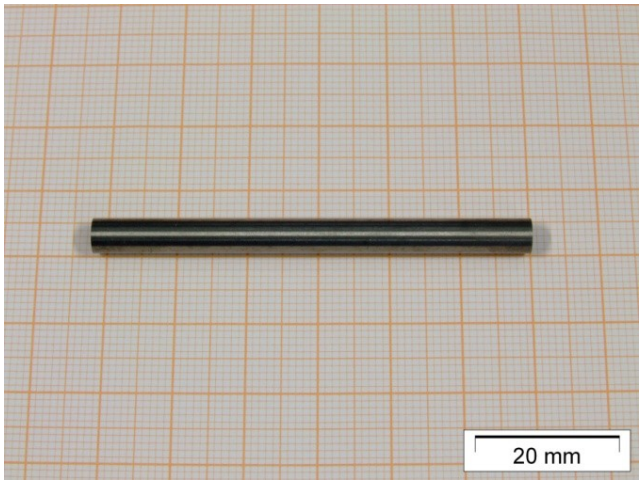

Fig. 22: Specimen geometry S5 (Cylindrical rod, diameter = 4.95 mm)

5.2.2 Testing setup

Specimen geometries S2 and S5 were tested in a four point bending test setup with an inner and outer span length of 15 and 30 mm respectively (see Fig. 23). Cylindrical rods with a 5 mm diameter, made of hard metal grade X9, were used as supports. The upper loading platen was fixed in all three spatial directions whereas the lower platen was able to rotate around one axis to ensure parallel alignment of the loading platens.

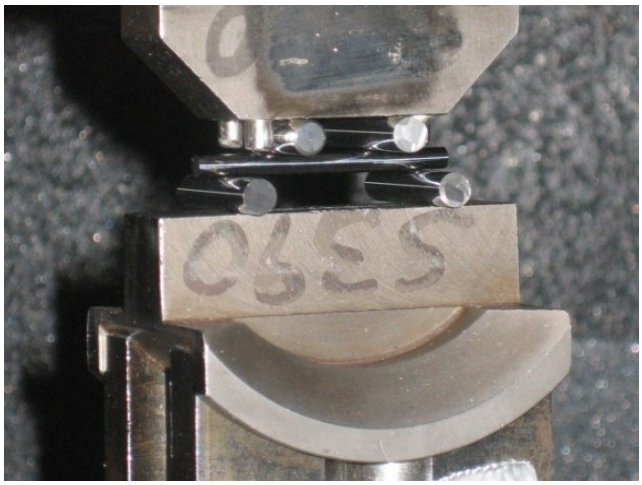

Fig. 23: Four point bending test setup with inner and outer span length of 15 and 30 mm

To prevent shattering of the specimen after breaking, a commonly available heat shrink tube was attached to the four point bending specimens as shown in Fig. 24. Upon fracture the tube keeps the specimens from hitting the steel structure below it which would spoil the formed fracture surfaces. In this manner the number of intact fracture surfaces and therefore the number of origins of fracture that could be identified was enhanced drastically compared to experiments performed without the shrink tubes.

The typical fracture path observed in four point bending specimens made of WC-Co hard metal is also visible in Fig. 24, indicated by red dashed lines for the left and central crack branch. Fracture initiates close to the region indicated by the black arrow and proceeds upwards. The peculiar crack path can be rationalised considering the following thoughts:

At high crack propagation velocities, in the order of considerable fractions of the speed of sound that cracks can reach in brittle solids, the crack bifurcates and deviates from the direction normal to the direction of maximum stress [62]. Several explanations to this kind of behaviour have been proposed. One involves a distortion of the crack tip stress field of swiftly moving cracks that shifts the maximum local tensile stress away from the initial crack plane onto an inclined plane [62]. Another explanation claims that secondary fractures ahead of the crack tip occur, varying in distance from the primary crack's tip according to the primary crack's stress field intensity. The secondary fractures are consumed by the primary one, forming severe fracture surface roughening [62]. A third explanation, valid especially for small specimens, is the possible

interaction of elastic stress waves emitted from the advancing crack tip after reflection from the specimen's boundaries [62]. Another possible explanation for specimens with inhomogeneous stress distributions, as with the bending specimen in Fig. 24, is that the crack avoids regions in the specimen that are still under compressive stress as it approaches because the crack propagates about as fast as internal stresses can relax.

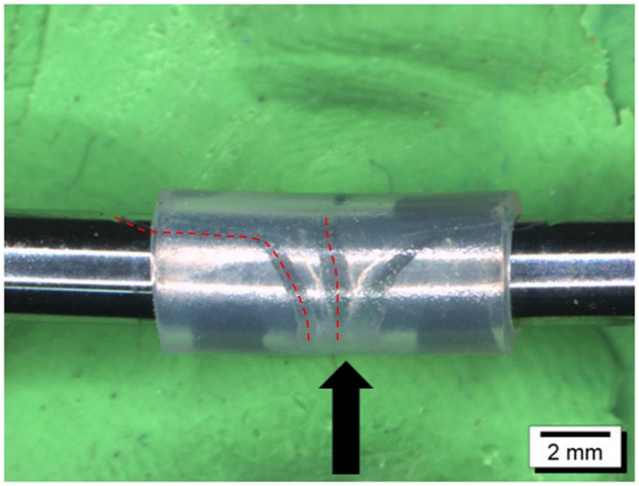

Fig. 24: Shrink tube attached to a four point bending specimen showing typical fracture paths for four point bending loading conditions

The specimen geometry S3 was tested in a three point bending test setup with an outer span length of 4.5 mm (see Fig. 25). The supports represented cylindrical rods of a 1 mm diameter made of hard metal grade X9. A commonly available adhesive tape placed between the specimen and the support rods served to protect the formed fracture surfaces in this case.

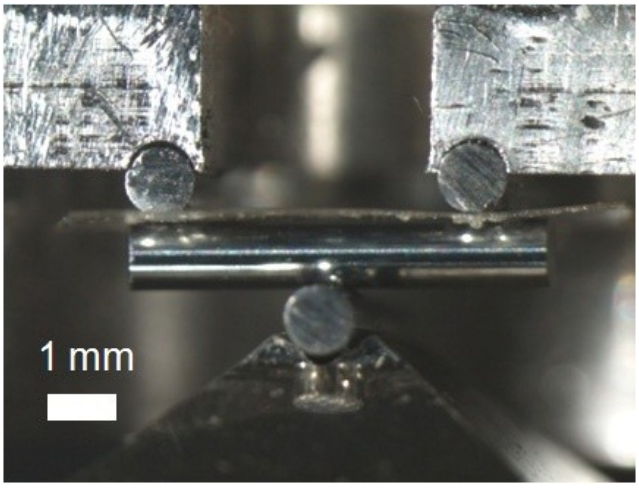

Fig. 25: Three point bending test setup with an outer span length of 4.5 mm. Note: adhesive tape placed between specimen and support rods

All bending tests except for the experiments performed with the microcantilever specimens (geometry S4) described in this work were performed at room temperature in ambient air.

Samples of geometry S4 were tested in situ in an SEM (LEO 982), equipped with a piezo-electrically controlled cube corner micro-indenter (ASMEC, UNAT) as shown in Fig. 26. The applied testing forces were in the mN regime.

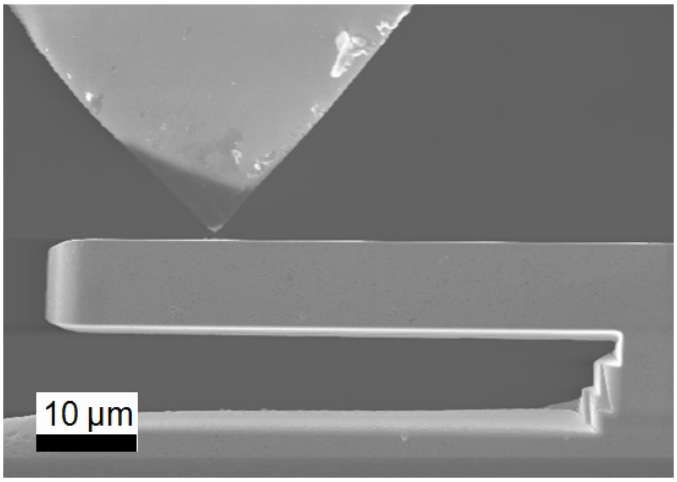

Fig. 26: In situ loading of a micrometre sized cantilever specimen (S4) in an SEM by a piezo-electrically controlled cube corner micro-indenter

6 Material properties under monotonous loading conditions

In engineering applications of condensed matter, material data such as yield strength or fracture strength are indispensible for the reliable design of components and tools. In the present chapter, a brief overview of the material data of WC-Co hard metals existing in literature will be given and the contribution of the current work to the understanding of the mechanical properties of hard metals will be illustrated.

In the past, the material testing techniques for uniaxial loading conditions described in literature and in the introduction to section 5 have been applied to hard metal grades of WC grain sizes larger than 1 μm, revealing the elastic-plastic stress-strain behaviour of WC-Co hard metals under compression loading conditions for binder phase contents ranging from 4 to 44 wt % [47]-[51]. In the case of tensile loading conditions, elastic-plastic material behaviour prior to specimen failure was observed in hard metal grades that contained amounts of Co binder down to 30 wt % [46]. No information on stress-strain data determined under uniaxial loading conditions for ultrafine grained hard metal grades is available in literature today.

In the following, the influence of microstructural parameters on flow behaviour under compression loading conditions, as well as the impact of defect size on the fracture behaviour under tensile loading conditions will be discussed.

6.1 Influence of microstructure on flow behaviour

The amount of binder metal as well as the size and shape of the binder metal regions in a hard metal have an influence on its flow behaviour, which is especially apparent under compression loading conditions. In the present section, experimentally determined levels of yield stress are presented and their dependence on parameters such as WC grain size, Co binder content, mean free path in the Co binder λ_{Co} and matricity of the Co binder M_{Co} is discussed. Factors influencing flow behaviour in WC-Co hard metals are briefly reviewed.

6.1.1 Uniaxial compression loading conditions

The stress-strain response under uniaxial compression and tension loading conditions of at least three specimens of geometry S1 was determined for the hard metal grades X1 to X10. In Fig. 27 representative examples of flow curves including the necessary strain correction described in section 5.1.4 are shown for the various hard metal grades [63]. The most remarkable result is that even the hardest hard metal grades with ultrafine WC grains and very low Co binder content exhibit considerable plastic deformation under compression loading conditions.

The stress-strain response under compression also varies strongly according to hard metal composition. In Table 3 the compressive yield limits $R_{p0.05}$, $R_{p0.1}$ and $R_{p0.2}$ are displayed along with the Young's moduli in compression and tension determined using specimens of geometry S1 [63]. Plastic flow starts at flow strength levels ($R_{p0.05}$) between about 2400 MPa and 5700 MPa. The results in terms of flow stress for the hard metal grades X1, X3, X4, X6 and X9 that were also published in [54] are in good agreement with analytical calculations of flow stresses performed in recent literature work [64]. Please note that the hard metal grades' nomenclature differs in [54] and [63] due to the higher number of hard metal grades investigated in [63].

In case of tension loading conditions, all hard metal grades except the grades X1, X2, X5 and X8, containing the highest binder content investigated, exhibit linear stress-strain behaviour before failure. The mentioned grades which contain 12 wt % Co binder show some small amount of ductility also under tensile loading. Please note that stress-strain curves in compression were determined up to strain values of 3% strain but due to reasons of simulation accuracy in strain correction they are displayed only up to smaller strain values in Fig. 27.

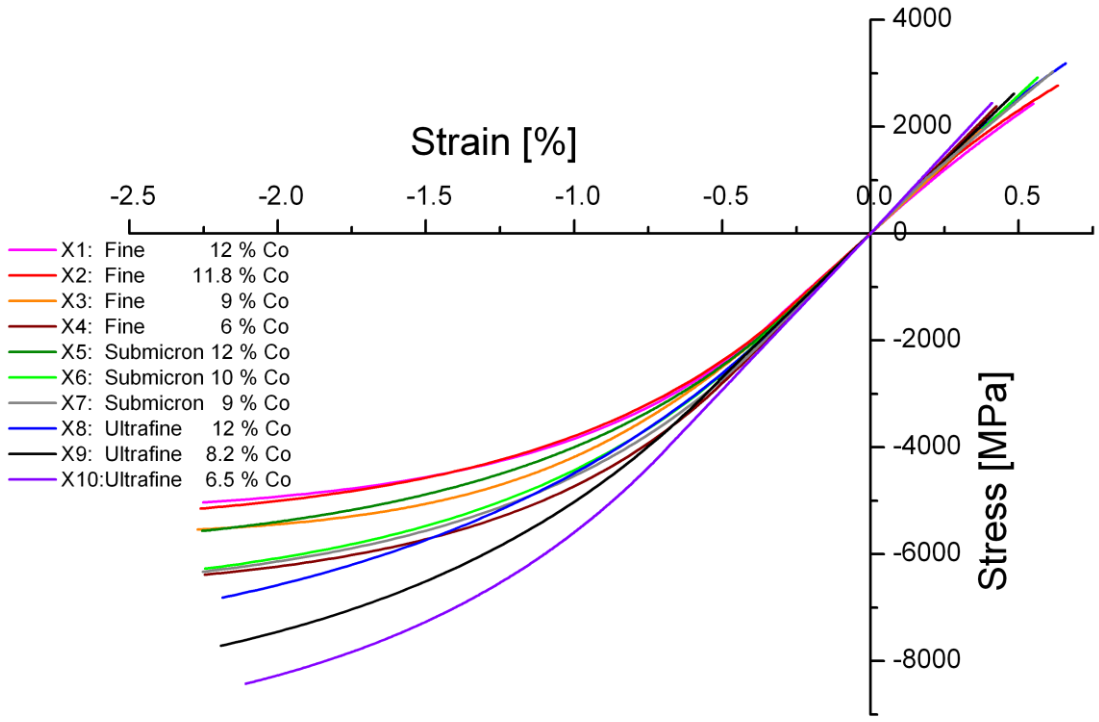

Fig. 27: Stress-strain curves of hard metal grades varying in Co binder content and WC grain size from 6 to 12 wt % and from 0.2 to 1.3 µm respectively [63]

	Compression				Tension
Grade	$E_{compression}$ [GPa]	$R_{p0.05}$ [MPa]	$R_{p0.1}$ [MPa]	$R_{p0.2}$ [MPa]	$E_{tension}$ [GPa]
X1	509 ± 8	2560 ± 270	3000 ± 200	3560 ± 170	497 ± 8
X2	497 ± 15	2610 ± 100	3030 ± 70	3570 ± 50	513 ± 30
X3	540 ± 5	2870 ± 170	3440 ± 100	4080 ± 70	528 ± 8
X4	566 ± 4	3690 ± 160	4250 ± 120	4850 ± 70	557 ± 15
X5	521 ± 13	2710 ± 90	3210 ± 70	3810 ± 60	496 ± 14
X6	524 ± 8	3470 ± 30	3980 ± 30	4580 ± 35	528 ± 11
X7	533 ± 22	3690 ± 270	4150 ± 210	4740 ± 150	551 ± 8
X8	533 ± 21	3570 ± 360	4150 ± 320	4890 ± 250	515 ± 14
X9	540 ± 11	4820 ± 270	5370 ± 230	6080 ± 180	535 ± 9
X10	590 ± 8	5710 ± 90	6280 ± 80	7000 ± 60	592 ± 9

Table 3: Young's modulus in compression and tension along with yield strength R_p in compression of tested hard metal grades [63]

Young's modulus is not significantly different in tension and compression and varies according to the amount of Co binder in the material between values of 480 GPa and

600 GPa for the investigated grades as displayed in Fig. 28 and Table 3. No significant influence of WC grain size on Young's modulus was observed for the tested materials. This result confirms the findings from literature that investigate the dependence of Young's modulus on composition and microstructure via a dynamic resonance technique [65]. The values of Young's modulus determined in the present work are roughly 10% lower than those determined via the resonance method for hard metal grades of the same binder content [65]. According to [34], one explanation for this discrepancy could be the very low strain level, close to the origin of the stress-strain curve, at which the material response is determined in the resonance technique, as opposed to the large strain range over which the elastic properties are averaged in the present work. Another reason could be the inhomogeneous stress distribution in the specimen used in the current investigation (see Fig. 17). Please note that the determination of Young's modulus in some particle reinforced materials is sometimes difficult due to the occurrence of an entirely non-linear stress-strain curve without any linear elastic region [66],[67].

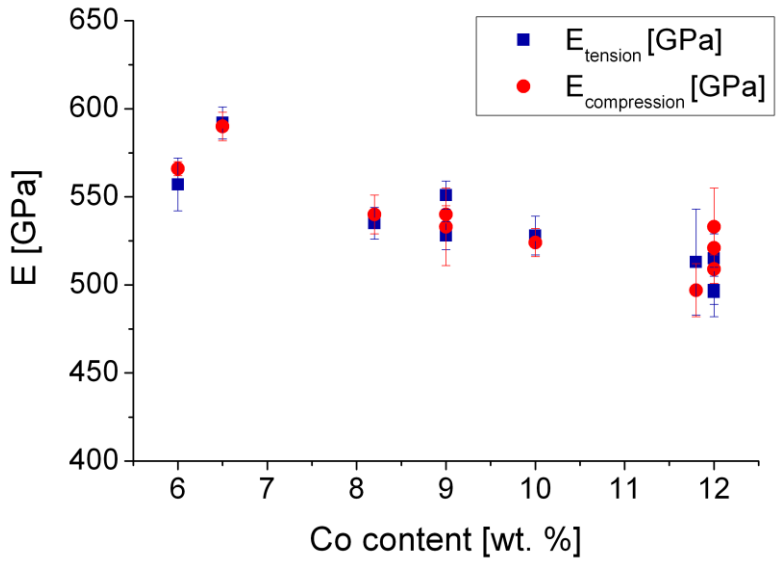

Fig. 28: Young's moduli as a function of Co binder content determined using specimens of geometry S1

When plotting the stresses at which 0.05%, 0.1% and 0.2% plastic strain occurred in the determined stress-strain curves, the strong influence of the binder content and the WC

grain size on the flow behaviour under compressive loading becomes apparent (see Fig. 29). The values of the flow stress rise significantly as the mean WC grain size and binder content decrease [63].

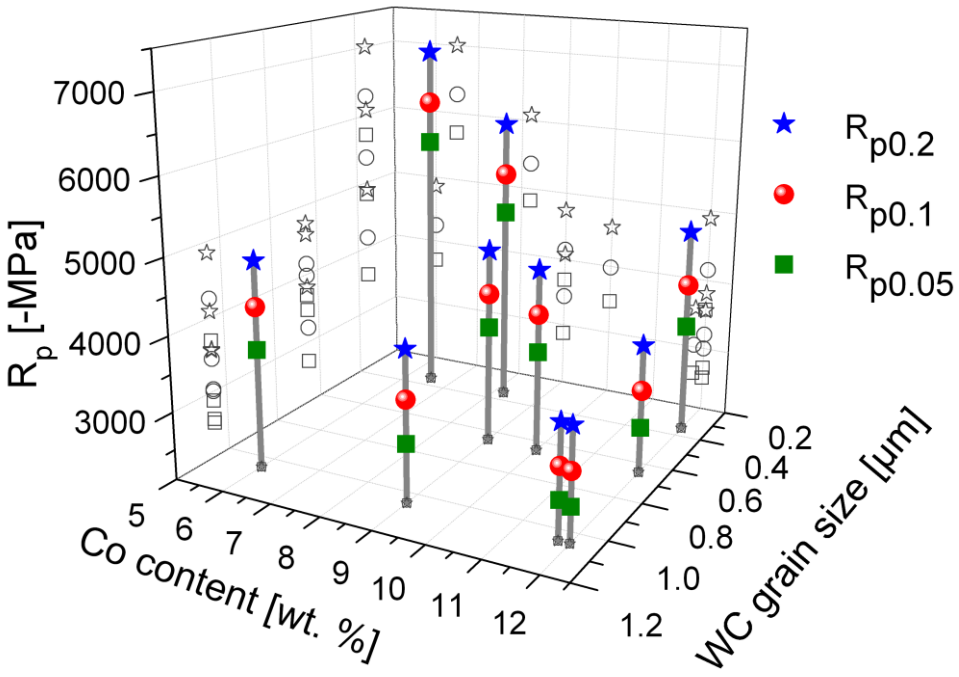

Fig. 29: Static flow stresses of WC-Co hard metals in compression as a function of WC grain size and Co binder content [63]; open symbols represent two-dimensional projections of the data

This behaviour can be rationalised discussing a few points influencing plastic deformation in WC-Co composite materials. At low levels of stress and strain dislocation motion occurs mainly in the Co binder phase [68] which justifies the consideration of its properties in terms of plastic deformability to be dominant for the composite as a whole, at least in early stages of plastic deformation. The plastic deformation behaviour of the Co phase, which is important for the overall behaviour of WC-Co alloys, is at the least influenced by the following factors:

(i) Solid solution hardening through dissolved W and C in the Co binder [69]-[72]. There are indications that the C content of the Co binder is very low [72]. The presence of W and C in solid solution also leads to a stabilisation of the face-centred-cubic (fcc) modification of the Co phase [70] that is subject to

(ii) a deformation-induced martensitic transformation to the hexagonally close-packed modification (hcp) which is thermodynamically stable at room temperature [42],[70],[73]-[75].

(iii) Residual stresses influence the flow behaviour of metal matrix composites [76]. The extent of their influence may depend on their magnitude, on their partial relaxation upon loading [77], phase matricity [23], phase size [78] and on the ratio of residual stress to applied stress [79].

(iv) The dimensional constraint of plastic flow [80] present when dislocation slip length in the binder is limited because dislocations are repelled from the WC/ Co interface in the narrow binder channels [69].

(v) The triaxial stress state arising in the Co between WC grains [69]. It decreases the amount of deviatoric stress driving plastic deformation.

(vi) The formation of a large number of stacking fault intersections [81] during plastic deformation of the Co binder metal [82] contributes to the remarkable strain hardening ability of the composite material and is predicted to be effective up to levels of stress of 8.9 GPa [37]. The frequent occurrence of the stacking fault intersections is due to the low stacking fault energy of about 20 mJm^{-2} of the Co binder [83],[84] that leads to an extremely wide stacking fault width of about 20 burgers vectors. The intersections take the form of a doublet of sessile stair rod dislocations (Lomer-Cottrell barrier) [85] which, in contrast to the stacking faults themselves, pose considerable resistance to dislocation slipping.

Plastic deformation also of the WC phase is necessary to explain the relatively ductile behaviour of the composite material at higher levels of strain [68]. Experimental evidence for plastic deformation in the WC phase of hard metals under compressive loading is reported in literature [73],[86].

When considering all the various points influencing plastic deformation mentioned above, one can understand that at high binder content and large WC grain size items (iv) and (v) are not as effective in strengthening the WC-Co composite as compared to when Co content is low and WC grain size is small. Thus the levels of stress at which plastic

deformation sets in can be expected to rise with a decrease in Co binder content and WC grain size.

6.1.2 Influence of matricity and mean free path on flow behaviour

Considering the discrete nature of plasticity, some authors proposed a Hall-Petch-like relationship [87],[88] that involves a mean free path in the Co binder phase (λ_{Co}) to describe the hardness and flow properties of WC-Co hard metals [33],[36],[37],[89],[90] (also see items (iv) and (v) described above).

Apart from λ_{Co}, also the geometry of the Co phase regions influences the flow behaviour of WC-Co. A possibility to describe the average shape of binder phase regions, in which plastic deformation sets in at lower global stress levels than in the WC phase, is the matricity parameter, which describes to what extent a microstructural constituent forms the matrix or an inclusion in a two-phase composite (see section 3.3). A high level of binder matricity M_{Co} corresponds to highly branched Co binder regions that exhibit numerous sites of stress concentration which lower the stress level at which the onset of global plastic deformation of the composite occurs [21]. A parameter describing geometrical influences on flow behaviour (e.g. M_{Co}) shall be combined with a parameter describing the influence of the discrete nature of plasticity (e.g. λ_{Co}) to describe the stress-strain behaviour of WC-Co hard metals.

In order to correlate λ_{Co} and M_{Co} with the determined yield strength values, the same were determined from manually binarised SEM images taken from FIB polished specimens made of hard metal grades varying in WC grain size and Co content as seen in Fig. 30. To avoid loss of information about very fine details of the hard metals' microstructure, such as the shape of narrow Co binder regions, the very gentle FIB polishing technique was found to be necessary. Surface preparation techniques conventionally applied to WC-Co hard metals involving grinding, polishing and etching were found to destroy or at least obscure very fine surface features.

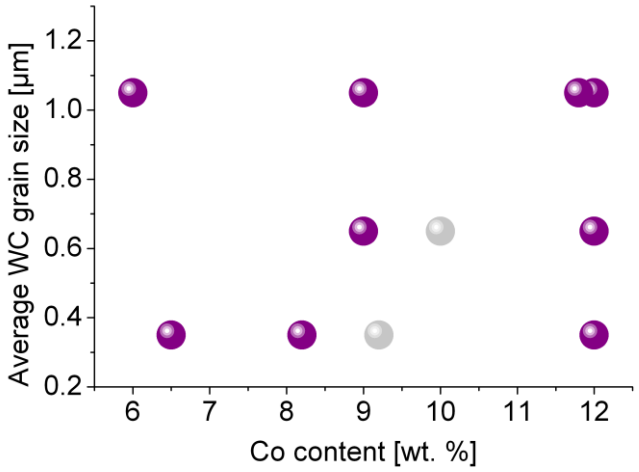

Fig. 30: Overview of hard metal grades investigated in terms of influence of binder matricity on flow behaviour as characterised by average WC grain size and Co content

Binder regions narrower than 20 nm were excluded from the analysis since their stress-strain behaviour is highly influenced by the surrounding WC material, heavily retarding plastic deformation. The linear intercept method was utilised to determine λ_{Co}, comparing the attained values for horizontal and vertical images to assure image isotropy. Binder matricity was determined evaluating Eq. 10 with the skeleton line lengths of the Co and WC phases computed from the binary images of the microstructures by a skeletonization procedure conducted in Matlab (see appendix in section 10). The results of the described evaluations are displayed in Table 4. Examples for the results of the skeletonization procedure are shown in Fig. 31 to Fig. 34.

Grade	M_{Co} [1]	λ_{Co} [µm]	$R_{p0.05}$ [MPa]	$R_{p0.1}$ [MPa]	$R_{p0.2}$ [MPa]
X1	0.352	0.32	2560	3000	3560
X2	0.355	0.30	2610	3030	3570
X3	0.349	0.25	2870	3440	4080
X4	0.314	0.20	3690	4250	4850
X5	0.369	0.18	2710	3210	3810
X7	0.326	0.19	3690	4150	4740
X8	0.322	0.09	3570	4150	4890
X9	0.283	0.08	4820	5370	6080
X10	0.224	0.05	5710	6280	7000

Table 4: Binder matricity M_{Co} along with average mean free path in the Co binder λ_{Co} and flow strength levels R_p; data visualised in Fig. 35 to Fig. 37

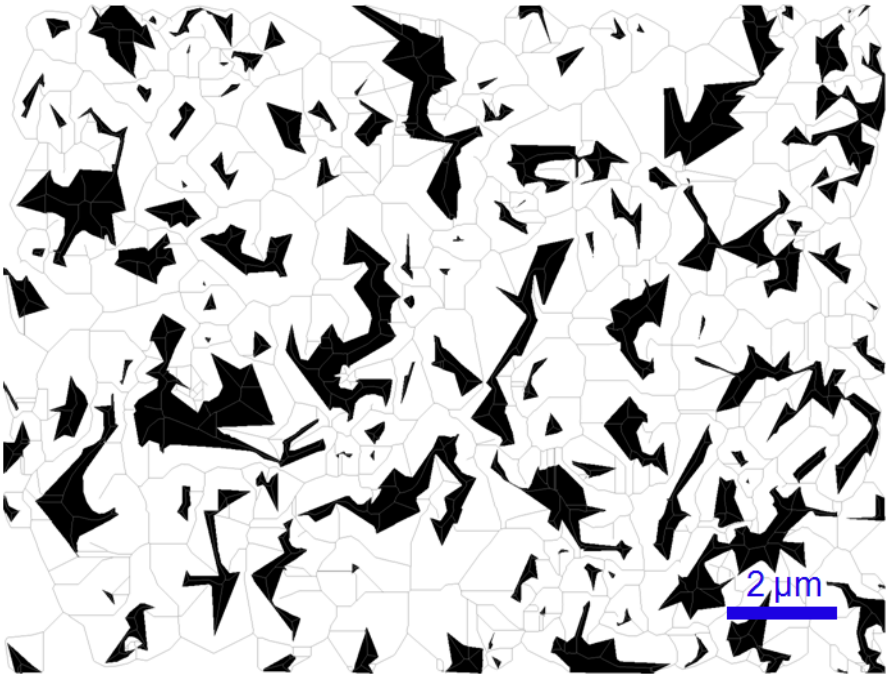

Fig. 31: Result of skeletonization procedure of the WC phase of hard metal grade X1 (skeleton lines of Co phase too narrow to be reproduced by printer), 12 wt % Co, fine WC grain size; $M_{Co} = 0.352$

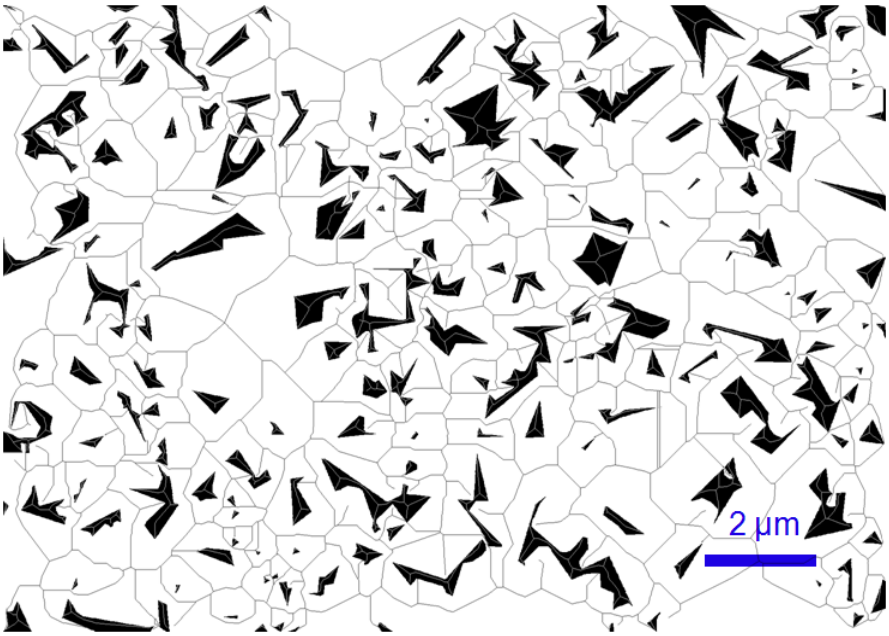

Fig. 32: Result of skeletonization procedure of the Co and the WC phase of hard metal grade X4, 6 wt % Co, fine WC grain size; $M_{Co} = 0.314$

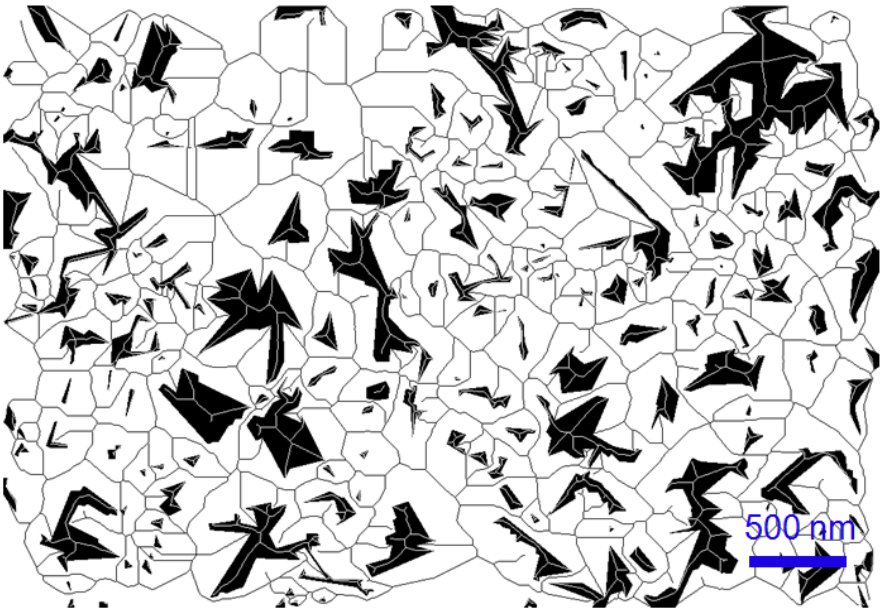

Fig. 33: Result of skeletonization procedure of the Co and the WC phase of hard metal grade X8, 12 wt % Co, ultrafine WC grain size; M_{Co} = 0.322

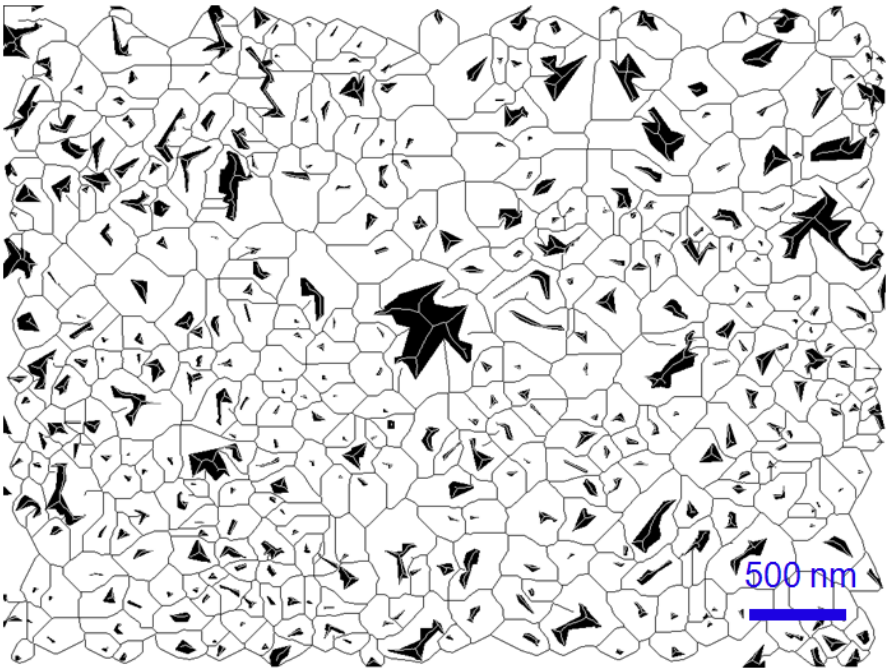

Fig. 34: Result of skeletonization procedure of the Co and the WC phase of hard metal grade X10, 6.5 wt % Co, ultrafine WC grain size; M_{Co} = 0.224

The Hall-Petch-like behaviour of WC-Co materials proposed in literature is retrieved in the current investigation when plotting the determined flow stress levels $R_{p0.05}$, $R_{p0.1}$, $R_{p0.2}$ vs. λ_{Co} (see orange line as guide for the eyes in Fig. 35 and Fig. 37). The results for

M_{Co} indicate that its reciprocal relation with flow stress found in numerical studies [21] can also be found in experiment (see green line as guide for the eyes in Fig. 36 and Fig. 37). A representation of the combined influence of λ_{Co} and M_{Co} is presented in Fig. 37.

Note that the determination of matricity values is a very laborious task and that in the present work no sufficient information on the scatter of matricity values was generated. Further investigations in the matter such as FE simulations of the stress-strain behaviour of real WC-Co microstructures could help to gain insight into e.g. the in-situ flow behaviour of the Co phase.

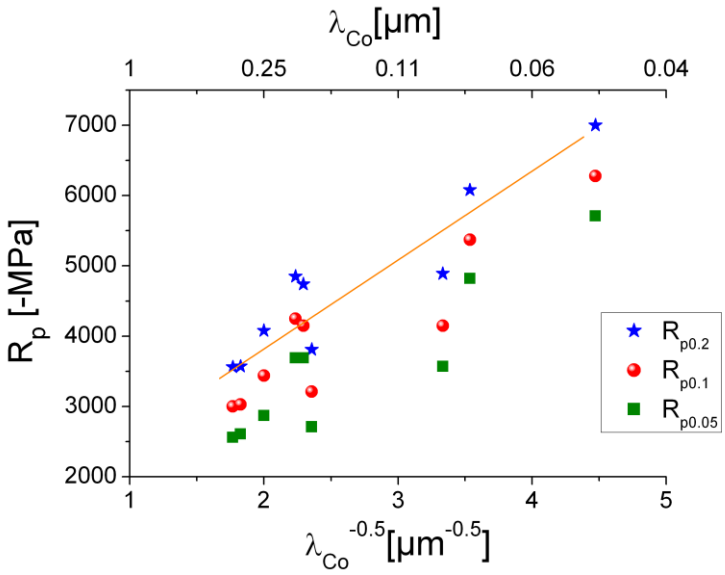

Fig. 35: Flow strength values R_p versus mean free path in Co binder λ_{Co}

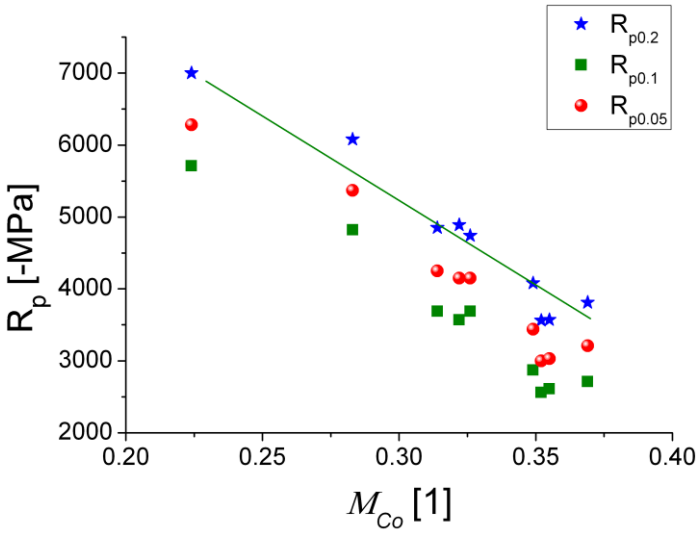

Fig. 36: Flow strength values R_p versus Co binder matricity M_{Co}

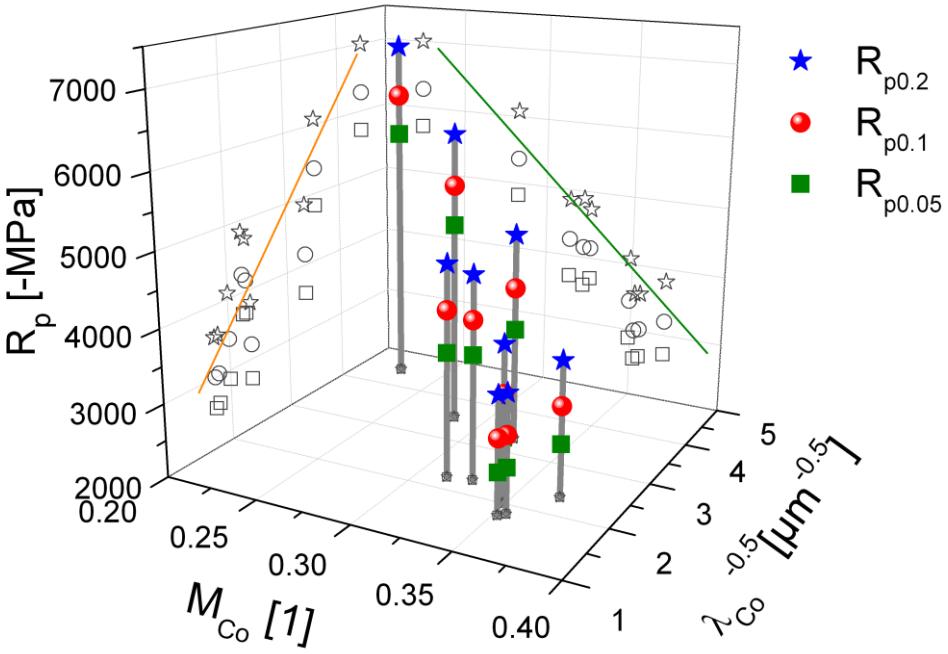

Fig. 37: Influence of binder matricity M_{Co} and inverse square root of mean free path in the Co binder λ_{Co} (Hall-Petch relation) on yield strength R_p of WC-Co hard metals; open symbols represent two-dimensional projections of the data

6.2 Influence of microstructure and specimen size on fracture behaviour

Microstructural defects represent sites of stress concentration in a material, becoming origins of fracture under tensile loading conditions. The probability of finding a defect of a certain size within a specimen correlates with the specimen's size. Therefore the load or strain a specimen can sustain depends on its microstructure and on its dimensions.

The main result presented in the current section is that tensile strength values are found to increase from minimum values of 800 MPa to about 6000 MPa when V_{eff} is varied from about 100 mm³ to about 10^{-8} mm³ by the application of various specimen geometries and testing setups. This kind of strength scaling is typical for brittle materials in which strength is defect controlled and can be explained by a size effect according to Weibull theory (see Eq. 9).

6.2.1 Uniaxial loading conditions

When looking at Fig. 27 it becomes apparent that the load bearing capacity of specimens made of hard metals in the dimensions of specimen geometry S1 is by far greater under compression loading conditions than under tensile load.

For the case of compression loading, fracture strength could not be determined because the specimens did not fracture before the maximum load capacity of the testing machine, equivalent to about 8500 MPa stress in the specimen with geometry S1, or the strain limit of 3 % was reached. Values of ultimate strength could be determined only for the materials X3 and X4 within the investigated stress and strain intervals. Values for all the other grades were denoted as greater than a certain value in Table 5.

Under tensile loading conditions ultimate strength was equal to the fracture strength and ranged from 800 MPa to 3300 MPa.

Grade	$R_{m,compression}$ [MPa]	$R_{m,tension}$ [MPa]
X1	> 5100	2391 ± 68
X2	> 5420	2663 ± 148
X3	5610	1426 ± 178
X4	6470	2110 ± 237
X5	> 5770	2910 ± 470
X6	> 6580	2761 ± 220
X7	> 6330	2433 ± 481
X8	> 7580	2539 ± 560
X9	> 8500	2449 ± 123
X10	> 8500	1500 ± 700

Table 5: Ultimate strength in tension and compression of tested materials

As any other engineering materials, hard metals are not entirely free of defects, which cause the scatter of the strength results. A variety of material defects can be present in hard metals. Fig. 38 and Fig. 39 exemplarily show a defect encountered in a tensile specimen with a size of about 20 µm consisting of an agglomeration of WC grains with a grain size larger than the average and with reduced binder content [54].

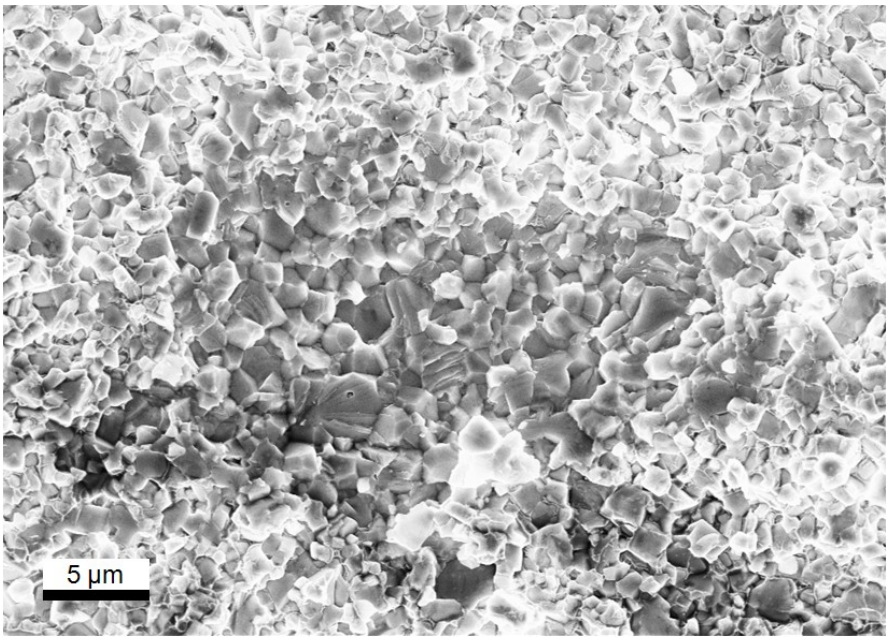

Fig. 38: SEM micrograph of an origin of fracture on a fracture surface of a tensile specimen of geometry S1 made of hard metal grade X1 [54]

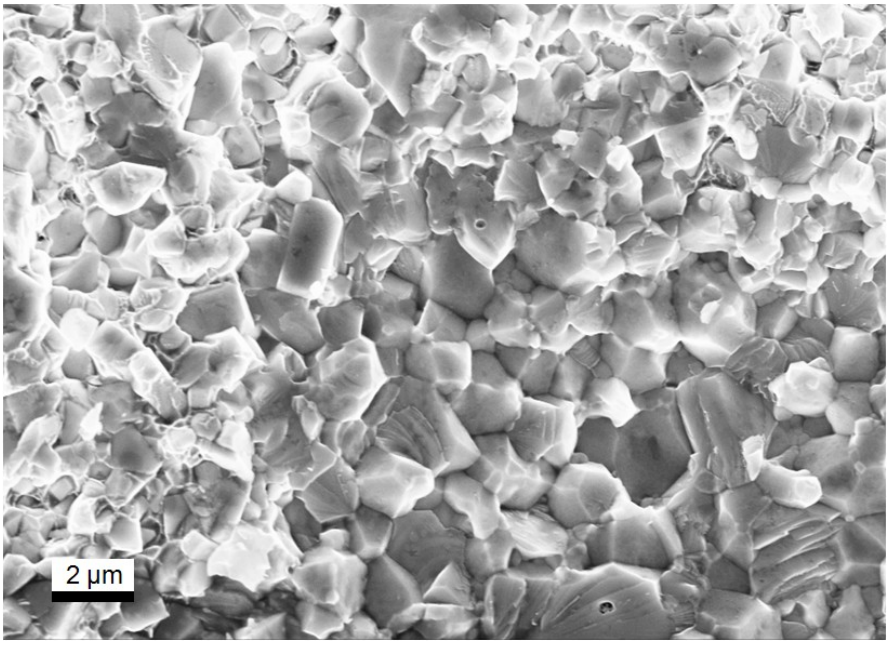

Fig. 39: Detail of the origin of fracture shown in Fig. 38 being an agglomerate of WC grains that are larger than the average WC grain size [54]

6.2.2 Influence of effectively tested volume on tensile fracture strength

For reflection on the influence of V_{eff} on fracture behaviour, test data from specimens of geometries S1 to S4 made of the hard metal grades X9 and X8, with ultrafine WC grain size and 8.2 and 12 wt % of Co content respectively, are considered. Please note that the two materials exhibit the same fracture toughness of 7.5 MPa√m. Samples were produced and tested as described in section 5. The smallest specimen in this comparison is the micrometre sized cantilever specimen. On the one hand its very limited dimensions are large enough to assure the determination of material properties still characteristic for the two phase composite material. On the other hand they facilitate the exploration of the limits of tensile strength when fracture initiating defects become as small as microstructural constituents.

When investigating fracture surfaces of the micrometre sized specimens, no defects such as observed in larger specimen sizes, were encountered. Estimations of critical defect sizes in these smallest specimens based on LEFM, give values in the order of magnitude of the submicron-sized tungsten carbide particles or Co binder

concentrations. It is therefore expected that the high strength values found in these specimens are close to the inherent material strength.

To reproduce materials' properties actually present in components and tools in service, hard metal samples of different geometries, made of the same hard metal grade, compared in this section were produced with the particular processing technology relevant for the respective tool sizes in application. Therefore, samples of different geometry were made from the same hard metal grade but not from the same batch of material. Although it is possible that the materials investigated do have different defect size distributions, this strategy was chosen to match material properties present in industrial applications as closely as possible.

Note that for the specimen geometry S1 and S4 only a limited number of strength experiments were performed. Table 6 shows an overview of the number of tested and compared specimens in the present section [91].

Geometry	Grade	Number of specimens
S1	X9 / X8	3 / 3
S2	X9 / X8	30 / 30
S3	X9 / X8	30 / 30
S4	X9 / X8	2 / 1

Table 6: Overview of the number of tested and compared specimens investigating dependence of tensile fracture strength on V_{eff} [91]

6.2.2.1 Data evaluation

In the experiments considered in this section the maximum forces in all the performed experiments were recorded and fracture stresses were evaluated. For the specimen geometries S1, S2 and S3, they were calculated from standard textbook formulas for the relevant load case assuming purely elastic behaviour [92]. The exact specimen geometry of all the described specimen types was also used to design three dimensional FEM simulation models in ABAQUS [93] to determine stress at fracture quantitatively. The elastic as well as the elastic-plastic stress-strain behaviour, as determined for both

investigated hard metal grades as described above and in [63], was used as input in the FE simulations. Compressive and tensile material behaviour were assumed to be symmetric as a first approximation. The determined stresses at fracture assuming purely elastic material behaviour were compared to results for elastic-plastic stress-strain behaviour. In the case of the micro-cantilever experiments, variations in geometry between individual specimens were taken into account.

As an example, Fig. 40 shows the FE model used for specimen geometry S4 along with the imposed boundary conditions: The lower and the back side of the FE model were fixed in the directions marked by double arrows. One point, being part of the lower and the back side of the model, was fixed in all three spatial directions. The elements used were of a C3D20 type.

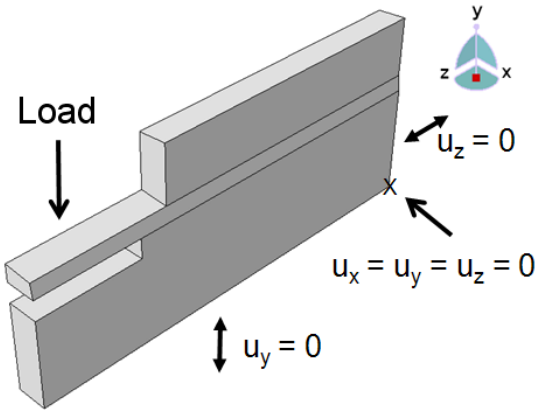

Fig. 40: Geometry and boundary conditions used in the FE simulation (ABAQUS) of specimen geometry S4 [91]

The number of experiments performed for the specimen geometries S1 and S4 is not sufficient to reliably determine the Weibull modulus m [1], therefore the exact value of effectively tested volume cannot be calculated. However, it can be estimated assuming that the Weibull modulus for a material remains constant when the specimen size is varied. Such an estimate is performed by evaluating Eq. 8 for each integration point of a FE simulation model for the respective specimen geometries, namely S1 and S4. The evaluations are performed at the maximum loads observed in the respective experiments. An overview of the utilised evaluation methods for stress at fracture and V_{eff} is given in Table 7.

Geometry	Stress evaluation method	V_{eff} evaluation method
S1	$\sigma = \frac{F}{Area_{\min}}$ [92]	FE simulation evaluating Eq. 8
S2	$\sigma = \frac{32 F l}{d^3 \pi}$ [92]	Analytic solution see Quinn [7]
S3	$\sigma = \frac{32 F l}{d^3 \pi}$ [92]	Analytic solution see Quinn [7]
S4	FE simulation	FE simulation evaluating Eq. 8

Table 7: Overview of evaluation methods for stress at fracture and effectively tested volume V_{eff} for the tested specimen geometries; F is force, l is loaded span, d is specimen diameter [91]

6.2.2.2 Results of strength characterisation

Detailed strength results for specimen geometries S1 and S4 are summarised in Table 8. Please note that for the specimen geometry S4, only one and two valid experiments could be realised for hard metal grade X8 and X9 respectively.

Grade	Geometry	Strength [MPa]
X9	S1	2591, 2373, 2383
X9	S4	6330, 6310
X8	S1	2137, 2301, 3178
X8	S4	5460

Table 8: Specimen geometries S1 and S4 with their respective tensile and bending strength values assuming purely elastic material behaviour [91]

All types of specimens except for specimen geometry S4 fail without measureable plastic deformation. In case of specimen geometry S4, made of hard metal grade X8, some indications of plastic deformation can be found on the surface of the broken specimen. Therefore, FE simulations were performed in order to evaluate the possible effect of plasticity on the fracture strength values. The utilised FE model is shown in

Fig. 41. The location of the stress maximum, marked in Fig. 41 by an arrow, is located very closely to the region were fracture occurred in the tested cantilever (compare Fig. 47).

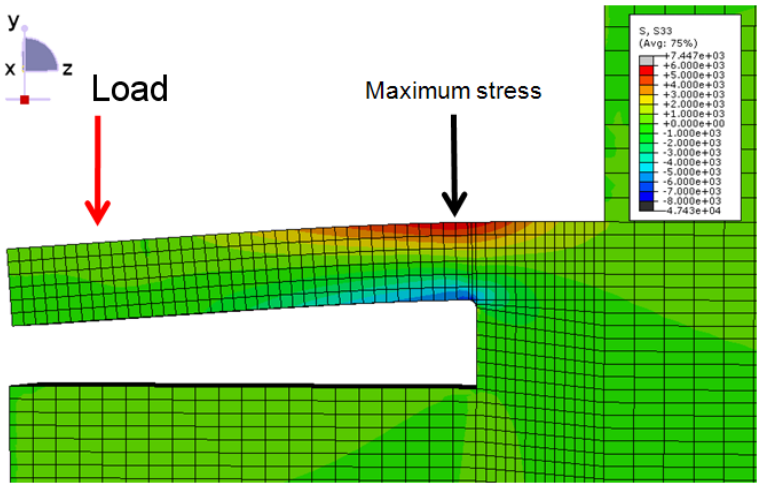

Fig. 41: Finite element model of specimen geometry S4 made of hard metal grade X9: Results in terms of axial stress (in z-direction) at maximum load observed in experiment [91]

Fig. 42 shows simulated stress-strain curves for purely elastic and for elastic-plastic material behaviour for loading up to the experimentally observed fracture load. The results in Fig. 42 clearly indicate that the specimens of geometry S4 fail after some plastification of the specimen has occurred. The fracture stresses are significantly higher than the stresses at the onset of plastic deformation which are in the range of about 3500 MPa for material X9 and about 2000 MPa for material X8. Taking plasticity into account, the fracture stresses for specimen geometry S4 made of X9 and X8 are roughly 6% and 9% lower than the values outlined in Table 8 (compare Fig. 42).

The results further suggest that specimens S1, S2 and S3 made of material grade X9 fail in the elastic regime, while in case of material grade X8 small amount of plastic deformation of these specimens are likely. For the microcantilevers made of X9 and X8 the plastic strains prior to failure roughly reach 0.1% and 0.2% respectively. In the larger specimens made of the hard metal grade X8, plastic deformation occurs as well, but the plastic strains are smaller than 0.05%. No indication for macroscopic plastic deformation is found in the larger specimens made of both materials.

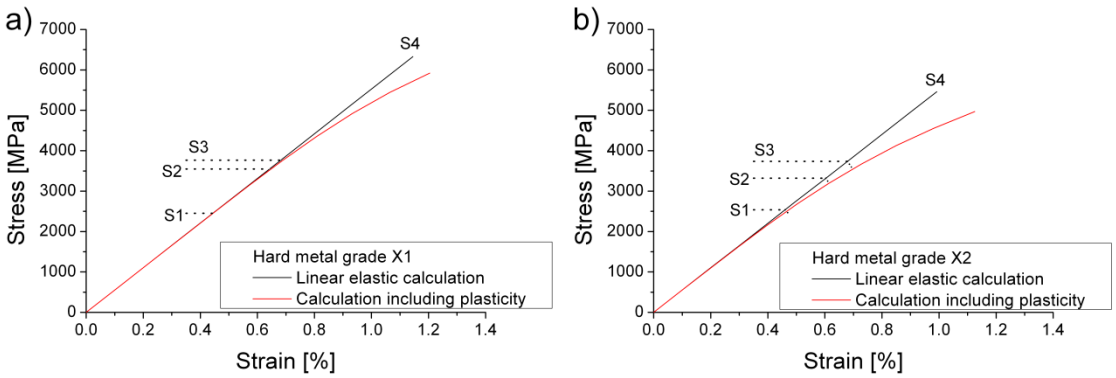

Fig. 42: Resulting stress-strain response at the point of maximum axial stress in FE simulation of specimen geometries S4 made of hard metal grade a) X9 and b) X8. Black and red lines correspond to solutions assuming purely elastic and elastic-plastic material behaviour respectively. Dotted lines indicate levels of stress and strain reached in specimen geometries S1, S2 and S3 respectively [91]

In Fig. 43 strength results for specimen geometries S2 and S3 are displayed in Weibull diagrams. The characteristic strength of the samples of type S3 is significantly higher than that of the samples of geometry S2 for both tested hard metal grades. The obtained ranking is in qualitative agreement with Weibull theory. The obtained Weibull moduli for the sample geometries S2 and S3 made of the same hard metal grade (X9 and X8) cannot be distinguished within the 90 % confidence limits, as pointed out in Table 9.

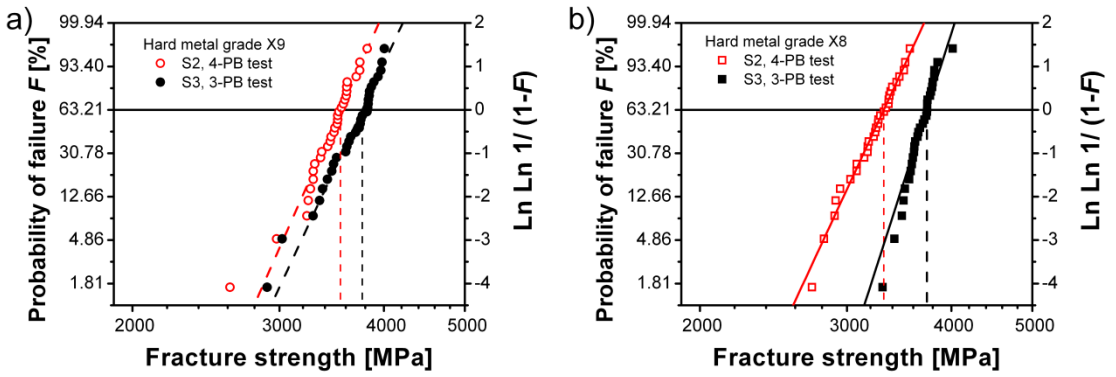

Fig. 43: Fracture strength values in the form of a Weibull diagram for various specimen geometries made of hard metal grades a) X9 and b) X8 as described in the text [91]

The results, summarised in Table 8 and Table 9, clearly indicate that the fracture strength determined in the experiments strongly varies with the effectively tested sample volume. The lowest strength values in the investigated cases are associated with the largest specimen size, the specimen geometry S1. The highest strength values are determined for the smallest specimens of geometry S4.

Grade	Geometry	Weibull modulus m [90% confidence interval]	Characteristic strength σ_0 [MPa] [90% confidence interval]	V_{eff} [mm^3]
X9	S2	18.9 [14.8, 24.1]	3549 [3490, 3611]	1.071
X9	S3	17.9 [14.1, 22.9]	3768 [3702, 3837]	0.001
X8	S2	18.0 [14.1, 23.0]	3320 [3262, 3380]	1.148
X8	S3	26.1 [20.5, 33.3]	3738 [3693, 3785]	0.001

Table 9: Weibull moduli, characteristic strength values and effectively tested sample volumes derived from the Weibull plots in Fig. 43, 30 specimens tested for each grade [91]

In order to demonstrate the size effect, fracture strength values determined for specimens S1 to S4 are displayed in Fig. 44 as a function of the effective volume. Fig. 44 also contains an estimate of the effect of the effective volume on the characteristic strength based on Weibull theory for specimen S2. The strength estimation for different effective volumes was performed evaluating Eq. 9. In the case of specimen geometries S1 and S4, Eq. 8 was evaluated via FE simulations to obtain information about their effectively tested volumes. Results are displayed in Fig. 44 along with results of the analytic relations for V_{eff} applicable for the more simple geometries S2 and S3, being cylindrical rods [7]. Please note that the strength values determined for specimen geometries S1 and S4 are statistically not reliable because of the low number of valid test data. Additional caution is necessary when interpreting these data points since the Weibull modulus m, necessary for calculating V_{eff}, was assumed to be constant when varying specimen size.

Eq. 9 is only applicable for "Weibullian" materials [4]. Using the strength data of sample S2, the extrapolation predicts a significantly higher strength for sample S3 than the one observed in the experiments for both investigated hard metal grades (see Fig. 44). Obviously the two samples do not behave in a Weibullian way. Possible reasons for this result are differences in the nature of defects or defect size distributions in the two sample batches or different qualities of the surface finish of the samples, including surface eigenstresses from the surface finishing process (note that there is a large difference in the surface/ volume ratio between the specimens S2 and S3), see [16],[17].

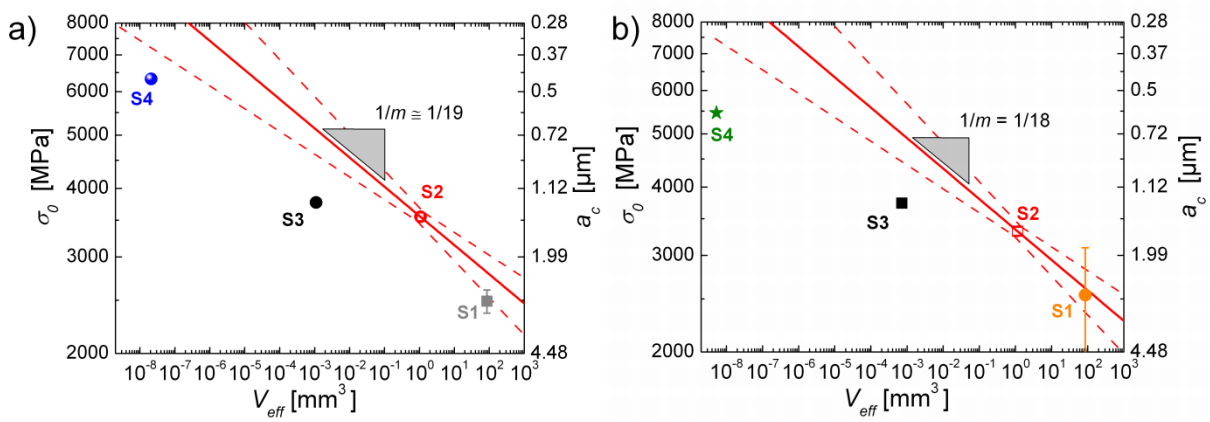

Fig. 44: Quantitative comparison of the strength values along with equivalent critical defect radii of specimen geometries S1, S2, S3 and S4 by strength extrapolation according to Weibull theory for hard metal grades a) X9 and b) X8. Dashed lines correspond to 90% confidence intervals. Strength values are linked to critical defect radii by Eq. 1a [91]. Note that the compared grades exhibit the same fracture toughness value

6.2.2.3 Defect sizes

Fracture mechanical estimation of defect sizes

An estimate of the critical defect size a_c [11] that leads to failure in the investigated specimens was performed using LEFM for the sake of simplicity. The fracture toughness and the equivalent fracture stress σ, e.g. the maximum stress as calculated in the FE simulation assuming linear elastic material behaviour, were inserted into Eq. 1a. For simplicity, Y was taken to be 1. This approach can be justified by considering that Y varies from 0.63 for a penny shaped volume crack [10] and 1.12 for a shallow surface crack [11] and also because the exact values of Y for real defect shapes are not known.

Results of the estimates for a_c at a stress of σ_0 are indicated on the right-hand side ordinates of Fig. 44 a) and b). They range from about 3 µm for the specimen geometry S1 to about 1 µm for specimen geometries S2 and S3. For the micro-cantilevers made from the material X9, a_c at a stress of σ_0 can be estimated to be about 500 nm which is in the size range of the WC grains or Co concentrations. The result for a_c of about 600 nm in the case of the micro-cantilever made of the hard metal grade X8, is also very similar to the size of the microstructural features in this sample. These results indicate that fracture might have started from a single WC grain or grain boundary. One can thus assume that the bending strength determined in the experiments with µm sized bending

specimens is close to the value one would obtain in an ultrafine grained hard metal free from microdefects. In other words, the determined strength can be considered as the intrinsic strength of the material.

Note that in the case of specimen geometry S4 the application of the LEFM approach is questionable since a small amount of plastic deformation of the beams is expected. The estimated defect size can thus be considered as an upper limit for the critical defect size.

In addition it should be noted that when tested specimens become very small, as in the case of specimen geometry S4, one approaches the limits of predictive power of the Weibull theory [13]. One of its prerequisites is that flaws do not interact, which is not the case when critical defect size approaches that of neighbouring WC grains [18]. In this case, defect density and strength values could be lower than predicted by Weibull theory [13].

Fractographically determined defect sizes

From Fig. 45 to Fig. 52 SEM images are shown as examples of fracture surfaces observed in tested specimens of different geometry. In Fig. 45 a typical fracture origin in a specimen of geometry S2 made of hard metal grade X9 is displayed. It represents an aggregate of WC grains that are larger than the average grain size, with a pore of a few micrometres in size in its centre. The smaller effectively tested volume in the sample geometry S3 leads by trend to smaller defects identified as origins of fracture. An example for a defect found on a fracture surface of sample geometry S3 in form of a micrometre sized pore is displayed in Fig. 46. Along with these pores, micrometre sized inclusions acted as origins of fracture. Similar defects were found in specimen of geometry S2 and S3 made of hard metal grade X8.

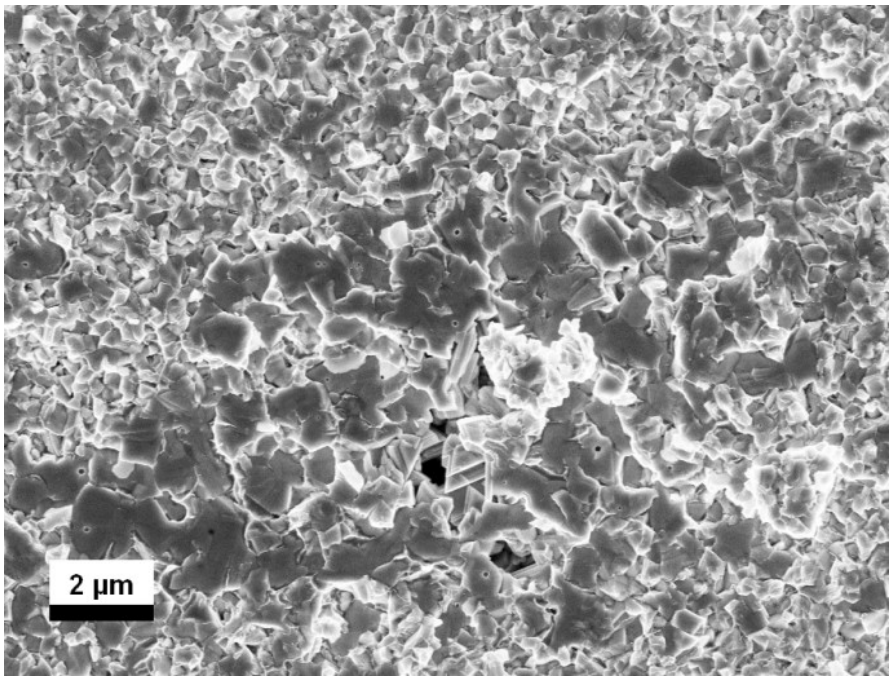

Fig. 45: SEM micrograph of an origin of fracture in a sample of geometry S2 (hard metal grade X9) [91]

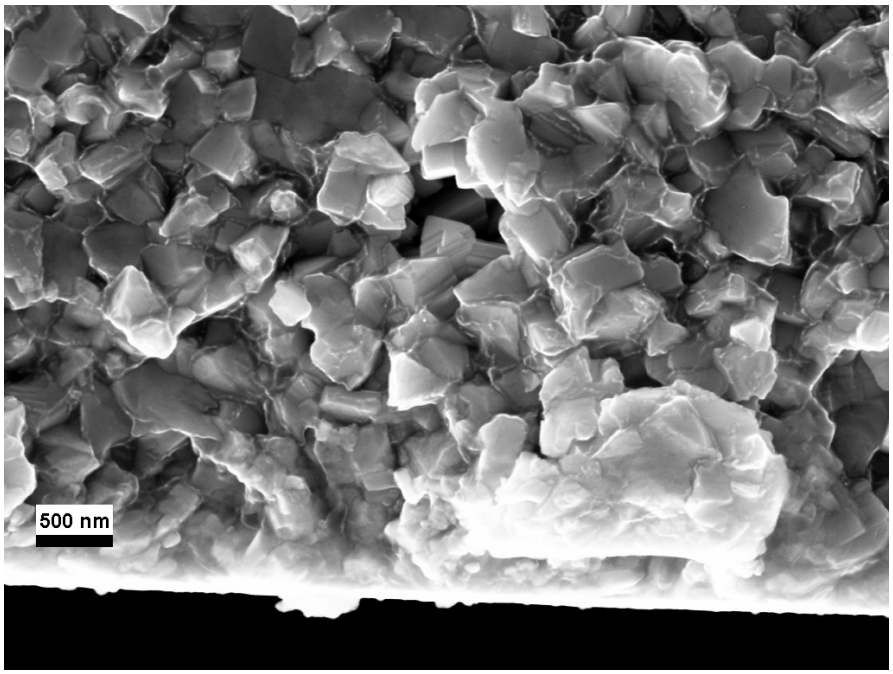

Fig. 46: SEM micrograph of a micro-pore being an origin of fracture in a sample of geometry S3 (hard metal grade X9) [91]

The experimentally observed defect sizes are in good agreement with the fracture mechanical estimations. If a defect's size predicted by LEFM differs from the size

actually encountered on a hard metal fracture surface, as it was occasionally the case for defects smaller than a few micrometres, this may be due to several reasons:

a. In bending experiments, defect sizes predicted by LEFM are valid for defects located at the specimen surface. The actually present defect size may be underestimated if the defect is located under and far from the specimen surface because of the stress gradient in the bending specimen.
b. Another particularity concerning bending experiments is the existence of a critical location of defects for which the transverse rupture strength is minimised. This critical location of a (e.g. spherical) defect is not located on the specimen's surface but closely below it (see e.g. Fig. 46) due to the stress concentration that arises between the defect and the specimen surface [94]. The defect first grows towards the maximum stress located at the surface increasing its effective size [94].
c. The use of the factor *Y* for the prediction of defect size approximating a defect's geometry as an ideal geometric shape is a general limitation of predictive accuracy since real defects exhibit more complex geometries leading to a stress concentration situation differing from the ideal situation.
d. In the case of micrometre sized defects, the actually present defect size may be overestimated by LEFM predictions due to the so-called R-curve behaviour of WC-Co hard metal [95]-[97]. In long cracks, Co binder ligaments convey some force between crack flanks at some distance behind the crack tip and contribute to the apparent fracture toughness of the material. If the defect from which a crack emanates is very small, the fracture toughness value may be smaller than that of a longer crack because these Co ligaments still have to develop.

A fracture surface of a specimen of geometry S4, made of hard metal grade X9, is displayed in Fig. 47 in a side view and under an inclination of 45° in Fig. 48, as indicated in Fig. 47. Details of the upper left hand side and upper right hand side of Fig. 48 are displayed in Fig. 49 and Fig. 50 respectively. No distinct defects such as they were found on fracture surfaces of the larger specimen geometries are to be identified.

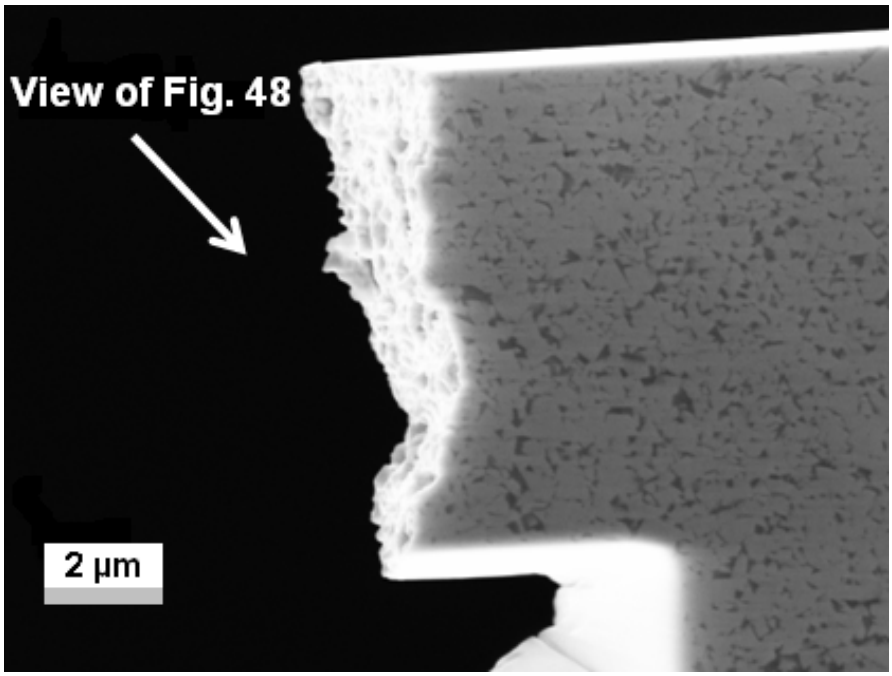

Fig. 47: Side view of fractured sample of geometry S4 made of hard metal grade X9 [91]

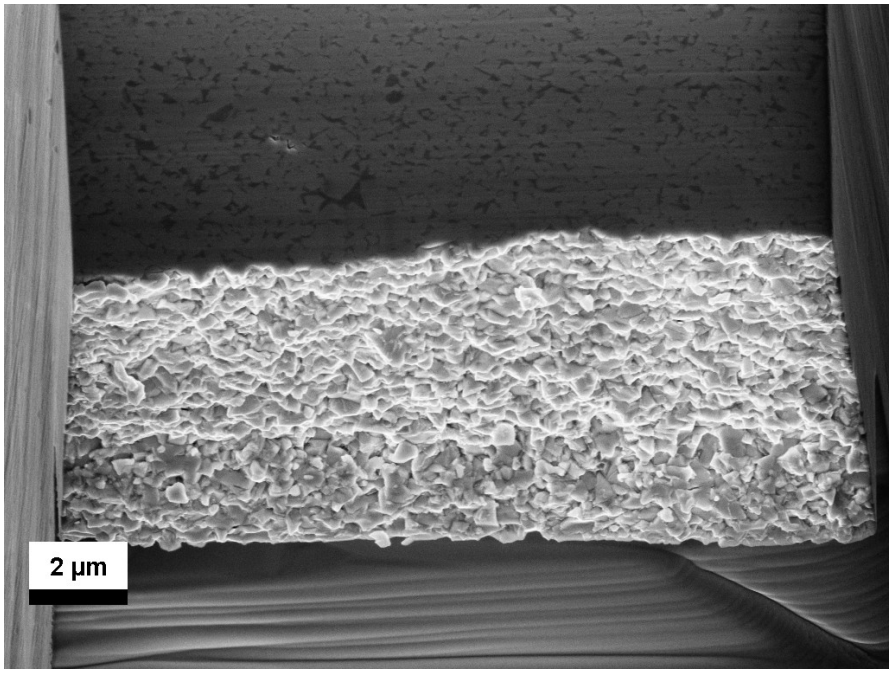

Fig. 48: SEM micrograph of a fracture surface of sample geometry S4, hard metal grade X9, inclined by 45° as indicated in Fig. 47 [91]

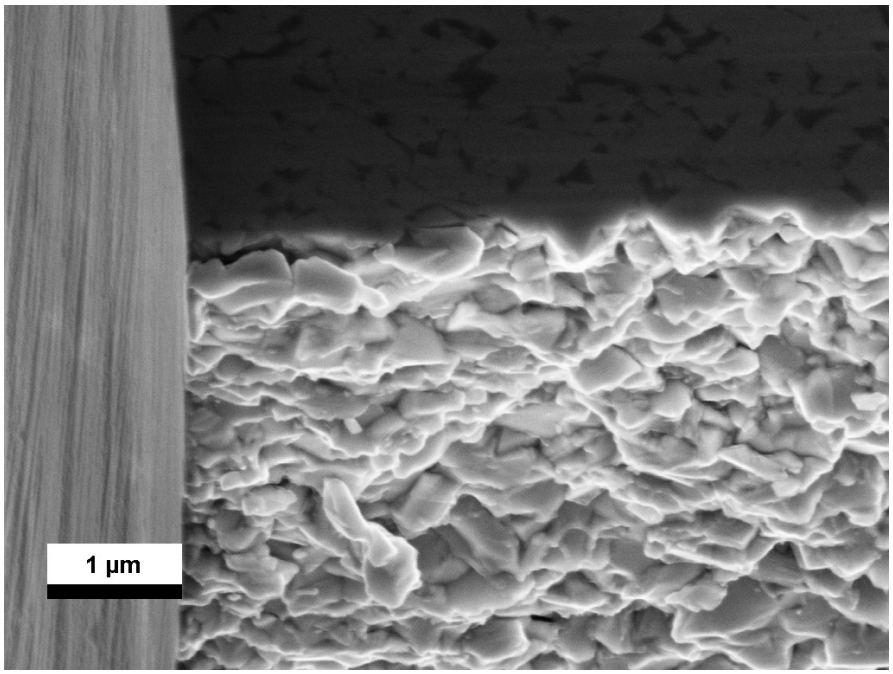

Fig. 49: Detail of the upper left side of fracture surface shown in Fig. 48 [91]

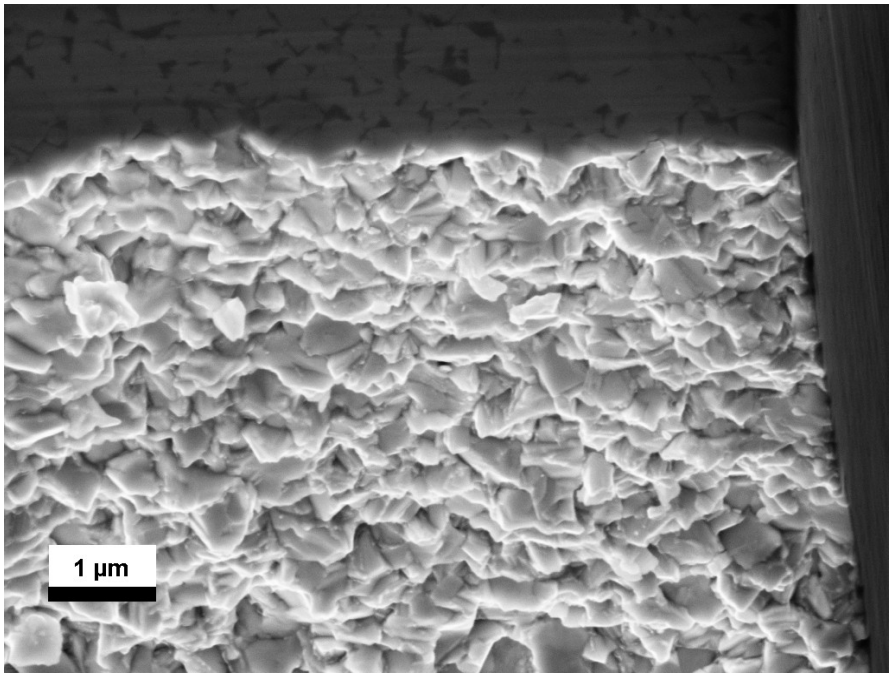

Fig. 50: Detail of the upper right side of fracture surface shown in Fig. 48 [91]

Fig. 51 shows a view of a fracture origin of a specimen of geometry S4 made of hard metal grade X8. The view is inclined under 45°, similar to that of Fig. 48. As indicated in Fig. 52 by a circle, the fracture surface exhibits a location at which a single WC

crystallite seems to be present, possibly not wetted during liquid phase sintering of the material, or where due to microplastic deformation (i.e. dislocation pile up) a decohesion might have occurred. Such an inhomogeneity acts as a stress concentrator in the material's microstructure, becoming the origin of fracture. Please note that the size of the identified inhomogeneity is in the order of magnitude estimated for the observed value of stress at fracture in this specimen.

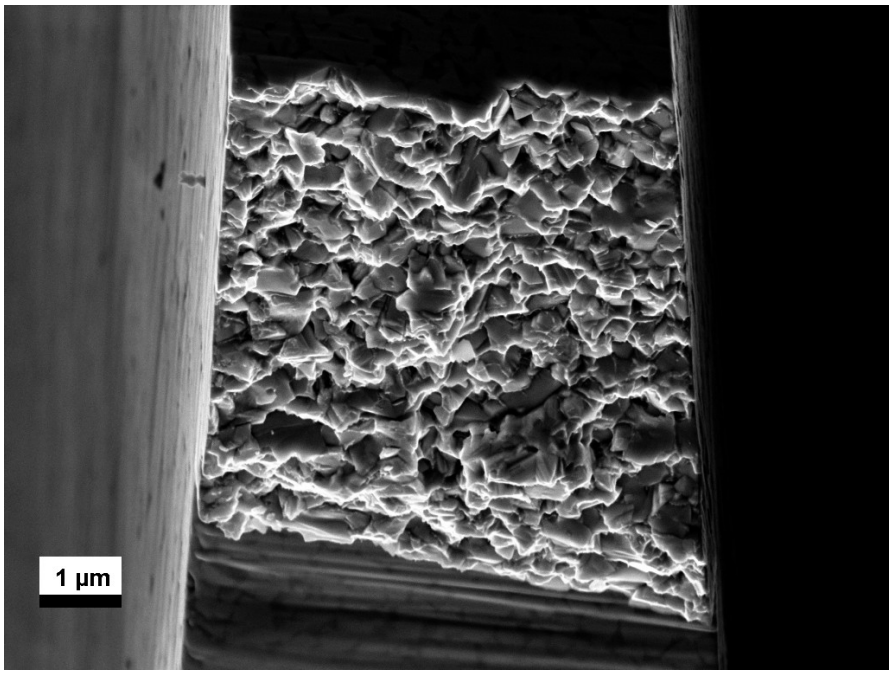

Fig. 51: Fracture surface of sample geometry S4 made of hard metal grade X8, view inclined by 45° [91]

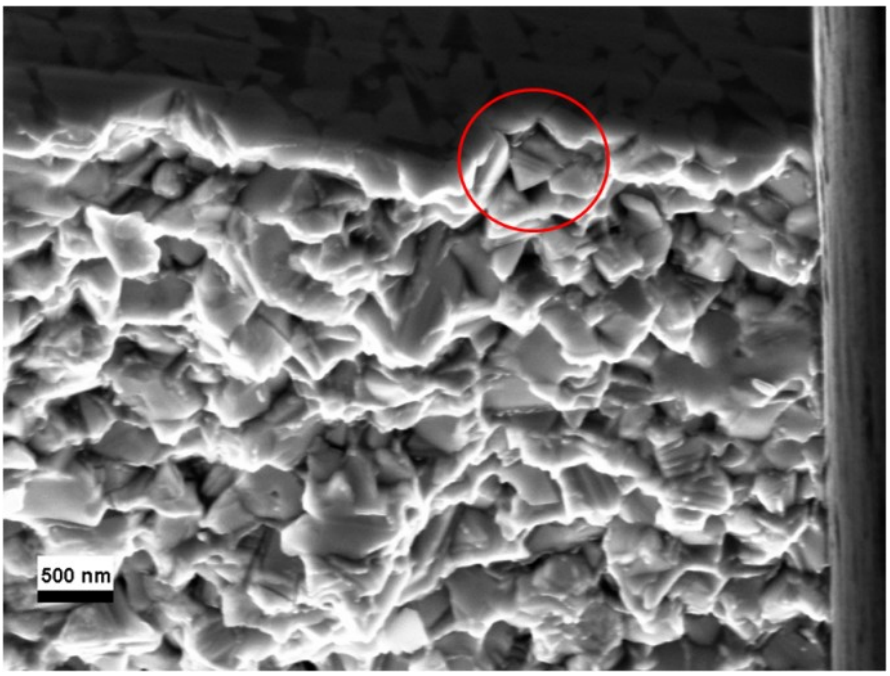

Fig. 52: Detail of the upper right side of fracture surface shown in Fig. 51 [91]

6.2.2.4 Defect densities

In brittle materials the typical sizes of defects that become origins of fracture can be predicted from the strength results via LEFM according to Eq. 1a. In addition to the size of the defects, their frequency can also be determined from the strength results evaluating Eq. 5 (see section 3.2). The typical density of defects of a certain size in a specimen of a certain V_{eff} for specimen geometries S2 and S3 made of hard metal grades X9 and X8 is described in Fig. 53. Considering the pronounced differences in the density of defects of the same size in the specimens of geometry S2 and S3, probing a V_{eff} differing 3 orders of magnitude, it becomes apparent that the defect size distribution in the hard metal is in fact not Weibullian. The defect densities calculated from the strength data of the specimens S3 geometry are about 3 orders of magnitude higher than the one calculated from the strength data acquired testing the specimens with geometry S2. If the defect densities would assume values as in a Weibull material, the points of in Fig. 53 a) and Fig. 53 b) would lie on a straight line [4].

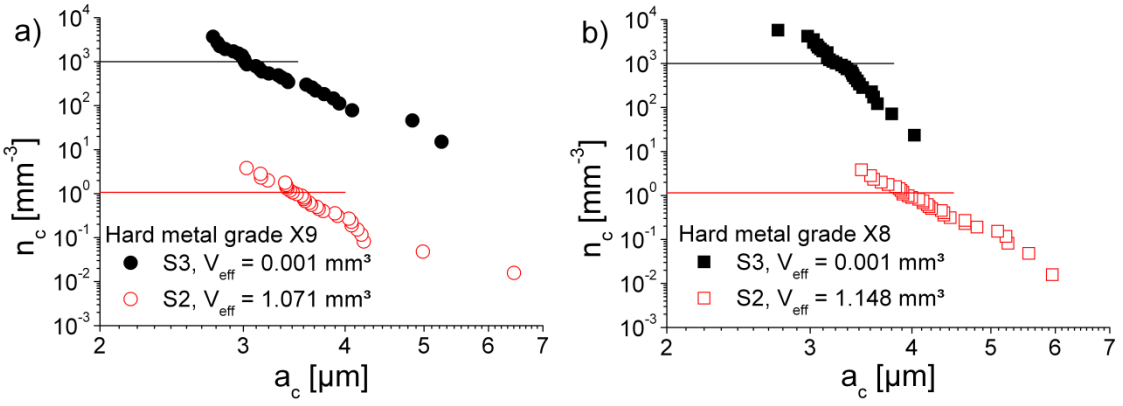

Fig. 53: Defect densities as a function of defect size for specimen geometries S2 and S3 made of hard metal grades a) X9 and b) X8. Defect density at characteristic strength ($N_{c,S}$ = 1) marked by horizontal lines

From the defect densities one can calculate the number of critical defects per specimen (per V_{eff}) evaluating Eq. 4 which gives a feel for the probability to find a certain defect size in a tested specimen (see Fig. 54). The largest defects of about 4 µm to 6 µm in size are about 250 times less frequent than the smallest ones of about 3 µm in size. The smallest critical defects, that are critical at the highest stress values in the batch of 30 compared specimens, are found about 4 times within V_{eff}, whereas the largest critical defects are found in every 168th specimen only. Note that in strength experiments the defect that exhibits the maximum value of K becomes the origin of fracture. Therefore it can be easily found by means of fractography, in contrast to metallographic methods in which defects only show when they are cut by a random section of a three-dimensional microstructure.

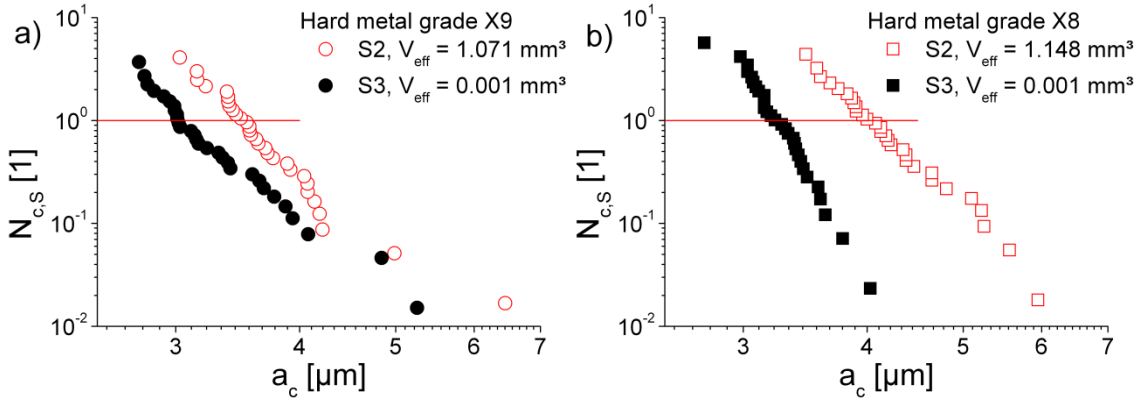

Fig. 54: Number of critical defects $N_{c,S}$ as a function of defect size for specimen of geometries S2 and S3 made of hard metal grade a) X9 and b) X8; characteristic strength ($N_{c,S}$ = 1) marked by horizontal lines

To determine how many sections of defects present in a microstructure can be found in an individual metallographic specimen, it is necessary to extrapolate the number of defects of a certain size per unit volume to defect sizes smaller than the measured critical defect size range. When doing so, e.g. for material grade X8 and geometry S2 (see Fig. 55), it becomes apparent that the extrapolation yields unrealistically large defect densities for small defect sizes with e.g. one defect of 0.9 µm in diameter per µm³ as indicated in Fig. 55 by a horizontal line. This limitation of Weibull theory when considering very high defect density [13] greatly influences the following prediction of number of sections of defects per unit area [98]:

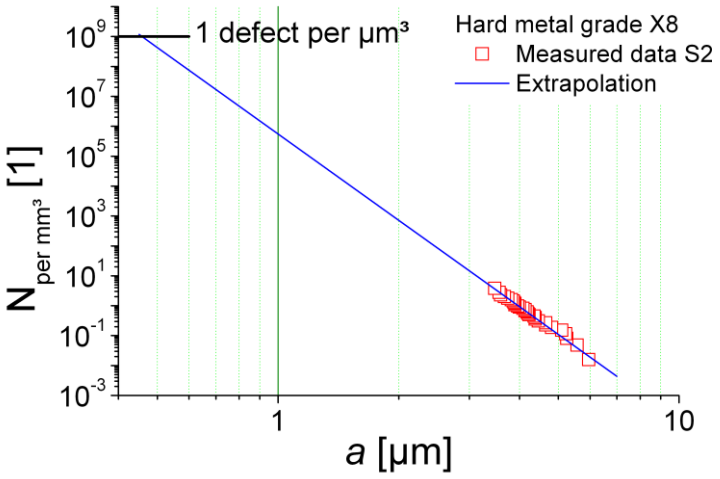

Fig. 55: Extrapolation of number of defects per mm³ of a certain defect radius *a* to small defect dimensions from data measured for specimens of geometry S2 made of hard metal grade X8

In the present example, sections of defects from the upper end of the defect size range are very unlikely to be found in metallographic specimens because, compared to smaller defects, they occur infrequently within the sample volume. In addition, a plane may cut a defect not only intersecting its centre but also at a certain distance from the centre. The resulting section of a cut defect can therefore be smaller in dimension than the maximum dimension of the defect. Table 10 shows the results of the mentioned prediction of number of sections of defects for various size intervals per unit area. It is clearly evident that in a metallographic specimen larger defects are by far less frequently intersected (and therefore visible) than smaller ones, simply because of their relative sparsity.

Size interval [µm]	Defects per mm³	Number of sections per mm²	Number of sections per 100 µm x 100 µm
0.5 ÷ 0	554300*	277248*	2772*
1 ÷ 0.5	719*	627*	6*
1.5 ÷ 1	15	17	0.169
2 ÷ 1.5	0.933	1.298	0.013
2.5 ÷ 2	0.110	0.178	0.002
3 ÷ 2.5	0.019	0.035	3.5E-04
3.5 ÷ 3	0.004	0.009	9.0E-05
4 ÷ 3.5	0.001	0.003	2.8E-05
4.5 ÷ 4	3.9E-04	0.001	9.7E-06
5 ÷ 4.5	1.4E-04	3.8E-04	3.8E-06
5.5 ÷ 5	5.7E-05	1.5E-04	1.5E-06
6 ÷ 5.5	2.5E-05	5.9E-05	5.9E-07

Table 10: Estimates of number of defects per unit volume and number of sections per unit area for certain size intervals evaluated for hard metal grade X8, specimen geometry S2 from an extrapolation according to Weibull theory and [98]. Values marked by an * are most likely to high as described in the text

Since conventional surface preparation techniques such as polishing and etching obscure or destroy fine surface features, a more gentle method in the form of a Gatan precision ion polishing system (PIPS) was applied to experimentally check the predictions of Weibull theory of defect density in WC-Co hard metal. In contrast to FIB polishing, during which Ga^+ ions impinge only very locally to remove material, PIPS is able to polish areas in the order of a mm² by Ar^+ ions that impinge under grazing incidence of about 2°.

In SEM micrographs of a hard metal surface prepared by PIPS (material X8, specimen geometry S2), various sections of micro-pores as encountered on fracture surfaces of the material can be distinguished (see Fig. 56 to Fig. 58). These pores are oftentimes located very close to one another so that their stress fields may interact upon loading, which contradicts a basic assumption of Weibull theory [13]. Therefore it can be expected that Weibull theory does not correctly describe the densities of these very small defects.

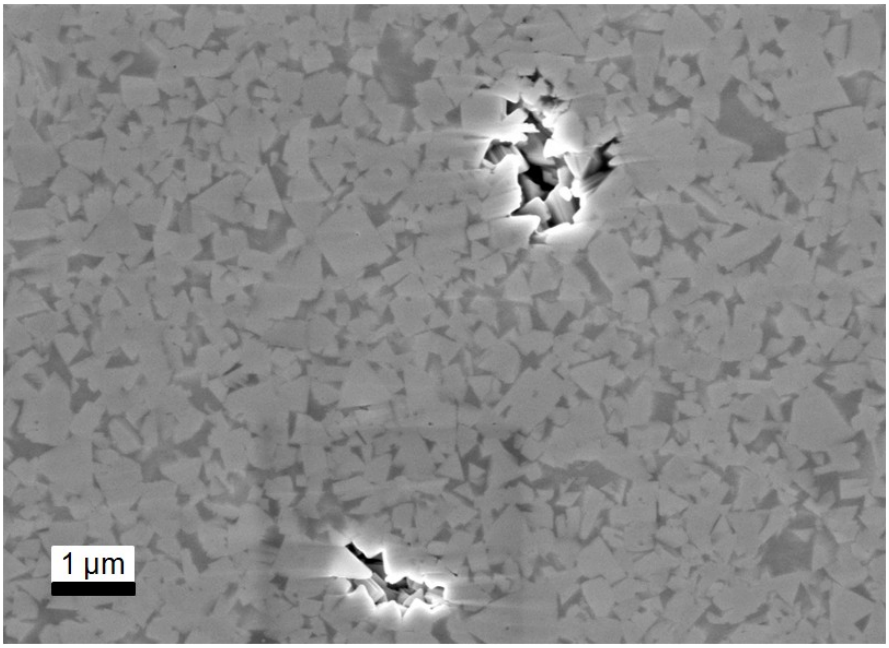

Fig. 56: Detail of Fig. 57: Microporosity in microsection of hard metal grade X8, specimen geometry S2

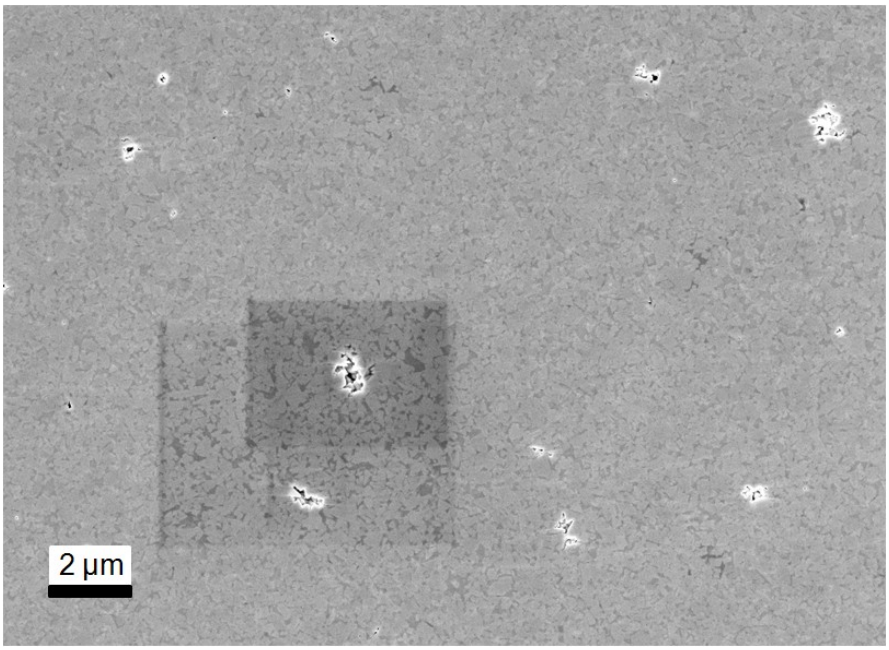

Fig. 57: Detail of Fig. 58: Microsection of hard metal grade X8, specimen geometry S2 prepared by PIPS polishing showing microporosity

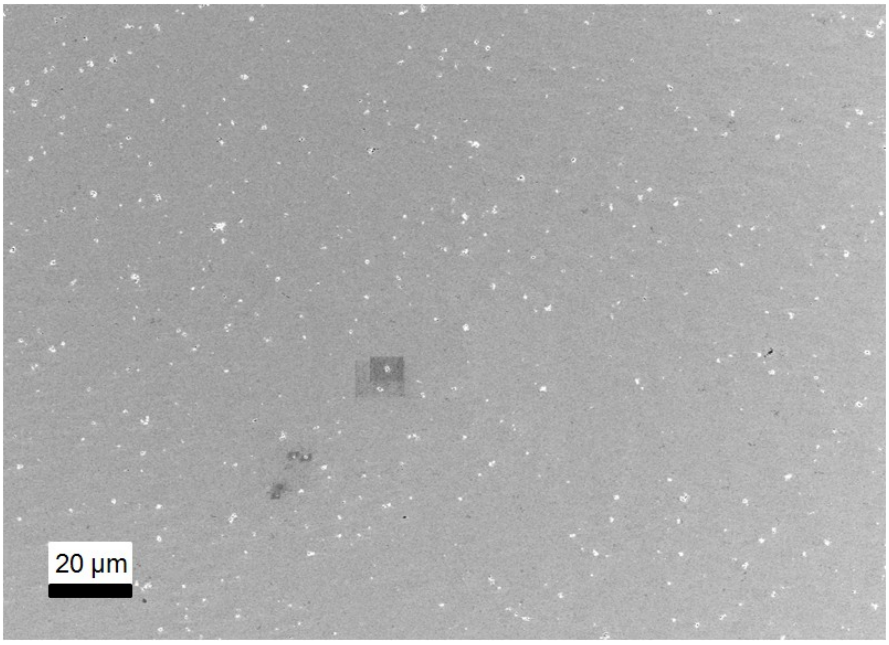

Fig. 58: Overview of microporosity in microsection of hard metal grade X8, specimen geometry S2

Comparing the number of defect sections counted on the area of Fig. 58 and the predicted number for this area including extrapolation errors, one can find that the predicted number is about 13 to 25 times larger than the one actually encountered on the metallographic specimen. This discrepancy is most likely caused by the limitation of predictive power of the used extrapolation when considering very small defects of great density as pointed out earlier and in [13].

To make sure that the PIPS procedure does not induce image artefacts, serial sectioning of regions of the material containing micro-pores with the FIB tool was performed, revealing that the detected defects are in fact micrometre sized pores: Just like in the images attained from PIPSed surfaces, also in the images from FIBed surfaces the presence of freestanding, facetted WC crystallites was detected which is a clear indication for an internal void or pore (see Fig. 59). The attained images viewed in consecutive order also showed the 3-dimensional shape of the pore.

Fig. 59: Microsection of specimen geometry S2, made of hard metal grade X8 prepared by FIB polishing, showing microporosity

7 Material properties under cyclic loading conditions

Apart from the need to understand the stress-strain response under monotonous loading conditions, engineering application also requires an understanding of the cyclic stress-strain and cyclic fracture behaviour of the material. Compared to the rather ample research performed on the fracture behaviour of WC-Co hard metals under cyclic bending loading conditions [50],[75],[99],[102]-[107], the information available on cyclic stress-strain behaviour under uniaxial loading conditions is scarce in literature. A single comparison of static and cyclic stress-strain curves indicates cyclic softening of the material when exposed to fatigue loading [51].

The fatigue crack initiation from material inhomogeneities and the subsequent fatigue crack growth (FCG) of the cracks, until the maximum stress intensity K_{max} at the tip of the growing crack approaches the fracture toughness K_{IC}, determines the length of the fatigue life of components and tools, also in the case of WC-Co materials [99]. High crack growth exponents, the therefore very swiftly accelerating cracks [51],[99],[100] and the rather low fracture toughness of hard metals, lead to rather low slopes in S-N curves, especially at high stress ratios with mean stress in tension.

In contrast to static loading, under which cracks propagate through both the carbides and the ductile binder phase, forming a multi-ligament zone of stretched Co binder between fractured WC grains [101], cracks propagates mainly in the ductile binder phase under cyclic loading conditions [75],[102]. There are indications that the mechanically induced phase transformation of the Co binder from fcc to hcp in the binder ligaments plays a role also under cyclic loading conditions: According to [103] the localisation of fatigue damage in shear bands and areas of transformed and therefore embrittled binder phase are reasons why fatigue sensitivity is not a simple function of binder content in hard metals with an average WC grain size of 1 µm. Other authors state that the fatigue sensitivity, defined as the ratio between applied stress intensity factors corresponding to FCG threshold and fracture toughness, increases if the stress ratio R ($R = \sigma_{min}/\sigma_{max}$) is decreased from 0.7 to 0.1 and that the effective ductility of the

constrained Co binder rises [100]. The hard metals become more fatigue sensitive as λ_{Co} increases from 0.15 µm to 0.75 µm and a transition from ceramic-like to metal-like fatigue crack growth behaviour is observed, i.e. the prevalence of K_{max} over ΔK as the fatigue controlling parameter becomes less pronounced. Other investigations on ultrafine grained hard metals support the findings of [100] with regard to fatigue sensitivity [104]. Fatigue limit rises with a decrease in λ_{Co} at room temperature [104] and also at elevated testing temperatures [105]. Significantly higher fatigue life is found in hard metals at 300°C testing temperature compared to room temperature tests [106]. Varying testing temperatures up to 700°C, lifetimes significantly below the values determined at room temperature are encountered [107]. The cyclic material behaviour of hard metals cannot be deduced from their behaviour under static loading conditions [107].

In the current section, information on the characteristic cyclic flow and ratchetting behaviour of WC-Co hard metals under uniaxial cyclic loading, depending on microstructure is presented. In addition, the influence of overloads, surface finish and residual stresses on the cyclic fracture behaviour of specimens subject to uniaxial and bending loading under various stress ratios is discussed. The pronounced impact of defect size on e.g. S-N behaviour is documented.

7.1 Flow behaviour under cyclic loading conditions

7.1.1 Cyclic stress-strain curves under uniaxial loading conditions

To show the characteristic stress-strain response of a WC-Co hard metal under repeated loading and unloading, the hard metal grade X1 was chosen as an example. The imposed stress ratio R was minus infinity, the applied testing frequency was 0.25 Hz in all the experiments described in section 7.1.

In the first loading cycle, the material shows considerable plastic deformation upon compression loading as described in section 6. In the unloading half-cycle, back-deformation sets in very early at rather high stress levels, reducing the amount of remaining plastic strain at zero stress, as indicated by parallel lines as guides for the

eyes in Fig. 60, that shows the first load cycle of the cyclic stress-strain diagram. For metal matrix composites this so-called Bauschinger effect [108] was predicted by FEM simulations due to constraint of plastic flow [109], the strain hardening behaviour of the binder and internal residual stresses [110]. The Bauschinger effect was also experimentally demonstrated in passivated thin films [111], in which dislocation motion is dimensionally constrained. In addition, the Bauschinger effect was also observed in unpassivated thin films in which inhomogeneous deformation due to differences in grain size and grain orientation was proposed to cause the effect [112].

The back-deformation in the unloading half-cycle is possibly also caused by the tendency of dislocations to minimise their line energy, retreating from narrow binder channels into which they were forced during plastic deformation during the loading half-cycle.

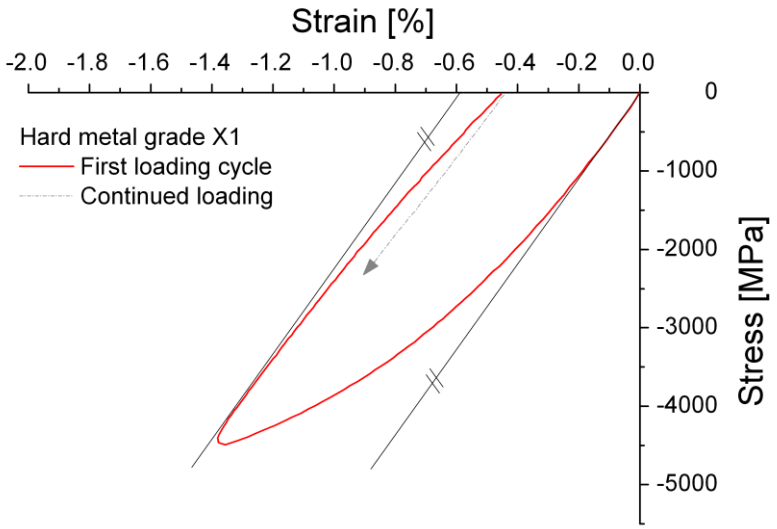

Fig. 60: Cyclic stress-strain diagram of hard metal grade X1 - first load cycle, stress ratio $R = -\infty$. Parallel lines as guides for the eyes indicating Bauschinger effect

Fig. 61 shows the second load cycle of the cyclic stress-strain diagram, which exhibits a drastically decreased hysteresis loop width, i.e. the amount of plastic deformation is by far smaller compared to the first load cycle.

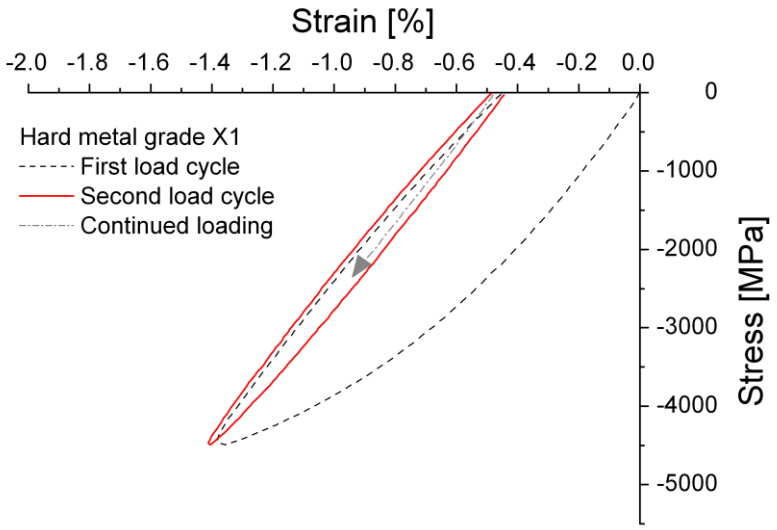

Fig. 61: Cyclic stress-strain diagram of hard metal grade X1 - second load cycle, stress ratio $R = -\infty$

This trend is continued when looking at the tenth load cycle and its very narrow hysteresis loop depicted in Fig. 62. The hysteresis loop widths in the 100th and the 5000th load cycle are even narrower than in earlier load cycles, but greater than zero as depicted in Fig. 63 and Fig. 64 respectively.

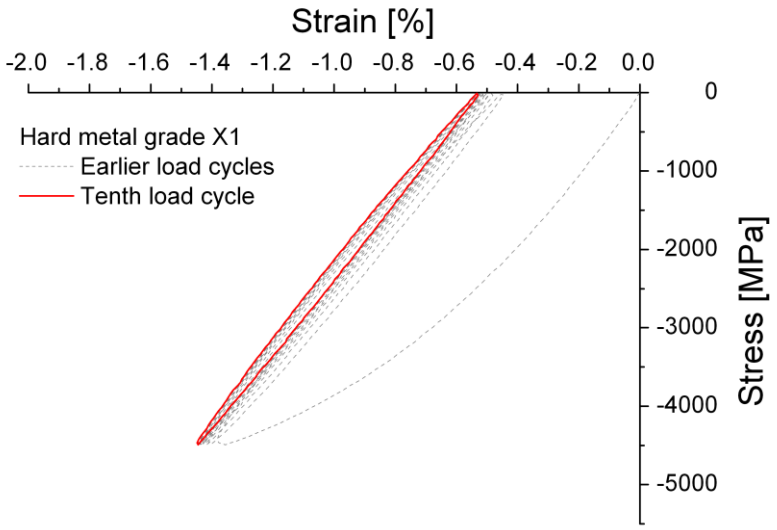

Fig. 62: Cyclic stress-strain diagram of hard metal grade X1 - tenth load cycle, stress ratio $R = -\infty$

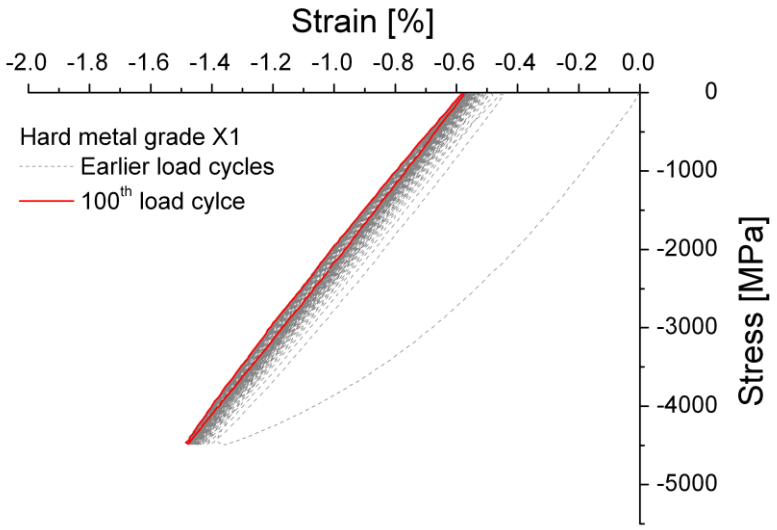

Fig. 63: Cyclic stress-strain diagram of hard metal grade X1 - 100th load cycle, stress ratio R = -∞

The increase in strain present at zero applied stress, referred to as residual strain, progresses rapidly within the first few load cycles and slows down in the consecutive load cycles. The residual strain finally stabilizes at a certain level as indicated in Fig. 64 by an arrow, depending on load history and material grade.

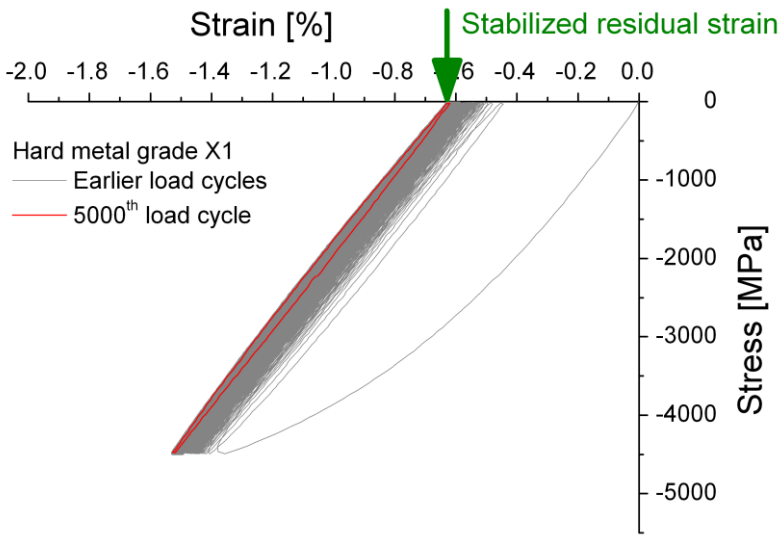

Fig. 64: Cyclic stress-strain diagram of hard metal grade X1, stress ratio R = -∞, 5000th load cycle, stabilized residual strain at zero applied stress indicated

7.1.2 Ratchetting behaviour under uniaxial loading conditions

Ratchetting or cyclic creep is a phenomenon of accumulation of plastic deformation under cyclic stressing with non-zero mean stress that results when yield in the individual load cycles occurs [113].

To study the development of the residual strain present at zero applied stress with the number of load cycles under a stress ratio of minus infinity, the hard metal grades X2 (which is very similar to the grade X1 in composition and microstructure), X5, X8 and X9 were chosen. Three of the compared grades contain 12 wt % binder and vary in their WC grain size from fine, via submicron to ultrafine. To explore the effect of lowering the binder content at a certain WC grain size, the ultrafine grained grade X9 with 8.2 wt % binder was added. An overview of the investigated hard metal grades is given in Fig. 65.

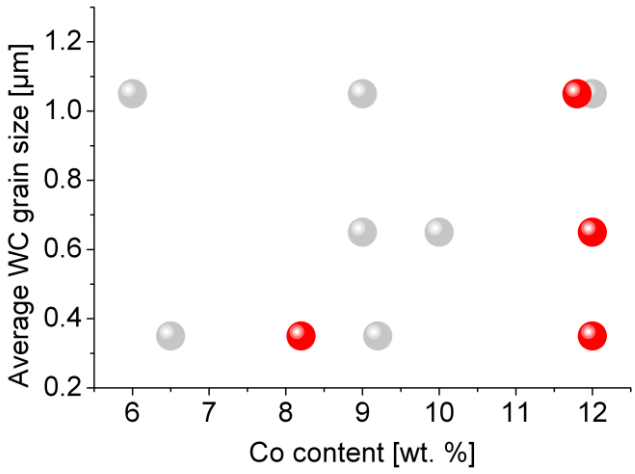

Fig. 65: Overview of hard metal grades investigated in terms of ratchetting behaviour as characterised by average WC grain size and Co content

In stress controlled uniaxial tests, five specimens of each of the four investigated grades were subjected to five different stress ranges $\Delta\sigma$ that approximate the yield strength values $R_{p0.05}$, $R_{p0.1}$, $R_{p0.2}$, $R_{p0.3}$ and $R_{p0.5}$. The development of the residual strain present at zero applied load as a function of the number of cycles is characterised by a rapid increase of residual strain in the early load cycles. In most cases, the residual strain stabilizes at a certain level after a few hundred load cycles as shown in Fig. 66 to Fig. 69. The experiments were performed up to 2000 cycles for cases in which the material

response had stabilized, in other cases the tests were performed up to higher cycle numbers. The results in Fig. 66 to Fig. 69 indicate that in most cases, ratchetting is completed within a few hundred load cycles. In this respect, the cyclic material response is very similar to the one of WC-Ni composite materials [114].

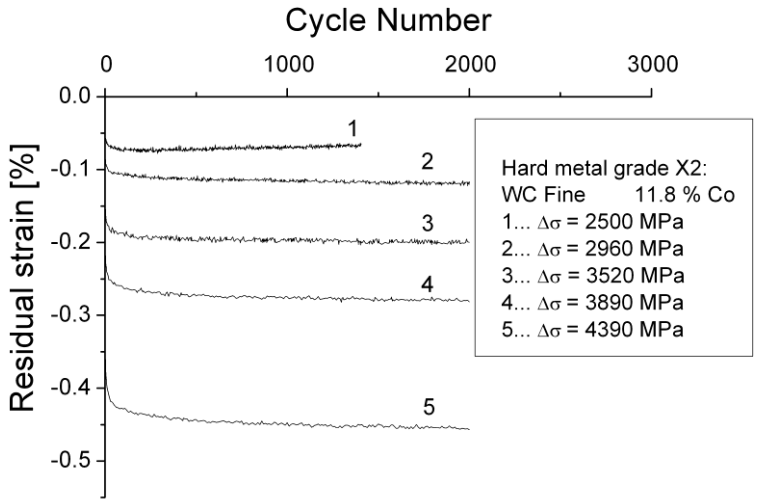

Fig. 66: Development of residual strain at zero applied stress with number of cycles at $R = -\infty$ for hard metal grade X2 [63]

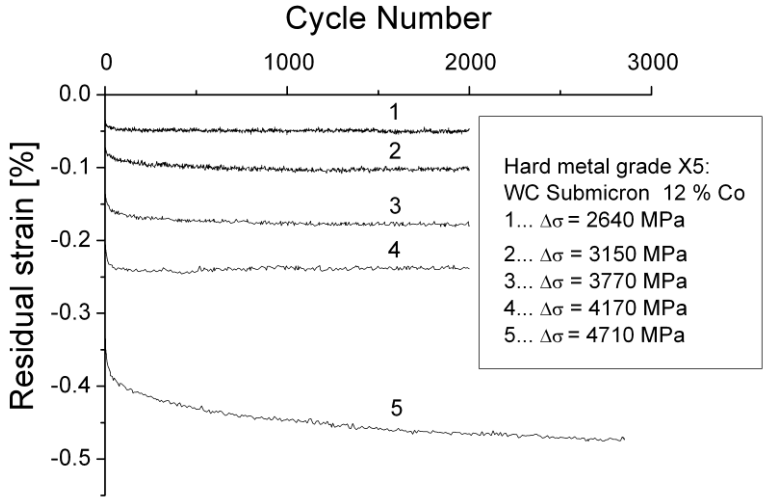

Fig. 67: Development of residual strain at zero applied stress with number of cycles at $R = -\infty$ for hard metal grade X5 [63]

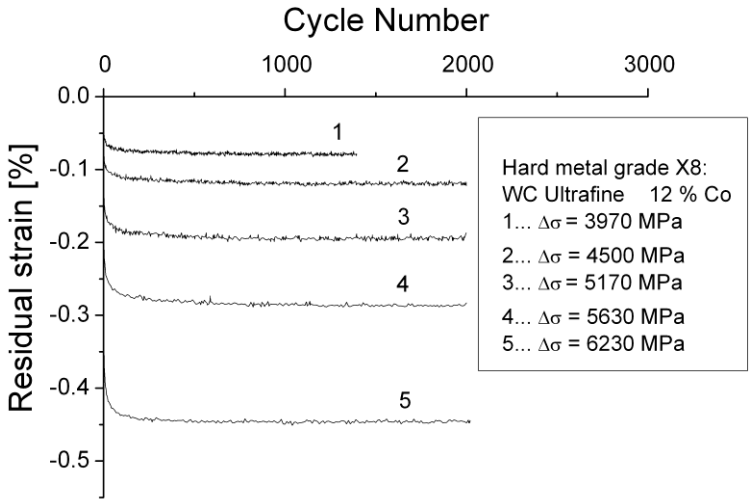

Fig. 68: Development of residual strain at zero applied stress with number of cycles at $R = -\infty$ for hard metal grade X8 [63]

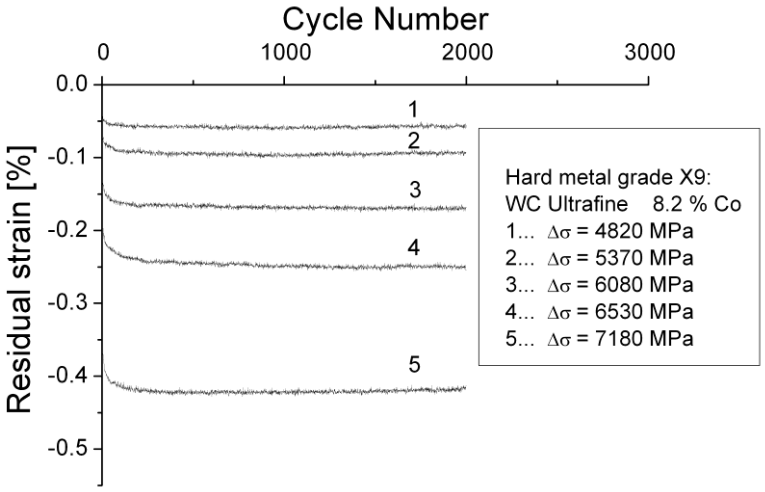

Fig. 69: Development of residual strain at zero applied stress with number of cycles at $R = -\infty$ for hard metal grade X9

The results of the ratchetting experiments lead to the following conclusions:

I. Levels of residual strain increase with an increase in applied stress.

II. At the same binder content, finer WC grain sizes lead to less residual strain at the same level of applied stress range.

III. At the same WC grain size, a decrease in binder content, i. e. an increase in reinforcement phase volume fraction leads to less residual strain.

(The items I-III are clearly reflected in Fig. 70)

A study of the cyclic stress-strain behaviour of Al alloys reinfoced with SiC particles concluded analogue to item III [115].

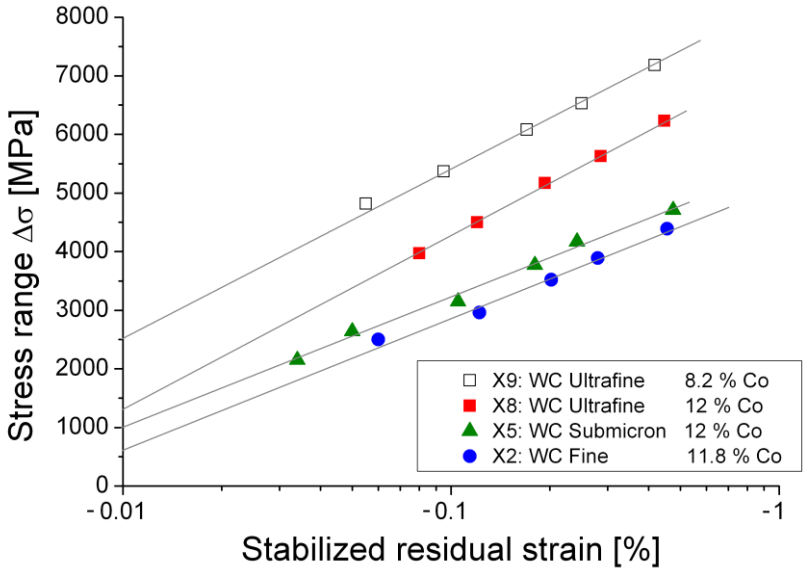

Fig. 70: Relationship between applied stress range and stabilized residual strain present in specimens of geometry S1 at zero applied stress for four hard metal grades at $R = -\infty$. Diagram enhanced by data of hard metal grade X9, compared to diagram presented in [63]

Interestingly the level of stabilized residual strain depends linearly on the amount of residual strain after the first loading cycle (see Fig. 71). This fact can be rationalised by considering that a certain amount of energy has been introduced into the specimen in the first load cycle by plastic deformation. This energy, stored in the specimen in the form of residual stresses, is the driving force for the development of the ratchetting strain and is proportional to the extent of plastic straining in the first loading cycle.

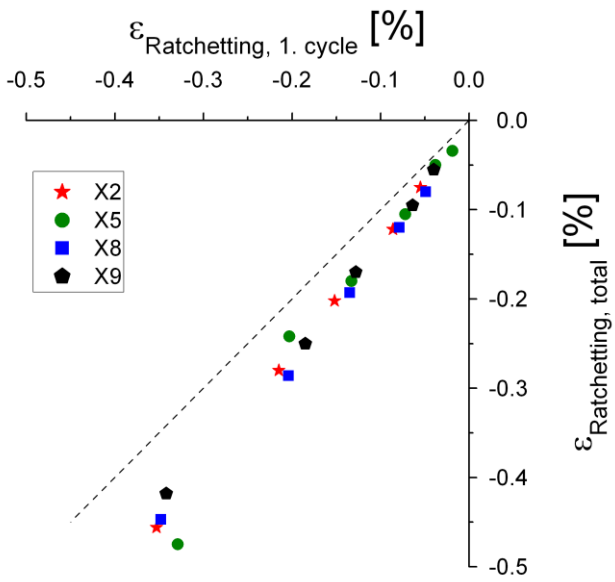

Fig. 71: Residual strain after first load cycle versus stabilized residual strain level for four hard metal grades at $R = -\infty$, dashed line under 45° as guide for the eyes

7.2 Fracture behaviour under cyclic loading conditions

7.2.1 Fracture behaviour under uniaxial cyclic loading conditions

In general hard metals used for structural components have to cope with a broad variety of loading conditions ranging from fluctuating tensile loads via alternating loads to fluctuating compression load. In many applications as tool materials, hard metals are subjected to cyclic loads with a high compressive mean stress. Taking into account residual tensile stresses caused by local plastic deformation, the stress ratio present in application can differ from the applied stress ratio [116], it can e.g. be between $R = -1$ and $R = -5$.

In this section, the dependence of stress amplitude-life (S-N) behaviour [117] and fatigue crack growth threshold on stress ratios, as well as the influence of overloads on the cyclic fracture behaviour of hard metals are discussed.

7.2.1.1 S-N behaviour under various stress ratios

To study the influence of stress ratio R on the cyclic fracture behaviour of the ultrafine grained WC-Co hard metal grade X8 under uniaxial compression loading conditions, R was varied from 0.1 via -1 to -3 in load controlled tests at a frequency of 10 Hz, using specimens of geometry S1. Results of the fatigue tests, performed up to 10^6 load cycles, are displayed in Fig. 72 in the form of stress amplitude-life (S-N) curves [117] in which the amplitude of applied stress is plotted versus the number of cycles to failure.

Results shown in Fig. 72 lead to the conclusion that the sustainable stress amplitude increases with decreasing stress ratio i.e. with increasing compressive mean stress. All S-N-curves show a significant scatter in the fatigue data and especially the S-N curves for R = 0.1 and R = -1 exhibit a rather low slope. Note that the fatigue tests were performed using specimens with an hourglass shape (geometry S1) and that in many cases fracture occurred not at the minimum sample diameter but at distances up to 10 mm away from it. Therefore, the S-N curves contain a set of data points that consider the nominal stress at the smallest cross section (filled symbols) and a second set of data points for which the stress was determined at the position of the fracture origin (open symbols). Triangles in Fig. 72 represent tests that were stopped at or slightly above 10^6 load cycles. Some specimens fractured already in the first load cycle. All specimens were taken from one and the same material batch to ensure comparable material quality in all the tests.

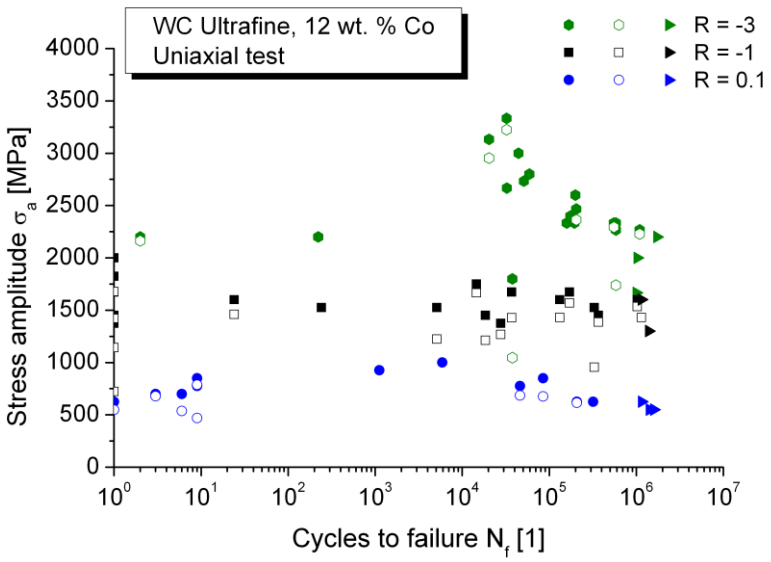

Fig. 72: Applied stress amplitude versus number of cycles to failure (S-N curve) for hard metal grade X8 for various stress ratios; symbols explained in the text

Defects similar to the ones shown in chapter 6.2 such as pores, inclusions or aggregates of WC grains larger than the average grain size were identified as crack origins. The scatter of the size of defects, from which fatigue crack growth starts, causes the large scatter of the S-N data. Low numbers of cycles to failures are due to large crack origins because only very little fatigue crack growth is necessary before the cracks reach their critical length which is determined by the local stress and the fracture toughness of the hard metal.

7.2.1.2 Dependence of fatigue crack growth threshold on stress ratio

An estimate of the threshold of stress intensity factor range ΔK_{th}, at which fatigue crack growth starts, was performed on the basis of Murakami's √area concept using Eq. 14 and Eq. 15 for surface flaws and internal flaws respectively [118].

$$\Delta K_{th,S} = 3.3 \cdot (H\!V + 120) \cdot (\sqrt{area})^{1/3} \cdot \left(\frac{1-R}{2}\right)^{a} \quad \text{for fracture origins at the surface} \qquad (14)$$

$$\Delta K_{th,i} = 3.5 \cdot (H\!V + 120) \cdot (\sqrt{area})^{1/3} \cdot \left(\frac{1-R}{2}\right)^{a} \quad \text{for internal fracture origins} \qquad (15)$$

The symbol A describes the projected area in the direction of the maximum stress and $\Delta\sigma$ represents the stress range (equal to two times the applied stress amplitude). The area A of the origins of fracture was determined from SEM micrographs taken from fracture surfaces. For each fatigue crack origin the initial stress intensity factor range ΔK at the start of FCG (ΔK_{start}) was calculated on the basis of Eq. 14 or Eq. 15 using the projected area of the initiation flaw from the SEM micrographs and the stress range actually present at the position of the fracture origin (non-constant specimen diameter).

An example of a fatigue crack origin found in the investigated hard metals is displayed in Fig. 73 [63]. In the immediate surroundings of the micro- pore, no "dimples" or "ridges" as they are typically formed during unstable crack growth [119] are visible. This is an indication of stable fatigue crack propagation in the material [119]. For clarification, the approximate sizes of the fatigue crack origin and the area of stable fatigue crack propagation are indicated by white dashed lines in Fig. 73.

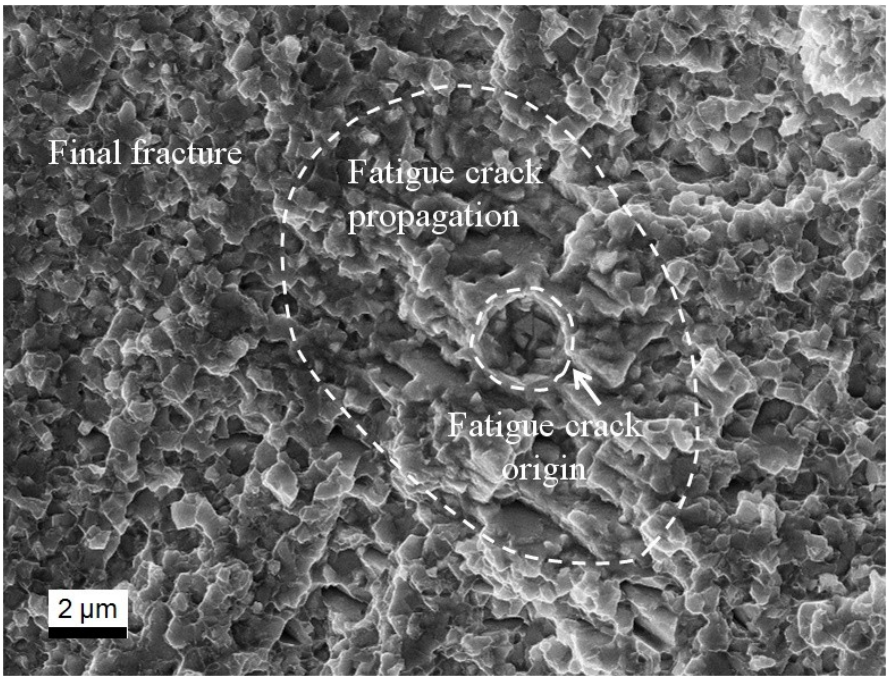

Fig. 73: Origin of fracture in a sample of hard metal grade X8 tested under cyclic loading conditions at R = -1 [63]

The minimum value of initial stress intensity factor range values ΔK_{start} of all the investigated specimens of the hard metal grade X8, at different stress ratios R, at the

respective stress ratio are given in Table 11. These values represent an estimate for the upper bound of ΔK_{th} values. The results indicate that ΔK_{th} rises with decreasing stress ratio [63] i.e. with enhanced compressive mean stress similar to results found for tools steels [120].

	R = 0.1	R = -1	R = -3
$\Delta K_{start,min}$ [MPa√m]	4.3	6.2	9

Table 11: Minimum values of stress intensity factor range at which fatigue crack growth started in samples of hard metal grade X8 under various stress ratios [63]

7.2.1.3 Influence of overloads on S-N behaviour

In industrial practice tools may be subject to mechanical overloads that might affect the tool material's mechanical strength. A comparison of ultimate compression strength in samples of WC-Co hard metal with binder contents ranging from 15 to 25 wt % in a virgin and a highly pre-deformed state (non-uniform compression applied from all sides [121]) has been performed by other authors [122]. To investigate the possible influence of mechanical overloads on cyclic material properties, series of stress amplitude-life experiments performed with specimens of different load history were compared in terms of S-N behaviour.

A set of specimens of geometry S1, made of hard metal grade X8 was tested under a load ratio R of 0.1 (data displayed in Fig. 72). Other sets of specimens from the same material batch were loaded monotonously in compression prior to cyclic testing up to stress levels equivalent to the flow stress values $R_{p0.1}$, $R_{p0.2}$ and $R_{p0.3}$ of the material. The impact of this preloading procedure on the cyclic fracture behaviour was found to be negligible as displayed in Fig. 74.

The reason for this kind of behaviour can be assumed to be the prevailing influence of defects present in the "as produced" material microstructure. Defects possibly generated by the preload that caused macroscopic plastic deformation are found to be non-existent or smaller than the defects already present in the material before the application of the preload. Fig. 75 shows an origin of fracture observed on the fracture surface of a

specimen (typically located in the specimen bulk and not at the specimen surface) loaded in compression up to 4900 MPa prior to fatigue testing. The presence of features of stable fatigue crack propagation [119] surrounding the defect, being a spherical-shaped pore, indicates that the effective defect size remains unaffected by plastic deformation applied prior to cyclic loading.

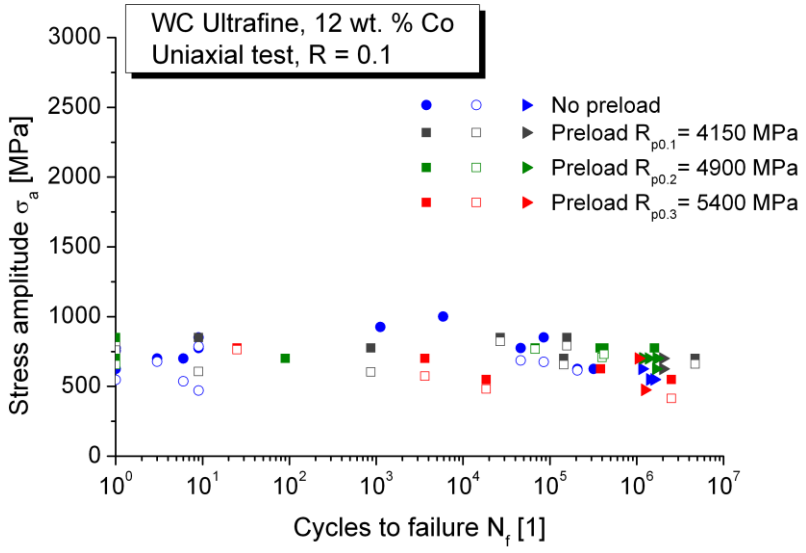

Fig. 74: Comparison of S-N behaviour of specimens with and without compression load prior to cyclic testing under *R*= 0.1; specimen geometry S1, hard metal grade X8; symbols used as in Fig. 72

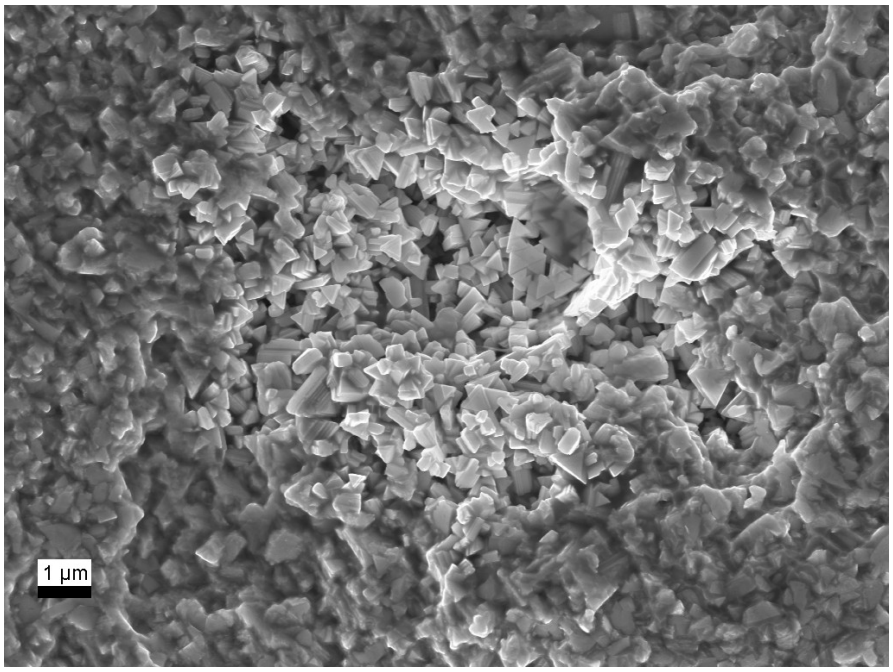

Fig. 75: Fracture of origin in a specimen of geometry S1 made of hard metal grade X8 loaded in compression up to 4900 MPa ($R_{p0.2}$) prior to cyclic loading under R = 0.1

7.2.1.4 Influence of material batch on S-N behaviour

Since the number of load cycles to failure at constant load amplitude depends strongly on the size of the initial defect from which fatigue crack growth starts, the cyclic fracture behaviour depends on the defect population present in a certain material batch. To compare the cyclic fracture behaviour of materials from two different production batches of the hard metal grade X8, specimens of geometry S1 were tested in uniaxial tests under a stress ratio *R* of 0.1. There exists a difference in the cyclic fracture behaviour between the two material batches as shown in Fig. 76. Material batch number 2 exhibits a higher tolerance to cyclic loads than material from batch number 1. The reason for this kind of behaviour is found to be a smaller average defect size in material batch 2.

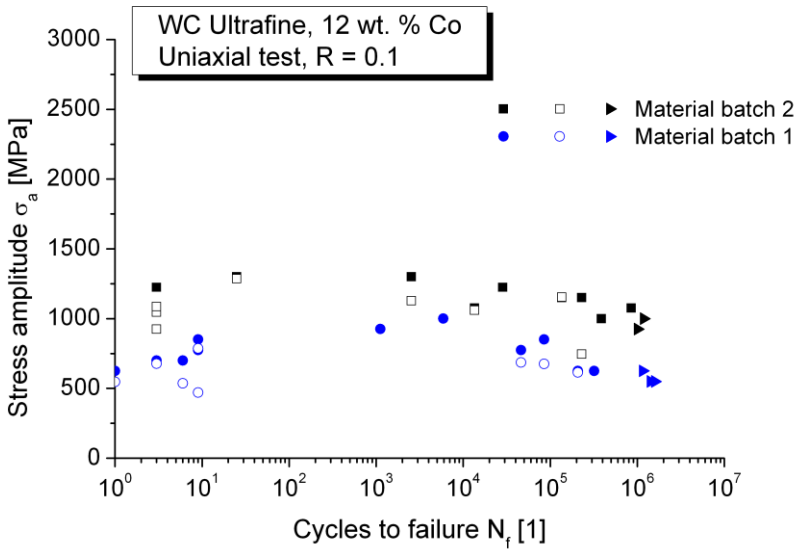

Fig. 76: S-N behaviour of specimens of geometry S1 made of two different batches of hard metal grade X8 under a stress ratio of *R*=0.1; symbols used as in Fig. 72

7.2.2 Fracture behaviour under cyclic bending loading conditions

The influence of machining technology applied to form a tool's contour has a major influence on tool performance in industrial application. The presence or absence of machining induced surface damage as well as the residual stress state are important factors influencing fatigue life.

7.2.2.1 Influence of surface finish on S-N behaviour

A common tool shaping technology for hard materials also used for WC-Co hard metals is electrical discharge machining (EDM) [123]. The elevated temperatures arising during the EDM process, in which an electrode is moved towards the work piece until the imposed electric voltage is high enough to ionize a dielectric media separating the two bodies, leave behind a thermally affected zone of several micrometres in thickness, as indicated in Fig. 77 by a black arrow. The thermally affected zone is associated with a molten surface layer containing micro-cracks (indicated in Fig. 77 by white arrows) running vertical or parallel to the surface [3]. Also, a region of increased contrast in the

Co binder phase is discernible in the SEM image which indicates increased tungsten content dissolved in the Co due to its rapid solidification after melting.

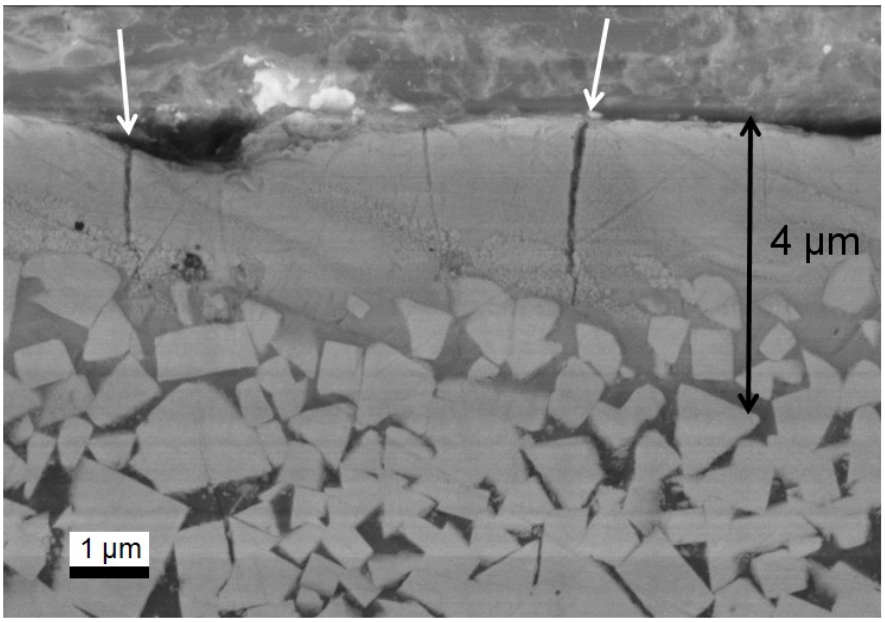

Fig. 77: Cross section polish of an EDMed surface of a specimen made of the hard metal grade X2 showing a thermally affected surface region with a molten surface layer containing microcracks

Many variants of the EDM technology exist varying in electrode shape (wire-cutting or die sinking) and dielectric media (oil, oil/powder suspension, water or gas) [123]. The addition of electrically conductive powders to dielectric oils has been shown to improve the obtained surface finish, the use of water and gases as dielectric media improve the environmental friendliness and cost effectiveness of the EDM process [123]. A variant of the technology suitable for micro machining combines conventional EDM with ultrasonic vibration to improve debris removal [123]. The extent to which the machined surface is influenced by the applied EDM technique in terms of obtained surface roughness, recast layer thickness and surface cracking tendency depends, for example, on the thermal conductivity i.e. the cobalt content of the machined hard metal [3], the used discharge energy, pulse duration and frequency [124], as well as the working gap width and the used electrode material [125].

Due to the damage done to the EDMed surface, the mechanical performance of the material under static and cyclic loading is degraded [126] as can be seen in Fig. 78,

comparing sets of specimens of geometry S5, made of hard metal grade X2, with ground and EDMed surfaces. The fatigue limits under a stress ratio of R = 0.1 after $2*10^6$ load cycles as evaluated via a staircase test [127] were 980 ± 20 MPa in the case of the ground specimens and 450 ± 40 MPa for the EDMed specimens. The roughness values of the EDMed and ground surfaces, as characterised by the average roughness R_a, were comparable in magnitude, being 0.30 µm and 0.25 µm respectively, which indicates that it is not a difference in surface roughness that causes the dramatic decrease of the fatigue strength.

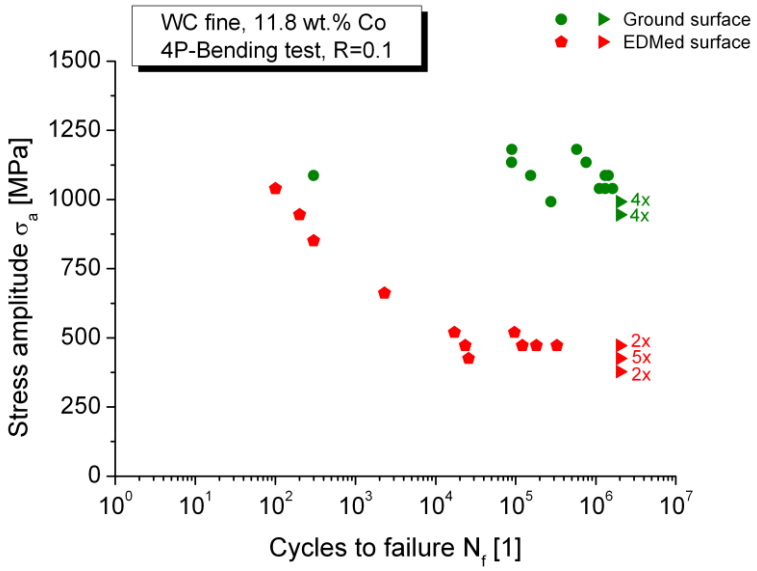

Fig. 78: Comparison of S-N behaviour of specimens with ground and EDMed surfaces tested in four point bending; geometry S5, hard metal grade X2, stress ratio R = 0.1; symbols used as in Fig. 72

To emphasise that cracks from the EDM procedure are the cause for failure in the EDMed specimens, an example for an origin of fracture is shown in an overview in the centre of the fracture mirror [62] in Fig. 79. More detail of the origin of fracture representing a coalescence of EDM induced microcracks is shown in Fig. 80.

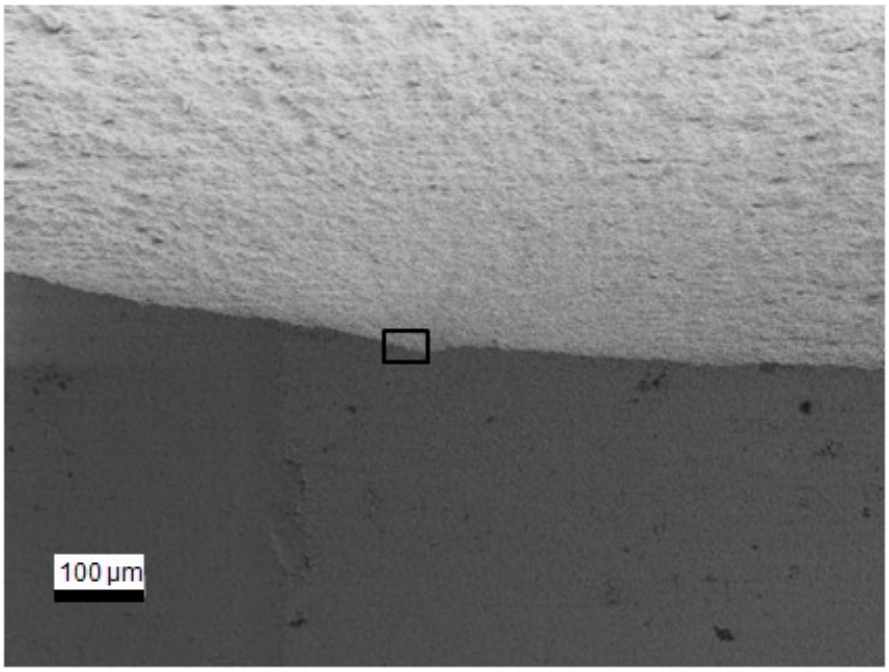

Fig. 79: Fracture surface of a specimen of geometry S5 made of hard metal grade X2; image inclined under 45°; upper image section: fracture surface with centre of mirror zone [62] indicated by black rectangle; lower image section: EDMed lateral sample surface

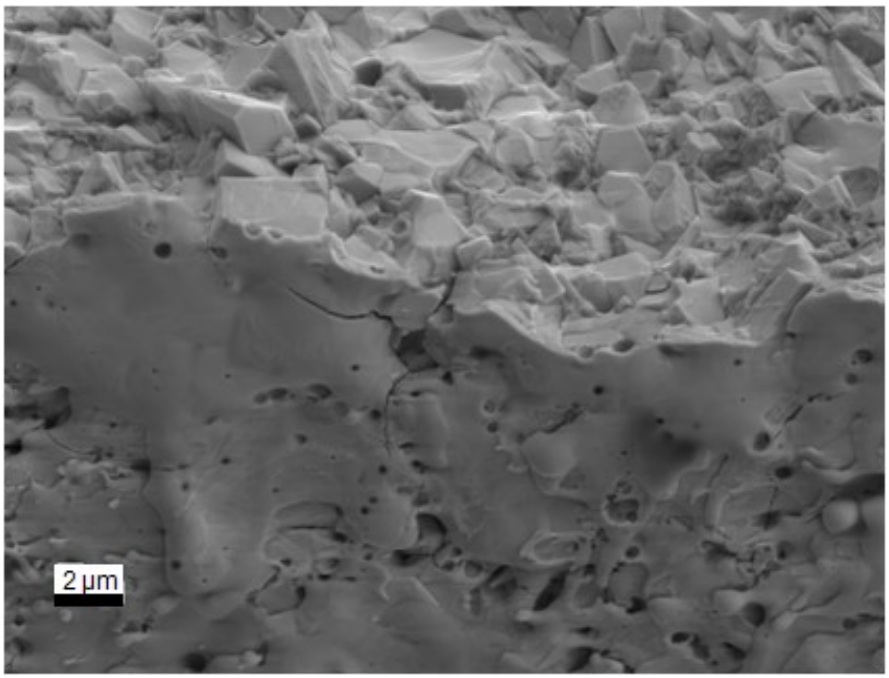

Fig. 80: Detail of fracture surface as marked in Fig. 79 showing the origin of fracture being a coalescence of EDM-induced microcracks

7.2.2.2 Influence of residual stress state on S-N behaviour

Besides the mentioned influence of surface cracking on the mechanical properties of WC-Co hard metal, the residual stress state also plays an important role regarding fatigue life since load induced stresses are superimposed with the residual stresses.

A possibility to determine residual stresses from lattice strains is the widely used $\sin^2\psi$ method [128] which was applied for the residual stresses in the WC phase using CrK_α radiation with an approximate beam diameter of 1 mm. To attain a depth profile of residual stresses the sample surface was removed electrochemically in layers to facilitate measurements beneath the original surface. A comparison of these depth profiles of the residual stresses measured in axial direction in specimens used to generate the S-N plot in Fig. 78 is displayed in Fig. 81. The residual stresses at the surface of the ground specimens have high compressive values [67] of around 2000 MPa. In the EDMed specimen surface, the residual stresses were found to be tensile with values of about 560 ± 100 MPa as previously demonstrated in [129]. The residual stresses decline very quickly, reaching a plateau value [67] of about 250 MPa in compression in both surface finish variants, already a few micrometres from the sample surface, as indicated in Fig. 81 by coloured lines as guides for the eyes. The measured plateau value of compressive residual stress in the WC phase is caused by the balance of eigenstresses present in the WC and the Co phase induced upon solidification after liquid phase sintering. The Co phase contracts more than the WC phase due to the difference in thermal expansion coefficients and is therefore under tensile residual stress in the sintered microstructure [130]-[133].

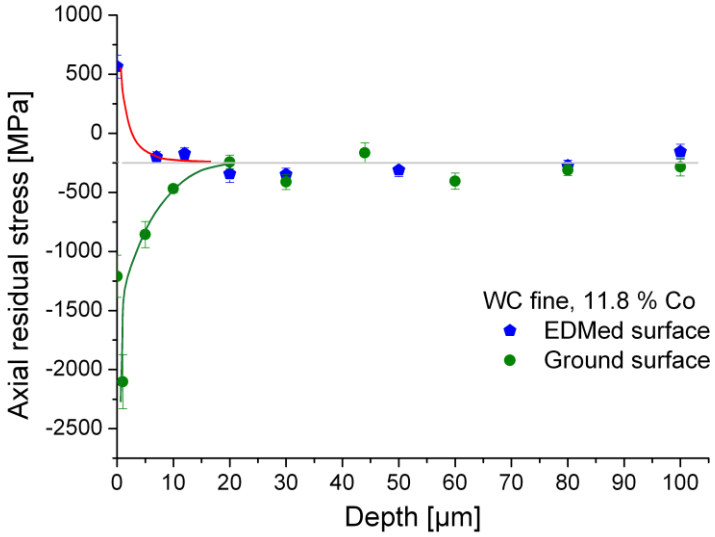

Fig. 81: Depth profile of axial residual stresses in a specimen of geometry S5 made of hard metal grade X2

To determine the role of residual stresses regarding fatigue life of WC-Co materials decoupled from the impact of differences in surface finish, the S-N behaviour of equally ground specimens was compared. Half of the specimens were annealed in a vacuum furnace for 2 hours at 900°C to remove the residual stresses introduced by the grinding procedure: Fig. 82 compares depth profiles of axial residual stress in the WC phase in ground and ground & annealed specimens of geometry S2 made from hard metal grade X11, that clearly show the reduction of the compressive residual stresses from -1955 ± 270 MPa at the surface of the ground specimen to 40 ± 150 MPa at the surface of the ground & annealed sample. The plateau value of compressive stress in the ground specimen is reached at a depth of about 20 µm.

The well-known beneficial effect of compressive stress on fatigue performance [134] also appears in the present case, elevating the fatigue limit determined after 2.10^6 load cycles from a level of to 550 ± 30 MPa in the ground & annealed specimens to 1250 ± 90 MPa in the ground specimens (see Fig. 83).

The average surface roughness R_a was again comparable in the compared specimens with values of 0.84 µm for the ground state and 0.78 µm for the ground & annealed state.

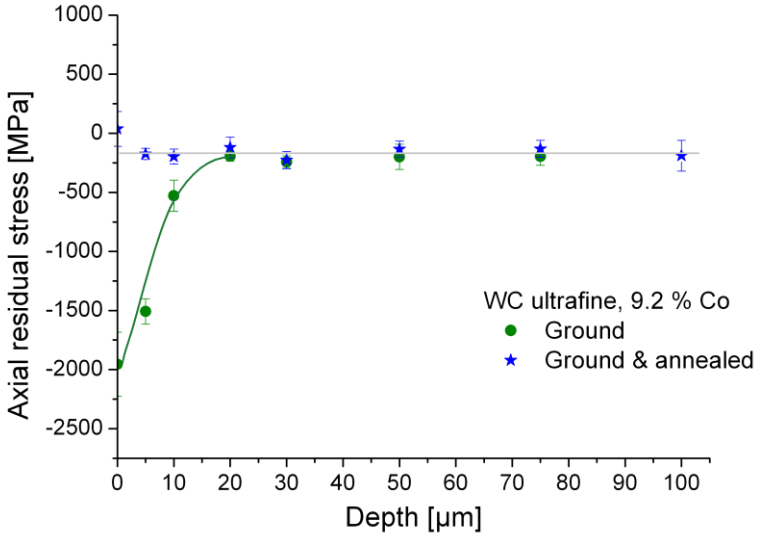

Fig. 82: Depth profile of axial residual stresses in ground and ground & annealed specimens of geometry S2 made of hard metal grade X11

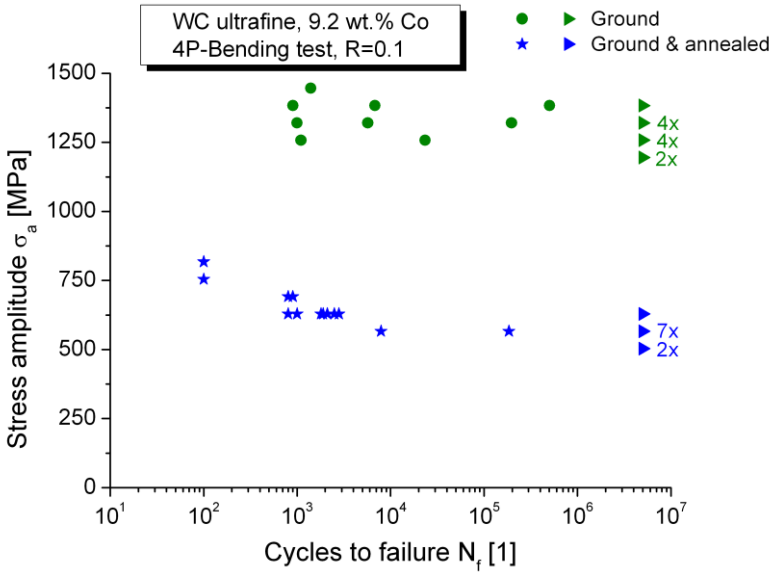

Fig. 83: Comparison of S-N behaviour of specimens in a ground and a ground & annealed state; tested in four point bending; geometry S2, hard metal grade X11, stress ratio R = 0.1; symbols used as in Fig. 72

The occurrence of the compressive residual stress can be interpreted as a shift in stress ratio from the applied one of R = 0.1 to an effective stress ratio that would be about R = -2.2. This change can also help to explain the observed doubling of the compared fatigue limits: The fatigue limit can be assumed to be directly proportional to ΔK_{th} (see

e.g. Eq. 14). The value of ΔK_{th} is about twice as high at R = -2.2 compared to its value at R = 0.1 for an ultrafine grained WC-Co hard metal containing 12 wt % Co binder (compare Table 11 and Fig. 84 with lines as guides for the eyes). Assuming that the values of ΔK_{th} are similar for ultrafine grained hard metal with 9.2 wt % Co binder, one can conclude as follows: The decrease in stress ratio due to the presence of compressive residual stress leads to an increase in ΔK_{th} and fatigue limit to values about twice as high as without the residual stress.

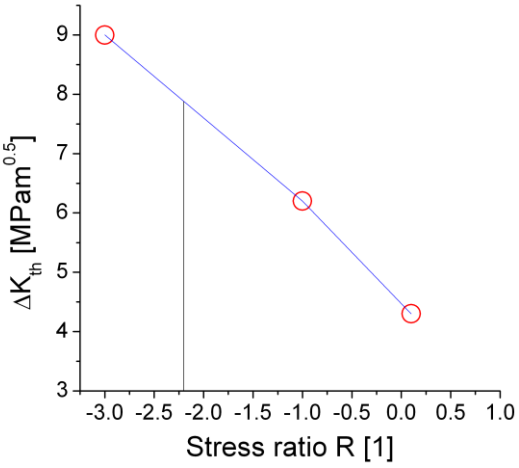

Fig. 84: Estimates of ΔK_{th} values versus stress ratio R for hard metal grade X8 with ultrafine WC grain size and 12 wt % Co binder

In both the ground and the ground & annealed specimens, fracture origins were identified as grooves from grinding that were about 5 µm deep as shown in Fig. 85. At this distance from the surface, the compressive residual stresses can still act protectively since they compensate crack-driving load-induced tensile stresses.

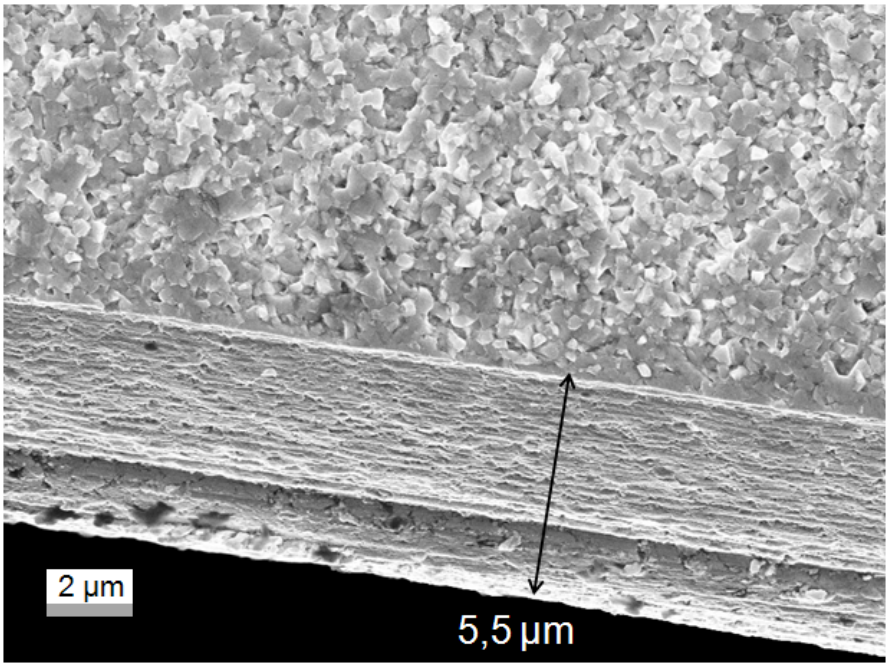

Fig. 85: Origin of fracture being a grove from grinding in a ground & annealed specimen of geometry S2 made of hard metal grade X11

It can be concluded that that compressive residual stresses protect the surface and inhibit defect growth from it, if the residual stresses act as deeply as the defects are located.

8 Summary and Outlook

In the present work, a material testing procedure for the reliable determination of the stress-strain response of WC-Co hard metals in tension and compression under static and cyclic loading conditions was presented.

The flow curves attained under monotonous loading conditions revealed a surprisingly high degree of plastic deformation prior to failure under compression loading conditions. Material data such as yield strength and Young's modulus were determined indicating a pronounced influence of material composition and microstructure on the flow behaviour. A qualitative relation of a so-called matricity parameter with flow behaviour found by other authors using numerical methods was retrieved in an experimental study.

Regarding the cyclic stress-strain behaviour of hard metals, the influence of composition and microstructure on the development of ratchetting strain was described. Under purely compressive cyclic loading, the incremental contribution to total cyclic deformation decreases within consecutive load cycles and stabilizes at a certain value. This stabilized value, referred to as ratchetting strain, increases with increasing binder content at a constant WC grain size. At constant binder content, a decrease in WC grain size leads to smaller ratchetting strain values. Ratchetting strain was also found to be proportional to the strain in the first load cycle.

The potential in terms of tensile fracture strength of ultrafine grained WC-Co hard metals free from processing heterogeneities was shown to be about 6000 MPa by comparing a number of specimens differing widely in size and effectively tested volume.

In addition, the cyclic fracture behaviour of WC-Co hard metals was studied. The value of stress intensity factor range at which fatigue crack growth starts from material inhomogeneities such as pores, inclusions or agglomerates of enlarged WC grains was found to increase with a decrease in the applied stress ratio. Mechanical overloads, as occurring frequently in application, were found not to significantly influence the cyclic fracture behaviour of WC-Co hard metals in currently available hard metal grades. The

detrimental influence of inappropriate surface finishing techniques and unfavourable residual stress states of technical surfaces on cyclic fracture behaviour was demonstrated.

The results of the present work reveal a high potential of WC-Co hard metals for the future applications in highly cyclically loaded components and tools, e.g. in fine blanking application. Their flow strength levels are tunable by the appropriate choice of WC grain size, binder content and binder matricity and exceed values about twice as high as those of high speed steels.

9 References

[1] Amberg S, Doxner H: Porosity in cemented carbide. *Powder Metall* **1** (1977), pp. 1-10

[2] Luyckx SB: Role of inclusions in the fracture initiation process in WC-Co alloys. *Acta Metall* **23** (1975), pp. 109-15

[3] Lenz E, Katz E, Konig W, Wertheim R: Cracking behaviour of sintered carbides during EDM. *Ann CIRP* **24** (1975), pp. 109–14

[4] Danzer R, Lube T, Supancic P, Damani R: Fracture of ceramics. *Adv Eng Mater* **10** (2008) [4], pp. 275-98

[5] Weibull W: A Statistical Theory of the Strength of Materials. Generalstabens Litografiska Anstalts Förlag, Stockholm (1939), pp. 1-45

[6] Weibull W: A statistical distribution function of wide applicability. *J Appl Mech* **18** (1951), pp. 293-8

[7] Quinn GD: Weibull effective volumes and surfaces for cylindrical rods loaded in flexure. *J Am Ceram Soc* **86** (2003) [3], pp. 475–79

[8] Griffith AA: The phenomena of rupture and flow in solids, *Philos Trans R Soc London Ser* **A221** (1921), pp. 163–98

[9] Irwin GR: Analysis of stresses and strains near the end of a crack traversing a plate. *J Appl Mech* **24** (1957), pp. 361–4

[10] Murakami Y: Stress intensity factors handbook Volume **2**. 3rd edition, Elsevier, Kyoto (1999), pp. 684-5

[11] Murakami Y: Stress intensity factors handbook Volume **1**. 3rd edition, Elsevier, Kyoto (1999), pp. 118-9

[12] ENV843-5 Advanced Technical Ceramics, Monolithic Ceramics, Mechanical Tests at Room Temperature, Part 5: Statistical Analysis (1997)

[13] Danzer R: Some notes on the correlation between fracture and defect statistics: Are Weibull statistics valid for very small specimens?. *J Am Ceram Soc* **26** (2006), pp. 3043–49

[14] Danzer R: A general strength distribution function for brittle materials. *J Eur Ceram Soc* **10** (1992), pp. 461-72

[15] Quinn GD: Weibull Strength Scaling for Standardized Rectangular Flexure Specimens. J *Am Ceram Soc* **86** (2003) [3], pp. 508–10

[16] Danzer R, Supancic P, Pascual J, Lube T: Fracture statistics of ceramics – Weibull statistics and deviations from Weibull statistics. *Eng Fract Mech* **74** (2007), pp. 2919-32

[17] Danzer R, Lube T, Supancic P: Monte Carlo simulations of strength distributions of brittle materials – Type of distribution, specimen and sample size. *Z Metallkd* **92** (2001), pp. 773-83

[18] Afferante L, Ciavarella M, Valenza E: Is Weibull modulus really a material constant? Example case with interacting collinear cracks. *Int J Solids Struct* **43** (2006), pp. 5147-57

[19] Gurland J: The measurement of grain contiguity in two-phase alloys. *Transactions AIME* **212** (1958), pp. 452-5

[20] Poech MH, Ruhr D: Quantitative characterization of the microstructural arrangement. *Prakt Metallogr* **31** (1994), pp. 70-77

[21] Poech MH, Fischmeister HF, Kaute D, Spiegler R: FE-modelling of the deformation behaviour of WC-Co alloys. *Comp Mater Sci* **1** (1993), pp. 213-24

[22] Leßle P, Dong M, Soppa E, Schmauder S: Simulation of interpenetrating microstructures by self consistent matricity models. *Scr Mater* **38** (1998) [9], pp. 1327-32

[23] Leßle P, Dong M, Schmauder S: Self-consistent matricity model to simulate the mechanical behaviour of interpenetrating microstructures. *Comp Mater Sci* **15** (1999), pp. 455-65

[24] Upadhyaya GS: Materials science of cemented carbides – an overview. *Mater Des* **22** (2001), pp. 483-89

[25] Schedler W: Hartmetall für den Praktiker, VDI-Verlag, Düsseldorf (1988) pp. 21-27

[26] Yamamoto T, Ikuharaa Y, Sakumab T: High resolution transmission electron microscopy study in VC-doped WC-Co compounds. *Sci Technol Adv Mater* **1** (2000), pp. 97- 104

[27] Fang ZZ, Wang X, Ryu T, Hwang KS, Sohn HY: Synthesis, sintering, and mechanical properties of nanocrystalline cemented tungsten carbide – A review. *Int J Refract Met Hard Mater* **27** (2009), pp. 288-99

[28] Engel U, Hübner H: Strength improvement of cemented carbides by hot isostatic pressing (HIP). *J Mater Sci* **13** (1978), pp. 2003-12

[29] Schedler W: Hartmetall für den Praktiker, VDI-Verlag, Düsseldorf (1988) pp. 126-30

[30] Gurland J, Bardzil P: Relation of strength, composition, and grain size of sintered WC-Co alloys. *J Met* **7** (1955), pp. 311-5

[31] Liu B, Zhang Y, Ouyang S: Study on the relation between structural parameters and fracture strength of WC-Co cemented carbides. *Mater Chem Phys* **62** (2000), pp. 35-43

[32] Mari D, Bolognini S, Feusier G, Viatte T, Benoit W: Experimental strategy to study the mechanical behaviour of hardmetals for cutting tools. *Int J Refract Met Hard Mater* **17** (1999), pp. 209-25

[33] Roebuck B, Almond EA: Deformation and fracture processes and the physical metallurgy of WC-Co hardmetals. *Int Mater Rev* **33** (1988) [2], pp. 90-110

[34] Ferreira JAM, Pina Amaral MA, Antunes FV, Costa JDM: A study on the mechanical behaviour of WC/Co hardmetals. *Int J Refract Met Hard Mater* **27** (2009), pp. 1–8

[35] Ingelstrom N, Nordberg H: The fracture toughness of cemented tungsten carbides. *Eng Fract Mech* **6** (1974), pp. 597-607

[36] Sigl LS, Fischmeister HF: On the fracture toughness of cemented carbides. *Acta Metall* **36** (1988) [4], pp. 887-97

[37] Sigl LS, Exner HE: The flow stress and hardness of metal-reinforced brittle composites. *Mater Sci Eng* **A108** (1989), pp. 121-9

[38] Roebuck B: Terminology, testing, properties, imaging and models for fine grained hardmetals. *Int J Refract Met Hard Mater* **13** (1995), pp. 265-79

[39] Roebuck B: Extrapolating hardness-structure property maps in WC/Co hardmetals. *Int J Refract Met Hard Mater* **24** (2006), pp. 101-8

[40] Torres Y, Casellas D, Anglada M, Llanes L: Fracture toughness evaluation of hardmetals: influence of testing procedure. *Int J Refract Met Hard Mater* **19** (2001), pp. 27–34

[41] Schubert WD, Neumeister H, Kinger G, Lux B: Hardness to toughness relationship of fine-grained WC-Co hardmetals. *Int J Refract Met Hard Mater* **16** (1998), pp.133-42

[42] Cha SI, Hong SH, Ha GH, Kim BK: Microstructure and mechanical properties of nanocrystalline WC-10Co cemented carbides. *Scripta mater* **44** (2001), pp. 1535–9

[43] Jia K, Fischer TE, Gallois B: Microstructure, hardness and toughness of nanostructured and conventional WC-Co composites. *Nanostruct Mater* **10** (1998) [5], pp. 875-91

[44] Fang ZZ, Wang X, Ryu T, Hwang KS, Sohn HY: Synthesis, sintering, and mechanical properties of nanocrystalline cemented tungsten carbide – A review. *Int J Refract Met Hard Mater* **27** (2009), pp. 288-99

[45] Toensing CH: Tensile testing of cemented carbides. AMSE Publication 66-MD-52

[46] Nishimatsu C, Gurland J: Experimental survey of the deformation of the hard-ductile two-phase alloy system WC-Co. *Trans Am Soc Met* **52** (1960), pp. 469-84

[47] Doi H, Fujiwara Y, Miyake K: Mechanism of plastic deformation and dislocation damping of cemented carbides. *TMS AIME* **245** (1969), pp. 1457–70

[48] Dusza J, Parilák L, Diblk J, Slesár M: Elastic and plastic behaviour of WC-Co composites. *Ceram Int* **9** (1983) [4], pp. 144-6

[49] Okamoto S, Nakazono Y, Otsuka K, Shimoitani Y, Takada J: Mechanical properties of WC/Co cemented carbide with larger WC grain size. *Mater Charact* **55** (2005), pp. 281-7

[50] Johansson I, Persson G, Hiltscher R: Determination of static and fatigue compressive strength of hard metals. *Powder Metal* **13** (1970) [26], pp. 449-63

[51] Bronsted P, Skov-Hansen P: Fatigue properties of high strength materials used in cold-forging tools. *Int J Fatigue* **20** (1998) [5], pp. 373-81

[52] DIN EN 10002-4 b resp. ISO 9513

[53] Beitz W, Küttner K-H: Dubbel – Taschenbuch für den Maschinenbau, 18th edition, Springer, Berlin (1995), pp. C42-3

[54] Kluensner T, Marsoner S, Ebner R, Glaetzle J, Pueschel A, Pippan R: Influence of Microstructure on Stress-Strain Behaviour of WC-Co Hard Metals in Static and Cyclic Loading. *Proc 17th Int Plansee Seminar* **3** (2009), Reutte, Austria, pp. AT10/1-10

[55] Uchic MD, Dimiduk DM, Florando JN, Nix WD: Sample Dimensions Influence Strength and Crystal Plasticity. *Science* **305** (2004), pp. 986-9

[56] Kiener D, Grosinger W, Dehm G, Pippan R: A further step towards understanding of size-dependent crystal plasticity: In situ tension experiments of minaturized single-crystal copper samples. *Acta Mater* **56** (2008), pp. 580-92

[57] Motz C, Schöberl T, Pippan R: Mechanical properties of micro-sized copper bending beams machined by the focused ion beam technique. *Acta Mater* **53** (2005), pp. 4269-79

[58] Di Maio D, Roberts SG: Measuring fracture toughness of coatings using focused-ion-beam-machined microbeams. *J Mater Res* **20** (2005) [2], pp. 299-302

[59] Matoy K, Schönherr H, Detzel T, Schöberl T, Pippan R, Motz C, Dehm G: A comparative micro-cantilever study of the mechanical behaviour of silicon based passivation films. *Thin Solid Films* **518** (2009), pp. 247-256

[60] Wurster S, Motz C, Pippan R: Notched-cantilever testing on the micrometer scale – effects of constraints on plasticity and fracture behaviour, *Proc 18th European Conference on Fracture* (2010) Dresden, Germany

[61] Wurster S, Motz C, Jenko M, Pippan R: Micrometer-Sized Specimen Preparation Based on Ion Slicing Technique. *Adv Eng Mater* **12** (2010) [1-2], pp. 61-4

[62] Lawn B: Fracture of brittle solids. 2nd edition, Cambridge University Press, Melbourne (1993), pp. 86-105

[63] Klünsner T, Marsoner S, Ebner R, Pippan R, Glätzle J, Püschel A: Effect of microstructure on fatigue properties of WC-Co hard metals. *Proc Eng* **2** (2010) [1], pp. 2001-10

[64] Golovchan VT, Litoshenko NV: The stress-strain behaviour of WC-Co hardmetals. *Comp Mater Sci* **49** (2010), pp. 593-7

[65] Doi H, Fujiwara Y, Miyake K, Oosawa Y: A systematic investigation of elastic moduli of WC-Co alloys. *Metall Trans* **1** (1970), pp. 1417-25

[66] Kouzeli M, Mortensen A: Size dependent strengthening in particle reinforced aluminium. *Acta Mater* **50** (1998) [16], pp. 5611-26

[67] Jaensson BO: Residual stresses and stress-strain behaviour of the WC-Co composite material. *Mater Sci Eng* **8** (1971), pp. 41-53

[68] Sundström BO: Elastic-plastic behaviour of WC-Co analysed by continuum mechanics. *Mater Sci Eng* **12** (1973), pp. 265-76

[69] Jaensson BO: Microstructural interpretation of the stress-strain behaviour of the WC-Co composite material. *Mater Sci Eng* **9** (1972), pp. 339-46

[70] Roebuck B, Almond EA, Cottenden AM: The influence of composition, phase transformation and varying the relative f.c.c. and h.c.p. phase content on the properties of dilute Co-W-C alloys. *Mater Sci Eng* **66** (1984), pp. 179-94

[71] Haglund S, Agran J: W content in Co binder during sintering of WC-Co. *Acta Mater* **8** (1998), pp. 2801-7

[72] Hellsing M: High resolution microanalysis of binder phase in WC-Co cemented carbides. *Mater Sci Technol* **4** (1988), pp. 824-9

[73] Arndt R: Plastizität von Hartmetallen auf WC-Co-Basis. *Z Metallkde* **63** (1972), pp. 274-80

[74] Sarin VK, Johannesson T: On the deformation of WC-Co cemented carbides. *Met Sci* **9** (1975), pp. 472-6

[75] Schleinkofer U, Sockel HG, Görting K, Heinrich W. Microstructural processes during subcritical crack growth in hard metals and cermets under cyclic loads. *Mater Sci Eng* **A209** (1996), pp.103-10

[76] Zahl DB, McMeeking RM: The influence of residual stress on the yielding of metal matrix composites. *Acta Metall Mater* **39** (1991) [6], pp. 1117-22

[77] Krawitz AD, Drake EF, Clausen B: The role of residual stress in the tension and compression response of WC-Ni. *Mater Sci Eng* **A527** (2010), pp. 3595-601

[78] Coats DL, Krawitz AD. Effect of particle size on the thermal residual stress in WC-Co composites. *Mater Sci Eng* **A359** (2003), pp. 338-42

[79] Schmauder S, Weber U, Soppa E: Computational mechanics of heterogeneous materials – influence of residual stresses. *Comp Mater Sci* **26** (2003), pp. 142-53

[80] Arzt E: Size effects in materials due to microstructural and dimensional constraints: A comparative review. *Acta Mater* **46** (1998) [16], pp. 5611-26

[81] Rajan K, Vandersande JB: Room temperature strengthening mechanisms in a Co-Cr-Mo-C alloy. *J Mater Sci* **17** (1982), pp. 769

[82] Schaller R, Mari D, Maamouri M, Ammann JJ: Mechanical behaviour of WC-11wt%Co studied by bending tests, internal friction and electron microscopy. *J Hard Mater* **3** (1992) [3-4], pp. 351-62

[83] Ericsson T: The temperature and concentration dependence of the stacking fault energy in the Co-Ni system. *Acta Metall* **14** (1966) [7], pp. 853-65

[84] Beeston BEP, Dillamoore IL, Smallman RE: The stacking fault energy of some Ni-Co Alloys. *Met Sci J* **2** (1968), pp. 12-4

[85] Ashbee KHG: Intersecting stacking faults in face-centered cubic lattices. *Acta Metall* **15** (1967), pp. 1129

[86] Östberg G, Buss K, Christensen M, Norgren S, Andrén HO, Mari D, Wahnström G, Reineck I: Mechanisms of plastic deformation of WC–Co and Ti(C, N)–WC–Co. *Int J Refract Met Hard Mater* **24** (2006), pp. 135–44

[87] Hall EO: The deformation and aging of mild steel: III Discussion of results. Proc Phys Soc B **64** (1951), pp. 747-53, London, United Kingdom

[88] Petch NJ: The cleavage strength of polycrystals. *J Iron Steel Inst* **174** (1953), pp. 25-8

[89] Poech MH, Fischmeister H, Spiegler R: Assessment of the in situ flow properties of the cobalt phase in WC-Co hard metals. *J Hard Mater* **2** (1991) [3-4], pp. 197-205

[90] Poech MH, Fischmeister HF: Deformation of two-phase materials: a model based on strain compatibility. *Acta Metall Mater* **40** (1992) [3], pp. 487-94

[91] Klünsner T, Wurster S, Supancic P, Ebner R, Jenko M, Glätzle J, Püschel A, Pippan R: Effect of specimen size on the tensile strength of WC-Co hard metal. *Acta Mater* **59** (2011), pp. 4244-52

[92] Beitz W, Küttner KH: Dubbel – Taschenbuch für den Maschinenbau, 18th edition, Springer, Berlin (1995), pp. C8-14

[93] http://www.simulia.com/products/abaqus_fea.html

[94] Cha SI, Lee KH, Ryu HJ, Hong SH: Effect of size and location of spherical pores on transverse rupture strength of WC-Co cemented carbides. *Mater Sci Eng* **A486** (2008), pp. 404-8

[95] Pezzotti G, Huebner H, Suenobu H, Sbaizero O, Nishida T: Analysis of Near-Tip Crack Bridging in WC/Co Cermet. *J Eur Ceram Soc* **19** (1999), pp. 119-23

[96] Felten F, Schneider GA, Sadowski T: Estimation of R-curve in WC/Co cermet by CT test. *Int J Refract Met Hard Mater* **26** (2008), pp. 55-60

[97] Torres Y, Bermejo R, Llanes L, Anglada M: Influence of notch radius and R-curve behaviour on the fracture toughness evaluation of WC–Co cemented carbides. *Eng Fract Mech* **75** (2008), pp. 4422-30

[98] Saltykov SA: *Stereometrische Metallographie*. VEB, Leipzig (1974), pp. 273-82

[99] Torres Y, Anglada M, Llanes L. Fatigue mechanics of WC-Co cemented carbides. *Int J Refract Met Hard Mater* **19** (2001), pp. 341-8

[100] Llanes L, Torres Y, Anglada M: On the fatigue crack growth behaviour of WC-Co cemented carbides: kinetics description, microstructural effects and fatigue sensitivity. *Acta Mater* **50** (2002), pp. 2381-93

[101] Sigl LS, Exner HE: Experimental study of the mechanics of fracture in WC-Co alloys. *Metall Trans A* **18A** (1987), pp. 1299-308

[102] Schleinkofer U, Sockel HG, Görting K, Heinrich W: Fatigue of hard metals and cermets. *Mater Sci Eng* **A209** (1996), pp. 313-7

[103] Kursawe S, Pott P, Sockel HG, Heinrich W, Wolf M: On the influence of binder content and binder composition on the mechanical properties of hardmetals. *Int J Refract Met Hard Mater* **19** (2001), pp. 335-40

[104] Sailer T, Herr M, Sockel HG, Schulte R, Feld H, Prakash LJ: Microstructure and mechanical properties of ultrafine-grained hardmetals. *Int J Refract Met Hard Mater* **19** (2001), pp. 553-9

[105] Dary FC, Roebuck B, Gee MG: Effects of microstructure on the thermo-mechanical fatigue responce of hardmetals using a new miniaturized testing rig. *Int J Refract Met Hard Mater* **17** (1999), pp.45-53

[106] Roebuck B, Maderud CJ, Morrel R: Elevated temperature fatigue testing of hardmetals using notched testpieces. *Int J Refract Met Hard Mater* **26** (2008), pp. 19-27

[107] Kindermann P, Schlund P, Sockel HG, Herr M, Heinrich W, Görting K, Schleinkofer U: High-temperature fatigue of cemented carbides under cyclic loads. *Int J Refract Met Hard Mater* **17** (1999), pp. 55-68

[108] Bauschinger J: Über die Veränderung der Elastizitätsgrenze und der Festigkeit des Eisens und Stahls durch Strecken, Quetschen, Erwärmen, Abkühlen und durch oftmals wiederholte Belastung. (1886) Mitt: Mech-Tech Lab, XIII München

[109] Llorca J, Needleman A, Suresh S: The Bauschinger effect in whisker-reinforced metal-matrix composites. *Scr Metall Mater* **24** (1990), pp. 1203-8

[110] Bruzzi MS, McHugh PE, O'Rourke F, Linder T: 2001. Micromechanical modelling of the static and cyclic loading of an Al2124-SiC MMC. *Int J Plasticity* **17** (2001), pp. 565-99

[111] Xiang Y, Vlassak JJ: Bauschinger effect in thin metal films. *Scr Mater* **53** (2005), pp. 177-82

[112] Rajagopalan J, Han JH, Saif MTA: Bauschinger effect in unpassivated freestanding nanoscale metal films. *Scr Mater* **59** (2008), pp. 734-7

[113] Kang G: Ratchetting: Recent progresses in phenomenon observation, constituitive modelling and application. *Int J Fatigue* **30** (2008), pp. 1448-72

[114] Krawitz AD, Venter AM, Drake EF, Luyckx SB, Clausen B: Phase response of WC-Ni to cyclic compressive loading and its relation to toughness. *Int J Refract Met Hard Mater* **27** (2009), pp. 313–6

[115] Kang G: Uniaxial time-dependent ratchetting of SiCP/6061Al alloy composites at room and high temperature. *Comp Sci Tech* **66** (2006), pp. 1418-30

[116] Fleck NA, Shin CS, Smith RA: Fatigue crack growth under compressive loading. *Eng Fract Mech* **21** (1985), pp. 173-85

[117] Wöhler A: Versuche über die Festigkeit der Eisenbahnwagenachsen. *Zeitschrift für Bauwesen* **10** (1860), English summary: *Engineering* **4** (1867), pp 160-1

[118] Murakami Y: *Metal fatigue: Effects of defects and nonmetallic inclusions*. Elsevier, Oxford (2002), pp. 11-24

[119] Erling G, Kursawe S, Luyckx S, Sockel HG: Stable and unstable fracture surface features in WC-Co. *J Mater Sci Lett* **19** (2000), pp. 437-8

[120] Jesner G, Pippan R: Failure mechanisms in a fatiugue-loaded high performance powder metallurgical tool steel. *Metall Mater Trans A* **40A** (2009), pp. 810-7

[121] Pepelin VM: Resistivity of hard alloys to finite plastic deformation. *Sov Powder Met Metal Ceram* (1966), pp. 253-8

[122] Pepelin VM: Effect of plastic deformation on the pysicomechanical properties of tungsten carbide-cobalt hard alloys. *Sov Powder Met Metal Ceram* (1965), pp. 933-8

[123] Abbas NM, Solomon DG, Bahari MF: A review on current research trends in electrical discharge machining (EDM). *Int J Mach Tools Manuf* **47** (2007), pp. 1214-28

[124] Gadalla AM, Tsai W: Electrical discharge machining of tungsten carbide-cobalt composites. *J Am Ceram Soc* **72** (1989) [8], pp. 1396-1401

[125] Jahan MP, Wong YS, Rahman M: A study on the fine-finish die-sinking micro-EDM of tungsten carbide using different electrode materials. *J Mater Process Technol* **209** (2009), pp. 3956-67

[126] Casas B, Torres Y, Llanes L: Fracture and fatigue behavior of electrical-discharge machined cemented carbides. *Int J Refract Met Hard Mater* **24** (2006), pp. 162–7

[127] Hück M: An improved method for the evaluation of staircase tests. *Z Werkstofftech* **14** (1983), pp. 406-17

[128] Noyan IC, Cohen JB: Residual stress measurement by diffraction and interpretation. Springer, Berlin (1987), pp. 117-63

[129] Bonny K, De Baets P, Quintelier J, Vleugels J, Jiang D, Van der Biest O, Lauwers B, Liu W: Surface finishing: Impact on tribological characteristics of WC–Co hardmetals. *Tribol Int* **43** (2010), pp. 40-54

[130] Larsson C, Odén M: X-ray diffraction determination of residual stresses in functionally graded WC–Co composites. *Int J Refract Met Hard Mater* **22** (2004), pp. 177-84

[131] Livescu V, Clausen B, Paggett JW, Krawitz AD, Drake EF, Bourke MAM: Measurement and modeling of room temperature co-deformation in WC–10 wt.% Co. *Mater Sci Eng* **A399** (2005), pp. 134-40

[132] Mari D, Krawitz AD, Richardson JW, Benoit W: Residual stress in WC-Co measured by neutron diffraction. *Mater Sci Eng* **A209** (1996), pp. 197-205

[133] Mari D, Clausen B, Bourke MAM, Buss K: Measurement of residual thermal stress in WC-Co by neutron diffraction. *Int J Refract Met Hard Mater* **27** (2009), pp. 282-7

[134] Wehner T, Fatemi A: Effects of mean stress on fatigue behaviour of a hardened carbon steel. *Int J Fatigue* **13** (1991) [13], pp. 141-8

[135] http://www.mathworks.com/help/toolbox/images/

10 Appendix

Skeletonization procedure for Matlab version R2009a used to determine Co binder matricity values [135]:

```
I = imread('imagetitle of binary image.tif');
% Pad the array for later use
I = padarray(I,[2 2],false,'both');
% Perform skeletonization or also called thinning
thin_co = bwmorph(I, 'thin',inf);
% Display the skeletonized image
imtool(thin_co);
% Calculate pixel line length considering orientations of neighbouring pixels
% Get orientation at each point
my_orientations = zeros(size(I));
% Preallocate; [row col] indices of points on skel
[r c] = find(thin_co);
% Note: This is why we padded earlier: all r,c are greater>=3 and <= size(dim) -2
% Go to each point and calculate orientation
for ii = 1:length(r)
   % Extract all pixels within the 5x5 window surrounding our point
   SKpart = thin_co((r(ii)-2):(r(ii)+2),(c(ii)-2):(c(ii)+2));
   % Connected components analysis, 8 connectivity (we care about corners!)
   CC =bwconncomp(SKpart,8);
   % Get orientation
   RP = regionprops(CC,'Orientation');
   % Save the orientation
   my_orientations(r(ii),c(ii)) = RP.Orientation;
end
% Sign doesn't matter
length_orientations = abs(my_orientations);
% Get angle closest to any axis
length_orientations(length_orientations>45)=90-
length_orientations(length_orientations>45);
% Get length, preserving only those in the skeleton, ".*" - elementwise multiplication
eachLength = 1./cosd(length_orientations).*double(thin_co);
skeletonlength_phase1 = sum(eachLength(:));
```